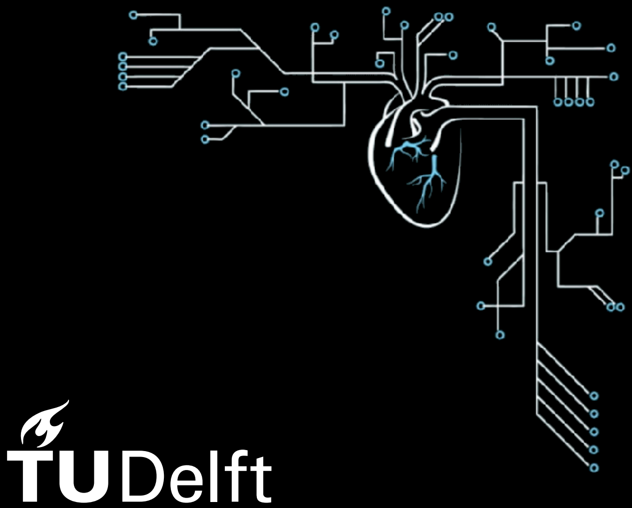

Design, Integration and Characterization of Microelectrodes for Heart-On-Chip Application

Shriya Rangaswamy

Design, Integration and Characterization of Microelectrodes for Heart-On-Chip Application

by

Shriya Rangaswamy

in partial fulfillment of the requirements for the degree of

Master of Science

in Biomedical Engineering

at the

Faculty of Mechanical, Maritime and Materials Engineering

Delft University of Technology

to be defended on March 31, 2021 at 15:00

Student number :	4899970	
Project duration :	August 2019 - March 2021	
Supervisor :	Prof. dr. ir. R Dekker	TU Delft, Phillips
Daily supervisor :	Dr. ir. N. Gaio	BIOND Solutions
Thesis committee :	Prof. dr. ir. R Dekker	TU Delft, Phillips
	Prof. dr. P.M. Sarro	TU Delft
	Prof. dr. ir. P.J. French	TU Delft
	Dr. ir. N. Gaio	BI/OND Solutions

Abstract

The lack of reliable disease models hampers the development of safe and effective drugs for humans as they fail to precisely identify the cardiotoxicity profile of drug compounds. Recent technological advancements have led to the development of the *"Organ-On-Chip"* (OOC) technology. OOCs are miniaturized micro-engineered devices which aim to accurately recapitulate the physiological conditions of different organs. In order to develop a Heart-On-Chip (HOC) device as an *in-vitro* screening platform for cardiotoxicity, it is essential to integrate micro-electrodes (MEAs) in a flexible polymeric substrate that can be manufactured with standard micro-fabrication techniques. Besides electrical stimulation and recording, the device should be capable of accommodating the different cellular structures of the human heart along with its vasculature, which is in continual exposure to perfusion with fluid. In this manner, a platform that is cleanroom-compatible, scalable and physiologically representative of the human heart can be developed.

The OOC device of Bi/ond provides an ideal platform in which MEAs can be successfully integrated. The device also offers microfluidic channels that supply the cardiac co-culture with the necessary perfusion to mimic the blood flow through the heart. In order to integrate TiN MEAs in the Bi/ond platform, several technological challenges need to be tackled. In previous work, polymers were often utilized as the insulation layer for the metal interconnects. Processing of polymers in a silicon-based cleanroom environment requires additional dedicated equipment. Therefore, it is necessary to investigate the feasibility of alternative dielectric, cleanroom-compatible materials, such as silicon nitride. Secondly, the metal lines experience considerable amounts of stress at the interface of the flexible membrane and the rigid silicon frame during the fabrication and post-fabrication process. By customizing the mechanical design of the PDMS membrane as well as the metal interconnects, the stress developed at the interface can be reduced, which can ultimately improve the yield of the devices due to the formation of fewer cracks in the metal lines.

In this thesis, three goals were defined and achieved in order to develop a proof-of-concept for a HOC device with silicon nitride encapsulated TiN MEA in a thick PDMS layer, which can be further integrated in a microfluidic device. First, a study of the compatibility and characterization of SiN_x insulation layers with PDMS membranes was performed. The adhesion between the nitride and PDMS membrane was improved by sandwiching a thin silicon oxide layer in-between the nitride and the PDMS. Additionally, we demonstrated the optimum deposition techniques for the nitride layers. Secondly, the yield of the devices was improved by optimizing the designs of the interconnects and the shape of the PDMS membranes. A novel *turtle* shaped design for the membrane was developed which helped to redistribute the stress at the interface. This novel design resulted in a yield higher than 75%.

Thirdly, a silicon-based cleanroom compatible fabrication protocol was optimized and defined for processing a HOC device with a TiN MEA encapsulated by SiN_x in a 200 μm thick PDMS membrane. Moreover, based on the techniques developed by Bi/ond, this device module was successfully integrated in a microfluidic device. Finally, Electrochemical Impedance Spectroscopy (EIS) measurements were carried out to confirm the functionality of the electrodes. The average impedance value at 1 kHz of three working electrodes was measured to be in the order of 800 kΩ, proving that an electrical connection was successfully established between the embedded TiN electrodes and the bondpads on the silicon frame.

Acknowledgements

"Anything that can go wrong will go wrong". Murphy's Law doesn't begin to cover the experience of working inside a cleanroom. The past eight months have definitely been a challenging, yet rewarding experience. I would like to thank Ronald for introducing me to the wonderful field of Organ-On-Chip technology. His invaluable input and his ability to break down complex concepts such that even a novice, like me, could understand will always be appreciated. I will always admire his passion for innovation and his ability to see the silver lining in every situation.

I would like to thank BI/OND Solutions for giving me the opportunity to work with them on such an interesting project. It wouldn't have been possible for me to have seen this project through without the constant guidance and support from Niko. It has always been easy for me to have an open conversations with him about work, life and everything else in between. I have learnt a lot from watching him work. He has truly been an inspiration. He has also helped me understand the tips and tricks of troubleshooting issues and ensuring that all possibilities have been explored. Unfortunately, he has also had to bear my, rather dramatic, downfalls. I will always appreciate his support during these times.

I would also like to thank the other members of the Bi/ond team: Cinzia, for all the witty conversations during lunch; William, for helping me with the simulations for this project; Anish, for helping me develop the designs for this project; Amr, Lonneke and Luis for their kind support.

I would like to thank all the staff and users of the EKL facility at TU Delft: Silvana, Tom, Mario, Aleksandar, Hitham and Johannes for their patience and time taken to train me on multiple equipment; Juan and Milica, for patiently answering all my doubts inside the cleanroom; Paolo, for always providing a helping hand and for all the interesting conversations during the long hours inside the lab (ranging from food, travel, life and of course, work); Marta, Hande, Paul, Roberto for their help inside the lab.

I was really lucky to have a great support system at the University. I loved all the coffee and tea breaks with Danai, Merlin, Siri and Luutzen. I would like to thank them for all their moral support.

I want to extend my gratitude to Maneesh for his unwavering emotional support and for going the extra mile to make sure I'm well-fed, especially during the last stages of my thesis. He has constantly stuck by my side even at my worst moments, and for that, I'll forever be grateful. I want to thank Vijay, Kruthika and their lovely daughter- Pragna, for always checking up on me and making sure I'm taking care of myself. They are truly my family away from home. I would also like to thank all my friends, who have offered their support virtually: Vandana, Pavithra, Advesh, Manju, Prithvi, Sharadhi and Manasa. This challenging journey would have been more difficult to handle if it weren't for the good company of my housemates. I always had someone to talk to at home at the end of a long day.

None of this would be possible if it weren't for my family. Knowing that I have people on whom I can fall back, without any second thought, has always comforted me when things felt overwhelming during these trying times. My parents have always encouraged me to pursue my interests and pushed me to be the best version of myself. I would also like to thank my brother for always believing in me and for being my personal cheerleader. I am grateful for everyone in my family: my Ajji (grandmother), my aunts and my cousins for reminding me of all the things I should be proud of.

Shriya Rangaswamy
31st March, 2021

Contents

1 Introduction **1**
1.1 Drug Discovery and Development . . . 1
1.2 Cardiotoxicity . . . 2
1.3 Heart-On-Chip . . . 2
1.4 Bi/ond Platform . . . 3
1.5 Research Goals and Approach . . . 4
1.5.1 Thesis outline . . . 5

2 Literature Review **6**
2.1 Cardiotoxicity . . . 6
2.1.1 Measurement of the Electrical Activity of Cardiomyocytes - Microelectrode Arrays (MEAs) . . . 7
2.1.1.1 Electrode-Electrolyte Interface . . . 8
2.1.1.2 Materials and Electrochemical Properties of MEAs . . . 9
2.2 Organ-On-Chip (OOC) Models . . . 9
2.2.1 Heart-On-Chip (HOC) . . . 9
2.3 Design Challenges Of MEAs for OOC Application . . . 11
2.3.1 Mechanical Design of Electrodes and Interconnects . . . 11
2.3.2 Insulation Materials . . . 15
2.3.2.1 Polyimide Insulation . . . 15
2.3.2.2 Silicon Nitride Insulation . . . 16

3 Mechanical Design of the MEA **18**
3.1 The Oval Design . . . 18
3.2 The Turtle Design . . . 23
3.3 Summary of the Designs . . . 29

4 Fabrication Challenges Associated with Silicon Nitride Interconnects **33**
4.1 Adhesion Between Silicon Nitride and PDMS . . . 33
4.2 Stress Analysis . . . 39
4.2.1 Effect of the Novel Membrane Designs . . . 40
4.2.2 Effect of the Deposition Technique of Silicon Nitride . . . 41

5 Fabrication and Characterization of the Device **44**
5.1 Fabrication of the Final Device . . . 44
5.2 Study of Formation of Cracks . . . 52
5.3 Electrochemical Impedance Spectroscopy (EIS) . . . 55

6 Conclusion **58**
6.1 Recommendations and Future Work . . . 59

A Appendices **60**
A.1 Organ-On-Chip (OOC) Models . . . 60
A.2 Wet Etching of Silicon Nitride . . . 63
A.3 Sheet Resistance of Titanium Nitride . . . 64

List of abbreviations

AC	: Alternating Current
BBB	: Blood-brain Barrier
BHF	: Buffered hydrofluoric acid
CE	: Counter electrode
CM	: Cardiomyocyte
CDC	: Charge Delivery Capacity
CVD	: Cardiovascular Diseases
DILI	: Drug-induced Liver Injury
DI	: Deionized water
DSP	: Double Side Polished
DRIE	: Deep Reactive Ion Etching
EKL	: Else Kooi Laboratory
EIS	: Electrochemical Impedance Spectroscopy
ECM	: Extracellular Matrix
FEM	: Finite Element Model
HF	: Hydrofluoric acid
HOC	: Heart-On-Chip
iPSC	: Induced Pluripotent Stem Cells
LPCVD	: Low Pressure Chemical Vapor Deposition
MEA	: Micro-electrode Array
MEMS	: MicroElectroMechanical Systems
MCS	: Multi Channel Systems
MTF	: Muscular Thin Films
OOC	: Organ-On-Chip
PDMS	: Polydimethylsiloxane
PEDOT	: Poly (3,4 – Ethylenedioxythiophene
PLC	: Primary Liver Cells
PECVD	: Plasma Enhanced Chemical Vapor Deposition
PI	: Polyimide
R&D	: Research and Development
RE	: Reference electrode
RT	: Room Temperature
SiN_x	: Silicon Nitride
SEM	: Scanning Electron Microscope
SSP	: Single Side Polished
TEER	: Transendothelial Electrical Resistance
TEOS	: Tetraethyl orthosilicate

TiN : Titanium Nitride

USB : Ultrasonic bath

WE : Working electrode

List of symbols

E : Young's modulus, MPa

t : Thickness, m

r : bending radius, m^2/s

σ : Bending stress, MPa

R_s : Sheet resistance, $\Omega/\square$

ρ : Resistivity, Ω.m

List of Figures

1.1 Drug development pipeline [2]. 1
1.2 Scanning Electron Microscope (SEM) images of the Cytostretch platform: (a) dog bone shaped polymeric membrane, as seen from the back of the device after silicon etching; (b) enlarged image of the metal electrodes encapsulated by parylene insulation and the micro-grooves patterned on the stretchable membrane [23]. 3
1.3 Bi/ond device: (a) 3-Dimensional schematic overview of the chip, illustrating the open well integrated with six electrodes and connected to the inlet and outlet of the micro-fluidic channel (b) Photograph of the *inCHIPit*^{TM} platform with a single channel *(left)* and with three channels (*right*) [24]. 4

2.1 (a) Elongation of the duration of the action potential of ventricles during cardiotoxicity, (b) resulting in the elongation of the QT interval of an electrocardiogram (ECG). Adapted from [35]. 7
2.2 (a) A commercialized micro-electrode array (MEA) fabricated using lithography techniques supported by a glass-ring which maintains the cell culture; (b) An overview of the MEA [43]. 8
2.3 A schematic representation of a Heart-on-Chip platform comprising of a Muscular Thin Film (MTF) chip attached to a polymeric micro-fluidic device, which accounts for the dynamic representation of the human heart [18] 10
2.4 (a) Meander design for interconnects specified by three important parameters: the diameter (D), the angle (H) and the width (W); (b) Meanders assuming an angle of 45° are termed as horseshoe shaped meanders [74]. 12
2.5 The average values of strain sustained by the horseshoe interconnects before their failure for different values of radius (R), width (W) and angle [72]. 12
2.6 The dogbone shape of the Cytostretch membrane comprised of four concave corners. The red lines represent the route assumed by the interconnects [23]. 13
2.7 Principal strain directions sustained in one corner of the Cytostretch membrane. (a) Directions of the first principal strain, as indicated by the red arrows. The dotted black lines represent the possible multiple tracks for the interconnects; (b) Directions of the second principal strain. The white lines indicate the path for the interconnects where they experience zero strain [23]. 13
2.8 (a) The effect of the interconnect track on the magnitude of the second principal strain in the Cytostretch flexible membrane; (b) The stress developed in the interconnect with a width of 20 μm and a thickness of 4 μm [23]. 14
2.9 Cracks observed in the metal (Titanium nitride, TiN) lines after the dicing process as shown by the yellow arrow [24]. 14
2.10 SEM image of a MEMS device with polyimide insulating layers post Deep Reactive Ion Etching (DRIE) process. Granular residues remain on the surface of the device after plasma treatment [85]. 15
2.11 (a) Residues observed on the silicon oxide layer after etching of polyimide using an aluminium (Al) hard mask; (b) "Fur-like" residues seen on the device with free-standing interconnects after etching of polyimide [73]. 16
2.12 Sputtering temperature dependence of the resistivity of platinum (Pt). Adapted from [90]. 17

3.1 3D rendering of the Bi/ond *oval* platform in which the MEA is integrated. The figure is not drawn to scale. 19

3.2 Magnitude and direction of the first principal strain developed in the *oval* membrane when it is subjected to an external pressure. The rectangular box marked by the black dashed lines depict the area where the magnitude of the first principal strain at the interface is relatively low. 19
3.3 Magnitude and direction of the second principal strain of the *oval* PDMS membrane when subjected to an external pressure. The smaller concentric ellipse enclosed within the black dashed lines represent the regions of zero-second principal strain. 20
3.4 The direction of the first principal strain, indicated by the red arrows, acting on one half of the *oval* membrane when subjected to an external pressure. The black lines depict the trajectories assumed for the interconnects when traversing from the membrane to the silicon substrate. 20
3.5 The different ranges of the magnitude of the principal strains acting on one-quarter of the *oval* membrane when subjected to an pressure. A region of minimum strain is defined (indicated by the black dashed lines), which approximately spans a distance of 0.4 mm from the outer periphery of the *oval* membrane. 21
3.6 The schematic representation of the oval design. The interconnect tracks are represented by the red lines. (a) The arrangement of six straight interconnect lines; (b) The arrangement of six interconnects which are designed in the form of meanders. The figures are not drawn to scale. 22
3.7 Different designs of the *straight* metal lines and the interconnects in one half of the oval membrane: (a) Shorter metal lines with a width of 10 μm; (b) Shorter metal lines with a width of 30 μm; (c) Longer metal lines with a width of 10 μm; (d) Longer metal lines with a width of 30 μm. 22
3.8 Different designs of the horseshoe-shaped *meanders* as the metal lines and the interconnects in one half of the oval membrane: (a) Shorter meanders with a width of 10 μm; (b) Shorter meanders with a width of 30 μm; (c) Longer meanders with a width of 10 μm; (d) Longer meanders with a width of 30 μm. 23
3.9 Mask designs of the *turtle* membrane. (a) The geometry of the *turtle* membrane accommodating the meandering interconnects; (b) The design of the *turtle* membrane for the straight interconnects. The figures are not drawn to scale. 24
3.10 The magnitude and direction (indicated by the red arrows) of the first principal strains acting on the *turtle* PDMS membrane when subjected to an external pressure: (a-b) Results of the FEM analysis for the membrane defined for the *meander* interconnects; (c-d) Direction of the first principal strain (indicated by red arrows), for the membrane to accommodate *straight* interconnects, along with its 3D representation. 25
3.11 The magnitude and direction of the first and second principal strains acting on the *turtle* PDMS membrane when subjected to an external pressure. (a-b) Second principal strain profile and its 3D illustration of the membrane designed for the *meanders*; (c-d) Second principal strain profile and its 3D illustration of the membrane designed for the *straight* lines. 26
3.12 The magnitude of the first principal strain acting on one half of the *turtle* membrane when subjected to an external pressure. (a) The region marked by the red lines depict the area of interest, where the maximum strain obtained is $\sim$5%; (b) The black lines depict the trajectories of the interconnects when traversing from the PDMS membrane to the silicon substrate. 26
3.13 The influence of the interconnect paths on the stress distribution of the *turtle* membrane. (a) The distribution of the first principal strain when *straight* interconnects were integrated on the membrane; (b) 3D representation of the influence of the *straight* interconnect lines. 27
3.14 The schematic representation of the *turtle* design. The interconnect tracks are represented by the red lines. (a) The arrangement of six straight interconnect lines; (b) The arrangement of six interconnects which are designed to assume the shape of horseshoe meanders. The figures are not drawn to scale. 27
3.15 Different designs of the *straight* and *meander* interconnects in one half of the *turtle* membrane: (a) Shorter *straight* metal lines with a width of 10 μm; (b) Shorter *straight* metal lines with a width of 30 μm; (c) Longer *straight* metal lines with a width of 10 μm; (d) Longer *straight* metal lines with a width of 30 μm; (e) Shorter *meanders* with a width of 10 μm; (f) Shorter *meanders* with a width of 30 μm; (g) Longer *meanders* with a width of 10 μm; (h) Longer *meanders* with a width of 30 μm. 28

3.16 Mask designs of the membrane geometry adopted for the current Heart-On-Chip device. (a) The geometry of the *oval* membrane; (b) The geometry of the *turtle* membrane accommodating the meandering interconnects; (c) The design of the *turtle* membrane intended for the straight interconnects. The figures are not drawn to scale. 29
3.17 Summary of the different parameters based on which multiple designs for the metal interconnects were devised. 30

4.1 A 2D cross-sectional overview of the process flow to fabricate the current device. In this device, TiN electrodes that are insulated by silicon nitride structures are embedded in a thick PDMS membrane. The figure is not drawn to scale. 33
4.2 Fabrication flow of the test device for the adhesion test. (a) Deposition of the PECVD TEOS landing layer on the front and processing of the backside PECVD SiO_2; (b) Patterning of LPCVD silicon nitride insulating layer; (c) Deposition and patterning of the second insulating PECVD SiN_x layer. The figures are not drawn to scale. 34
4.3 (a) *oxide-AFTER* device, with a thin PECVD SiO_2 layer deposited on top of the patterned nitride stack; (b) *oxide-BEFORE* sample, where the thin oxide layer is patterned lithographically along with the stack of nitride layers. The figures are not drawn to scale. . . 34
4.4 Process flow of the *control* set: (a) Curing of PDMS; (b) Membrane releasing; (c) Top view of the *control* samples, after releasing of the membrane. Process flow of the *oxide-AFTER* devices: (d) PDMS coating; (e) Membrane releasing; (f) Top view, illustrating the deposition of the oxide layer over the entire surface of the sample. Process flow of the *oxide-BEFORE* samples: (g) Coating with PDMS; (h) Membrane releasing; (i) Top view of the *oxide-BEFORE* samples, which shows the processing of the oxide layer along with the nitride stack; (j) Bottom view of the devices after releasing the membrane. The figures are not drawn to scale. 35
4.5 (a) Delamination of the silicon nitride layer from the PDMS membrane when immersed in an USB with acetone at 40°C, as seen in the *control* set; (d), (e) and (f) Delamination of the nitride layers, as observed in the *oxide-AFTER* devices; (g), (h) and (i) The effect of the additional oxide layer in the *oxide-BEFORE* samples which do not exhibit any delamination of the SiN_x layer after being exposed to the same solvent for a period of 20 minutes. . . . 37
4.6 a 2D sketch of the (a) *oxide-AFTER* and, (b) the *oxide-BEFORE* samples. 38
4.7 The occurrence of wrinkles on the PDMS membrane as observed under a microscope during the adhesion test, for different designs: (a) EC10; (b) ME30; (c) EC10_Extend; (d) MC10_Extend. 39
4.8 Process flow for the fabrication of test devices to investigate the effect of the membrane design on the stress profile of the PDMS membrane: (a) Processing of the backside and front side PECVD SiO_2; (b) PDMS coating; (c) Through-silicon etching and membrane releasing; (d) Bottom view of the final test sample. The figures are not drawn to scale. . . 40
4.9 Microscope images of the PDMS membrane as observed in the samples fabricated for evaluating the effect of the membrane design on the formation of *wrinkles* in different designs, such as the: (a) Oval membrane; (b) Turtle membrane, for the straight metal lines; (c) Turtle membrane, to accommodate the meanders. 41
4.10 Fabrication flow for the samples utilized to analyze the effect of PECVD SiN_x structures on the formation of *wrinkles* when the PDMS membrane is released via DRIE process: (a) Processing of PECVD SiO_2 on the backside and front side of a DSP wafer; (b) Patterning of a stack of PECVD SiN_x and an oxide adhesion layer; (c) PDMS coating; (d) Membrane releasing; (e) Bottom view of the final sample, which displays the PECVD SiN_x insulation structures embedded in the PDMS membrane. The figures are not drawn to scale. 42
4.11 Microscope images of the test samples with PECVD SiN_x structures embedded in the PDMS membrane on a DSP wafer after releasing the membrane, as observed for different designs such as: (a) EE30; (b) EC10; (c) EE10_Extend; (d) MC30. 43

5.1 Process flow for the fabrication of the final device: (a) Deposition of the PECVD SiO_2 landing layer on the front and the patterning of the PECVD SiO_2 on the back; (b) Patterning of the electrode openings and the first isolation layer defined by PECVD SiN_x; (c) Patterning of TiN to form the electrodes and the bond pads, and its (d) Top view; (e) Deposition, patterning and dry etching of the second PECVD SiN_x isolation layer along with the thin oxide adhesion layer; (f) PDMS coating; (g) Membrane releasing, and its (h) Top view; (i) Opening of the bond pads, and its (j) Top view; (k) Bottom view of the device depicting the electrode openings embedded in the PDMS membrane. The figures are not drawn to scale. 45
5.2 Mask designs adopted for the current Heart-On-Chip device illustrated for one half of the membrane. (a) Design of the first layer of silicon nitride *straight* lines insulating the metal lines, with an opening of 30 μm for the TiN electrodes; (b) Design of the horseshoe-shaped *meanders* of the first layer of silicon nitride with the 30 μm electrode openings; (c) Design of the *straight* metal lines and electrodes; (d) Design of the horseshoe-shaped *meanders* for the metal lines; (e) Design of the second insulating layer of silicon nitride (*straight* lines); (f) The second layer of silicon nitride (*meanders*). The figures are not drawn to scale. . . . 46
5.3 SEM images of the first layer of PECVD SiN_x isolation structures (*straight* lines and the *meanders*), with the 30 μm electrode openings. 47
5.4 SEM images of the TiN metal lines (*straight* lines and *meanders*) on the first SiN_x isolation layer, and the TiN bondpads. 47
5.5 SEM images showing the insulated TiN metal lines (*straight* lines and *meanders*) by the second layer of PECVD SiN_x, leaving the TiN bondpads exposed. 48
5.6 SEM images of the 30 μm TiN electrodes embedded in a thick PDMS *oval* membrane. The TiN metal lines are insulated by short *meander* structures of PECVD SiN_x. 49
5.7 SEM images of the 30 μm TiN electrodes integrated in a thick PDMS *turtle* membrane. The TiN metal lines are insulated by long *meander* structures of PECVD SiN_x. 50
5.8 SEM images of the 30 μm TiN electrodes embedded in a thick PDMS *oval* membrane. The TiN metal lines are insulated by long *straight* lines of PECVD SiN_x. 50
5.9 Images of the final device taken under an optical microscope, where the TiN electrodes and metal lines are integrated in a thick layer of PDMS, as seen in different designs: (i) EC10 (ii) EC10_Extend (iii) EC30_Extend (iv) EE30_Extend. 51
5.10 Images of the device with the EC10_Extend design, taken under a microscope, which: (a) displays the micro-fluidic channel integrated by Bi/ond, and (b) its magnified image. . . . 51
5.11 Different designs of the device as observed under a microscope *before* the dicing process. No cracks were observed in many of the designs, including: (a) EE30 (b) EE30_Extend, and (c) ME30_Extend designs. However, cracks in the TiN metal lines even *before* dicing were observed in some of the device designs, such as: (d) ME30. 52
5.12 Formation of cracks (post dicing) in the horseshoe-shaped TiN *meanders* in the: (a) *oval* membrane, and (b) *turtle* membrane; (c, d) No cracks observed for the *straight* lines in the *turtle* membrane, *after* the dicing process. 53
5.13 Set-up of a three-electrode system for performing EIS measurements for the current device (EC30_Extend). 56
5.14 The bode plots from the EIS measurements, conduced over a frequency range of 1-100 kHz, of the TiN MEAs. 57

A.1 Illustration of the Lungs-on-Chip platform which comprises of two chambers connected by a porous, thin and flexible polymer membrane; *(right)* Vacuum applied to the two compartments enables the polymer membrane to be stretched which emulates the breathing action in the lungs [105]. 60
A.2 Multiple layers of primary liver cells (PLCs) cultured on a PDMS substrate to provide (a) a biological guide for the growth of cells; (b) a hexagonal contour; (c) inclusion of a reservoir in the platform to enable circulation; (d) inclusion of a diverter for the purpose of vertical circulation [107] 61
A.3 Schematic illustration of the blood-brain barrier chip: (a) top and bottom faces of the chip; (b) integration of platinum electrodes in the chip; (c) assembled PDMS platform of the chip [108] 62
A.4 Illustration of the Nephron-on-Chip device designed by Weinberg et al. [110]. 62
A.5 (a) Etching of LPCVD Si_3N_4 in 5% HF; (b) Etching of PECVD SiN_x in 5% HF; (c) Etching of LPCVD Si_3N_4 in 1:7 BHF; (d) Etching of PECVD SiN_x in 1:7 BHF. 63

List of Tables

3.1 Overview of the design nomenclature and their descriptions. 31

3.2 Matrix depicting the different design parameters considered for the *oval* and the *turtle* membrane and their respective nomenclatures. 32

4.1 Results of the adhesion test of the test samples in different solvents. 38

5.1 Percentage yield of metal lines during fabrication and post fabrication process. 54

A.1 Resistivity values of TiN sputtered at different temperatures. 64

1 | Introduction

1.1 Drug Discovery and Development

Before a new drug is introduced into the market, it must go through an extremely lengthy and extensive process of testing and approval. Figure 1.1 depicts the overview of the drug development process, which can be broadly categorized into five stages, namely target discovery, pre-clinical trials, clinical trials, review by regulatory authorities and post-market surveillance. Once a novel drug target has been identified, its therapeutic effects are validated via high-throughput screening which mainly consists of *in-vitro* assays. Selected compounds from these assays are then further evaluated for their toxicological and pharmacological characteristics mainly in animal models. Most compounds fail at these early phases of validation and testing, owing to the fact that *in-vivo* animal testing primarily aims to verify the toxicity of the drug compounds rather than their therapeutic effects. The pre-clinical phase realizes the potential side effects, mode of action of the drug compounds and scale-up information for their respective manufacturing [1]. The regulatory board approves clinical trials if the results obtained from previous testing is deemed safe and effective for human applications. The clinical trials consist of three phases, wherein Phase I focuses on the safety profile of drugs, Phase II on the effectiveness and Phase II is dedicated for corroborating the findings on a broader range of the population. Finally, after approval from appropriate regulatory boards, a drug candidate enters the market for commercial applications whilst being under constant scrutiny by the regulatory authorities.

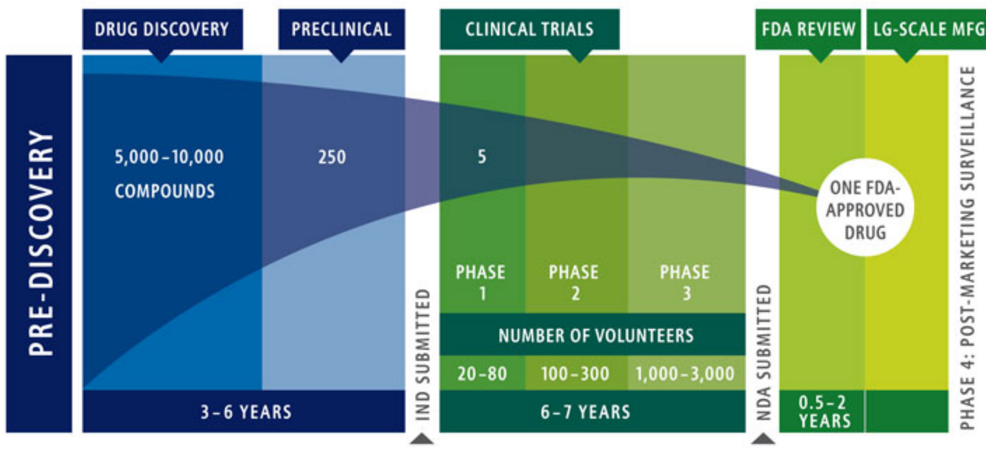

Figure 1.1: Drug development pipeline [2].

On an average, pharmaceutical companies invest $1.2 billion over a span of 10-15 years for the research and development of a new drug [3]. The nearly exponential increase in the investments made in the Research and Development (R&D) sector of the industry has not resulted in a boom in the number of drugs that is capable of being marketed. This "productivity paradox" is a major hurdle that the pharmaceutical industry is yet to surpass [4]. Moreover, a large number of marketed drugs are withdrawn due to unexpected side-effects, resulting in huge financial ramifications for pharmaceutical companies. Currently, the gold standards for testing drug compounds are utilizing *in-vitro* cell cultures and relying on animal models. Although these techniques have provided useful insights for decades, they fail to sufficiently emulate the natural microenvironment of organs inside the human body. Moreover, there are

ethical concerns that need to be considered when working with animal models for human applications. Therefore, it is imperative to build disease models that can accurately predict the safety of drugs in humans while simultaneously minimizing the need for animal models in drug testing [5, 6].

1.2 Cardiotoxicity

The lack of reliable disease models hampers the development of drugs that are safe and effective in humans as they fail to precisely identify the toxicology profile of drugs [7, 8]. Currently, 2-Dimensional (2D) *in-vitro* assays and animal models are employed for the toxicology and efficacy evaluation of drug molecules. 2D cell cultures on petri dishes fail to provide cells with the ability to interact with the surrounding tissues as is the case in a normal human body. The absence of accurate cell-cell and cell-tissue interaction in 2D cultures makes it difficult to mimic the mechanism of drug interactions within the human body. Several drugs developed to treat severe diseases, such as cardiovascular ailments, often fail in the later stages of development as a result of cardiotoxicity [9].

Cardiotoxicity adversely affects the action potential of cardiomyocytes which can ultimately result in fatal cardiac arrests. In the period between 1990-2001, several marketed drugs were recalled on account of the onset of cardiotoxicity in humans [10, 11]. The detection of cardiotoxicity at the earlier stages of the drug development pipeline is necessary to accurately predict the safety profile of drugs. This calls for a transition to be made from 2D assays to 3-Dimensional (3D) cell cultures. Additionally, the ethical concerns regarding the use of animals for testing drugs are extensive. Therefore, it is also crucial to develop a method or technology that pushes both the scientific community and the industry towards a future where the use of animal models becomes redundant.

Advances in tissue engineering research have made it feasible to develop biologically appropriate human cardiac models, which can be employed for the early detection of cardiotoxicity. These models utilize human induced pluripotent stem cell (iPSC) derived cardiomyocytes, as they have a higher predictive value [12]. Additionally, developments achieved in microfluidics have made it possible to recapture the dynamics of the human heart [12]. Recent technological advancements have provided momentum for the development of the relatively novel *"Organ-On-Chip (OOC)"* technology. OOCs are miniaturized micro-engineered devices on which different human cell-types can be incorporated to accurately mimic the physiological conditions of different organs [13, 14, 15]. Successful organ models of the kidneys, liver, heart, lungs and blood vessels have been previously established [13, 14, 15, 16, 17]. Organ-On-Chip technology is compatible with microfluidics and microfabrication protocols, making it suitable for scaling up and also suitable to be applied in the drug development pipeline. The incorporation of microfluidics and cardiac vasculature in a single platform proves to be a reliable alternative for the current gold standards of drug testing, such as animal models and 2D *in-vitro* assays.

1.3 Heart-On-Chip

Cardiomyocytes (CMs) provide the contractility of the human heart. They are arranged in parallel to each other in the form of bundles [18]. Various mechanical, chemical and electrical cues regulate the contractility of cardiac muscles [18, 19]. Additionally, endothelial cells as well as smooth muscle cells contribute to the overall organization of the heart tissue [18]. In order to emulate an accurate biological representation of the human heart in an *in-vitro* environment, it is paramount to consider the complex anisotropic arrangement and composition of the cardiac tissue in addition to the constant exposure to the appropriate dynamic and electrical cues. Till date, there have been multiple Heart-On-Chip platforms that have been developed in an attempt to reproduce the intricate machinery of the human heart, some of which are further elaborated in Section 2.2.1. The research group of Parker et al. [20] designed a Heart-On-Chip platform in which Muscular Thin Films (MTFs) were developed that provide CMs the ability to arrange themselves in an anisotropic manner defined by the patterns on the chip. Moreover, these chips can be incorporated into a micro-fluidic device which provides the dynamic flow needed to recapture the mechanism of blood flow through the chambers of the heart [18]. However, this particular platform does not support the addition of microelectrodes that are required for the electrical stimulation and recording of the electrical response of the electrogenic cardiac cells.

Cytostretch is a Heart-On-Chip device which was developed by TU Delft, The Netherlands in collaboration with Philips, Netherlands (as shown in Figure 1.2). It incorporates various modules such as micro-grooves, micro-electrodes, micro-pores and a stretchable and biocompatible membrane [21]. The flexible membrane can be employed to provide mechanical stimuli that is physiologically relevant to the cells of a living heart [22]. Micro-grooves patterned on the membrane promote alignment of the tissue by providing topological cues to the cardiac cells cultured *in-vitro* [21]. The activity of electro-active cells such as cardiac, neural and muscular cells can be recorded by micro-electrodes embedded in the flexible membrane [21]. The micro-electrodes can also be employed to stimulate such electrogenic cells. The combination of these numerous features makes Cytostretch a versatile Organ-On-Chip device.

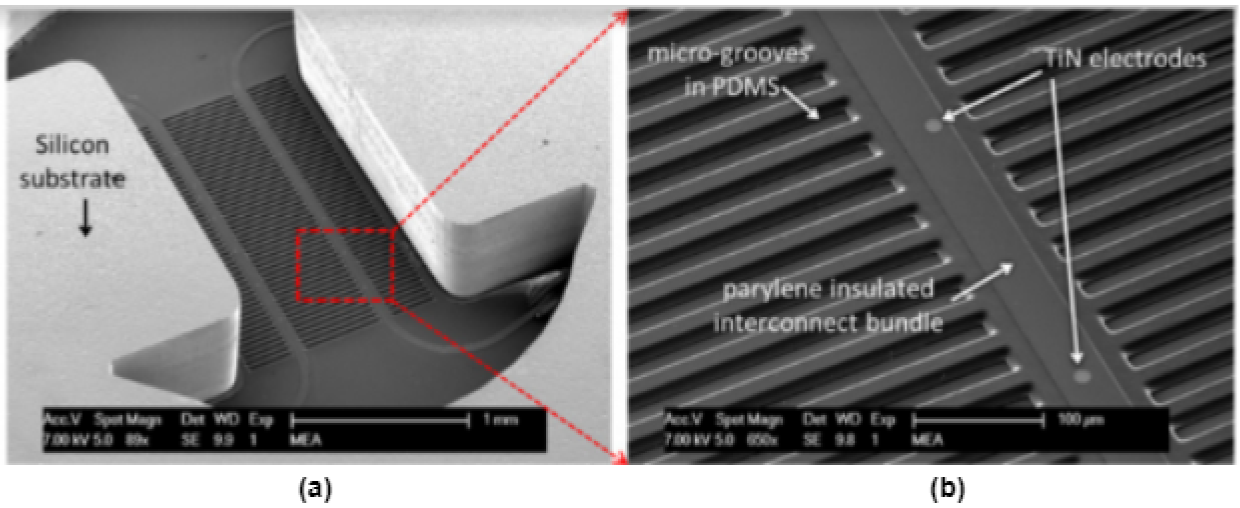

Figure 1.2: Scanning Electron Microscope (SEM) images of the Cytostretch platform: (a) dog bone shaped polymeric membrane, as seen from the back of the device after silicon etching; (b) enlarged image of the metal electrodes encapsulated by parylene insulation and the micro-grooves patterned on the stretchable membrane [23].

The insulating layers which encapsulate the metal electrodes in the device are typically a polymer, like polyimide or parylene. Processing of polymers in a micro-fabrication protocol poses specific challenges with respect to the processing duration, mode of patterning, adhesive properties and cleaning methodology. Although the Cytostretch platform describes a methodology for processing of polymers quite efficiently, it is not yet suitable for large-scale production due to fabrication limitations. Therefore, an alternative insulating material which is also compatible for processing in a silicon micro-fabrication cleanroom needs to be explored. Furthermore, Cytostretch does not provide perfusion which can successfully simulate the dynamic micro-environment of the heart nor does it provide a platform where the cardiac vasculature can be accurately recaptured.

In order to develop a Heart-On-Chip device as an *in-vitro* testing platform for various drug compounds, it is essential to integrate micro-electrodes in the stretchable polymeric membrane which is compatible with standard micro-fabrication techniques. Besides electrical stimulation and recording, the device should be capable of accommodating the different cellular structures of the human heart along with its vasculature, which is in continual exposure to perfusion with fluid. In this manner, a platform that is cleanroom-compatible, scalable and physiologically representative of the human heart can be developed.

1.4 Bi/ond Platform

Bi/ond's Organ-On-Chip (OOC) device is named *inCHIPit*^{TM}, and it is depicted in Figure 1.3. *inCHIPit*^{TM} offers biologists a platform where they can plate their cells of choice on a membrane in an open well and in the micro-fluidic channel incorporated into the membrane with standard pipetting. The advanced perfusion control allows the mimicking of mechanical cues and the supply of nutrients to the cells in order to recreate a human relevant model. In this manner, the cultured cells can be replenished with oxygen and other biological signalling molecules [24]. The combination of the platform and the cell

co-culture can be used to replicate the interactions between an organ and a blood vessel, or between two different organs. Moreover, these devices assist biologists in performing real-time microscopy of the cultured cells by providing a transparent membrane that is suitable for optical imaging. It also has the added ability to stretch samples cultured on the polymeric membrane with physiological accuracy [24]. The membrane can either be connected to a single micro-fluidic channel or a three-channel system, depending on the requirements of the sample.

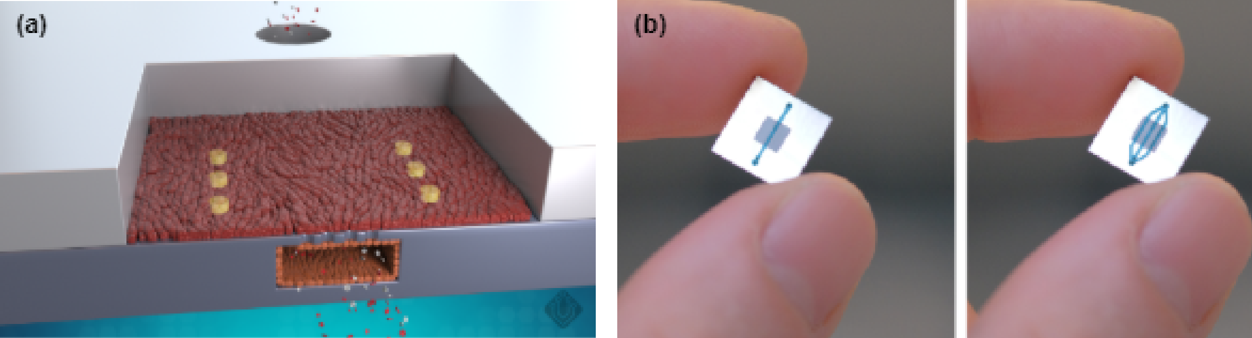

Figure 1.3: Bi/ond device: (a) 3-Dimensional schematic overview of the chip, illustrating the open well integrated with six electrodes and connected to the inlet and outlet of the micro-fluidic channel (b) Photograph of the *inCHIPit*^{TM} platform with a single channel *(left)* and with three channels (*right*) [24].

Till date, the Heart-On-Chip platforms that have been developed either provide the appropriate topological and electrical cues, while being incapable of integrating a compatible perfusion system or, a platform that includes a perfusion system, but lacks electrical cues and the ability to recapture the cellular arrangement of cardiac cells and its vasculature. The Bi/ond OOC device provides an ideal platform in which microelectrode arrays can be successfully integrated. The device also offers micro-fluidic channels that supply the cells with the necessary perfusion to mimic the blood flow through the heart. Moreover, biologists can utilize the *inCHIPit*^{TM} model to seed cardiomyocytes on one side, and endothelial cells of the vasculature of the human heart on the other side of the porous membrane, to closely mimic the structure and arrangement of cardiac tissue.

In order to integrate microelectrodes in the *inCHIPit*^{TM} model certain technological aspects need to be addressed. In some of the current Heart-On-Chip platforms, the metal electrodes are insulated by a polymer, as illustrated in the Cytostretch platform discussed in Section 1.3. Polymers pose issues during the fabrication protocol which makes it non-compatible with high volume production, as elucidated in Section 2.3.2.1. This calls for further research into alternative cleanroom-compatible dielectric materials that can serve as the insulation for the micro-electrodes. Additionally, it is crucial to consider the stress distribution of the metal lines at the interface between the silicon frame and the polymeric substrate, which is further elaborated on in Section 2.3.1. Reports on the development of cracks across the metal electrode structures during the process of dicing have been previously described [24], which requires additional investigation. Therefore, extensive research on viable materials and the design of the electrodes and interconnects along with their respective arrangement is necessary for the incorporation of micro-electrodes in the *inCHIPit*^{TM} model.

1.5 Research Goals and Approach

The major hurdle in the development of reliable Heart-on-Chip models is the ability to provide topological and dynamic cues- such as fluid flow, mechanical stretching, micro-electrode arrays- while simultaneously being able to provide biologists with a platform for performing co-culture assays. Moreover, current microelectrode arrays in OOC platforms are insulated by polymeric structures, which pose challenges during micro-fabrication making it unsuitable for high volume production. Therefore, there exists a need to develop a cleanroom-compatible Heart-On-Chip device that can provide the appropriate electrical stimuli and that is capable of building a biologically appropriate *in-vitro* model of the human heart consisting of cardiomyocytes and endothelial cells of the vasculature. Based on the aforementioned requirements, the goals of this thesis are formulated as follows:

1. Characterization and Compatibility of Silicon Nitride (SiN_x) insulation with PDMS membranes.
2. Optimization of the design and arrangement of the metal lines and membrane designs to improve the yield.
3. Fabrication of a Heart-On-Chip device with micro-electrodes.

To realize the above mentioned objectives of the project, test devices were fabricated in the Else Kooi cleanroom of TU Delft to establish the structural and mechanical integrity of the silicon nitride isolated interconnects during the micro-fabrication process. Test devices were fabricated to evaluate the adhesion between the interconnects and the polymer membrane. Based on the stress models of the Bi/ond platform obtained from COMSOL simulations, the arrangement of the different metal electrodes and the ceramic interconnects were designed. Organ-On-Chip devices with the novel design considerations were fabricated. Furthermore, the metallic electrodes of these devices were characterized via Electrochemical Impedance Spectroscopy (EIS).

1.5.1 Thesis outline

The thesis is further organized as follows: In Chapter 2, details of established OOC models are stated. Issues concerning the use of polymers as an insulating material for metal electrodes are reviewed in Chapter 2, while also the viability of utilizing a ceramic material, like silicon nitride, as an alternative isolation material is discussed. Furthermore, the concepts behind impedance measurements of metal electrodes via electrochemical characterization are further discussed in the Literature Review in Chapter 2. Chapter 3 elucidates the design considerations followed for the arrangement of electrodes and interconnects based on the stress-strain models of the polymeric membrane. The challenges associated with the utilization of a ceramic material as the insulating layer for MEAs in OOC devices are addressed in Chapter 4. Finally, the fabrication protocol of the final device and its characterization are explained in Chapter 5. The final conclusions drawn from this work are stated in Chapter 6.

2 | Literature Review

Despite several scientific advancements, the need for accurate disease models for the precise screening of safe and effective drugs remains unmet. Consequently, numerous drugs have been recalled from the commercial market as a result of the onset of cardiotoxicity in patients. In this chapter, the mechanisms underlying cardiotoxicity and the importance of the development of reliable *in-vitro* platforms for screening of cardiotoxicity in the early stages of drug development are further elaborated. Microelectrode arrays (MEAs) embedded in 2D cell culture substrates are commonly employed for the detection of cardiotoxicity. It is therefore necessary to comprehend the mode of action of MEAs when interacting with biological samples. Important electrochemical properties of various materials currently being employed as electrodes intended for recording and stimulation purposes are further discussed in this chapter. The drive behind the development and advancements made in the field of OOC technology are discussed, while elucidating the designs of some well established OOC models, namely Heart-On-Chip. MEAs can be potentially integrated into OOC devices to predict the safety of cardiovascular drugs to aid in the early detection of cardiotoxicity. The need for the successful integration of MEAs in a Heart-On-Chip platform with the appropriate cardiac co-culture and dynamic mechanisms are emphasised in Section 2.2.1. In order to realize the incorporation of MEAs in a physiologically pertinent OOC platform, such as Bi/ond's *inCHIPit*^{TM} model, various technological aspects require additional investigation, as explained in detail in Section 2.3. Specifically, the approach assumed for the design and arrangement of the electrodes and interconnects based on the stress profile of the OOC platform are discussed. Finally, the challenges pertaining to the processing of polymers, such as polyimide, during micro-fabrication are illustrated. Alternatively, the feasibility of a ceramic dielectric material as an insulator, such as silicon nitride is suggested.

2.1 Cardiotoxicity

Cardiovascular diseases (CVD) are widespread non-communicable diseases affecting millions of people worldwide [18, 25]. Statistics indicate that the incidence of CVD was over six million in the European Union (EU) and over eleven million cases in the whole of Europe in 2019, and is expected to continually increase in the coming years [25]. Therefore, the necessity to develop novel and effective drugs which either treat these diseases or prevent them is of utmost importance. In spite of numerous scientific achievements and technological advances, the overwhelming demand for effective drugs still remains unmet. This is mainly attributed to the fact that the animal models employed for studying the effects of drug molecules do not accurately predict the corresponding human responses [26]. Moreover, the toxicology profile of drugs varies from organism to organism, making it unfeasible to solely rely on the results from the animal models as a criteria to market drugs [27]. Additionally, clinical trials, which represents only a small group of the total population, are not sufficient to effectively determine the specific drug responses [28]. Due to the aforementioned challenges, it is near-impossible to anticipate all the adverse effects of drugs in humans. Cardiotoxicity is a fatal adverse effect of some of the drug compounds and it is the chief driving factor for these drugs to be withdrawn from the market [9]. As a consequence of cardiotoxicity, several non-cardiac drug compounds, such as terfenadine, have also been recalled from markets [29]. The occurrence of cardiotoxicity is not limited to CVD drugs, and nearly a majority of the therapeutic drug compounds have unexpected adverse effects [30]. Cardiotoxicity induces arrhythmia that impair the normal rhythmic heart rate, and in extreme cases can also cause cardiac arrest. Elongation of the QT interval as seen on an electrocardiogram (ECG) is an indicator of cardiotoxicity [31, 32, 33]. Depolarization and the consequent repolarization of the ventricles is represented by the QT interval in an ECG of a healthy human. The QT interval marks the duration of

the electrical activity of the cardiac cells located in the ventricles. The action potential of ventricles is elongated during cardiotxicity, as illustrated in Figure 2.1.

Contraction of cardiac cells is stimulated by action potentials which propagate along different regions of the heart. An action potential originates due to a reversal of the potential across the cell membrane of cardiomyocytes, referred to as depolarization, and terminates with the cardiac cells returning to their original potential, referred to as repolarization [34]. During depolarization, there is an influx of sodium (Na^+) and calcium (Ca^{2+}) ions causing a rise in the potential across the membrane. This occurs when the cells are sufficiently triggered electrically. During repolarization, there is an outflow of potassium (K^+) ions to restore the balance of the membrane potential. Drugs that impede the natural functioning of potassium flow across cell membranes of cardiomyocytes, prolong the process of ventricular repolarization. This abnormal activity of the ventricular cells is linked to the occurrence of arrhythmia [31, 32, 33].

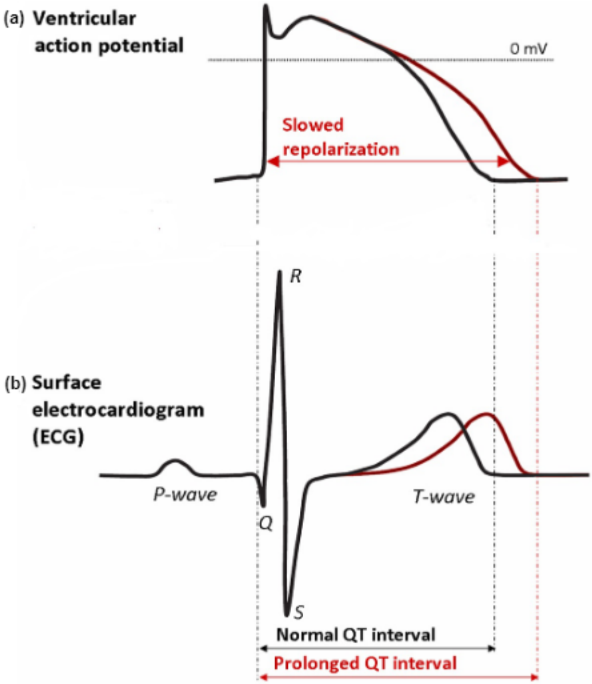

Figure 2.1: (a) Elongation of the duration of the action potential of ventricles during cardiotoxicity, (b) resulting in the elongation of the QT interval of an electrocardiogram (ECG). Adapted from [35].

Detection of cardiotoxicity is mainly carried out by utilizing *in-vitro* models that are capable of measuring the action potential of cardiac cells [36, 37, 38]. Cellular action potential measurements are commonly carried out either directly by the patch-clamp method or indirectly with micro-electrode arrays (MEAs), which are usually embedded in the cell culture substrate.

The cardiac models employed for the detection of cardiotoxicity are mainly focused on measuring the action potential changes in cardiac cells when they are exposed to drug compounds [36, 38, 39]. The gold standards for conducting these measurements include the patch-clamp technique and the use of micro-electrodes. Microelectrode arrays (MEAs), embedded in the 2D cell culture substrate, are popularly employed as tools for detecting cardiotoxicity, mainly by recording changes in the electrical response of the cultured cells when exposed to different drug compounds. In Section 2.1.1, some of the ideal materials and impedance characteristics of MEAs are elaborated.

2.1.1 Measurement of the Electrical Activity of Cardiomyocytes - Microelectrode Arrays (MEAs)

Mechanical, chemical and electrical stimulants applied externally to electro-active cells, such as muscular, neuronal and cardiac cells, results in a change in their electrical responses. The active exchange of sodium, calcium and potassium ions across the cell membrane via their respective ion channels generates

a concentration difference of these ions [40, 41]. The electric potential inside the cell in relation to that of the extra-cellular matrix (ECM) is altered during the flow of ions in and out of the cell. This difference of potential stemming from the ionic concentration difference is detected in the form of an electric signal [41, 42].

The patch-clamp technique is a direct measurement approach, wherein a micro-pipette is utilized to form perforations in the outer membrane of cardiac cells [23]. In this manner, the potential across the membrane can be directly measured under a microscope. Patch-clamping produces precise readings. Nevertheless it is extremely cumbersome to conduct patch-clamp measurements manually and the throughput obtained is relatively low [23].

Micro-electrodes are employed to measure the action potential in an indirect manner. In this technique, cardiomyocytes are cultured on a substrate embedded with micro-electrodes, as depicted in 2.2. The potential inside the cell along with the impedance of the membrane is coupled to the micro-electrode and the output obtained is termed as field potential [23, 43, 44]. MEAs have the added benefit of providing a measurement platform for monitoring the electrical activity for long periods of time without damaging the cells, as in the case of patch-clamp measurements. It also provides a higher throughput than the patch-clamp technique. The MEA measurements usually occur on rigid flat surfaces, which excludes the *in-vivo* physiological conditions [23]. Therefore, incorporation of MEAs in models that can recapture the essential features of the human body is fundamental for the screening of cardiotoxicity.

MEAs are utilized as convenient platforms for studying the activity of electrogenic cells. MEAs find their application in multiple fields, such as [45]: (i) screening of drug compounds [46] (ii) cell-based biosensors [47] (iii) prediction of the safety and toxicity pharmacological profile of drugs [48] (iv) study of the collective behavioural patterns of cells by detecting their extracellular electrical response [49, 50]. Research has also yielded concrete evidence of the possibility of regulating stem cell differentiation to follow a specific lineage when they are stimulated electrically [51].

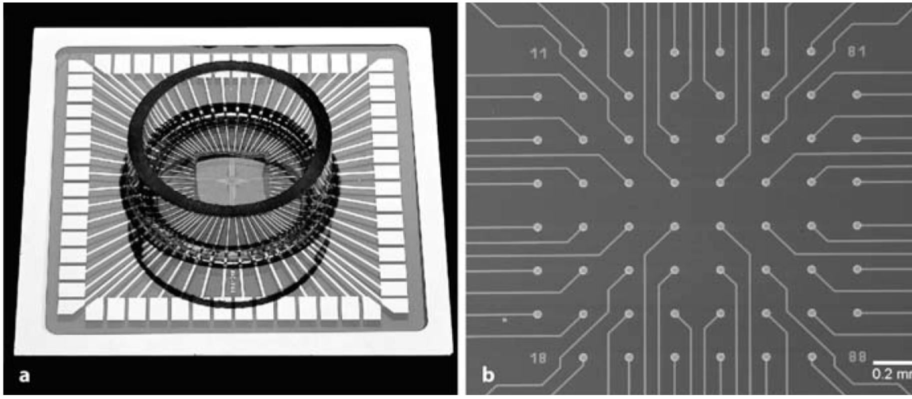

Figure 2.2: (a) A commercialized micro-electrode array (MEA) fabricated using lithography techniques supported by a glass-ring which maintains the cell culture; (b) An overview of the MEA [43].

2.1.1.1 Electrode-Electrolyte Interface

The interface between the electrode and electrolyte is acted upon by a combination of chemical and electrical stimuli, which in turn affects the transfer of charge between the electrolytes in the culture media and the surface of the metal electrodes [52]. Therefore, the performance of micro-electrodes can be analyzed by investigating its electro-chemical properties [53].

When a metal electrode comes in contact with an ionic solution, an electrical double layer is formed at the interface due to the development of a potential difference [54, 55]. The difference in the chemical potential between the solid electrode and the aqueous electrolyte results in charge separation at their interface [56]. Eventually charge distribution across the interface equalizes, establishing a steady potential. At this potential, capacitance is generated at the interface which in turn contributes to the impedance of the metal electrodes [54]. Therefore, micro-electrodes employed for stimulating cells and for recording their electrical responses need to have lower impedance for a better charge distribution at the electrode-electrolyte interface and subsequently better electrical performance.

2.1.1.2 Materials and Electrochemical Properties of MEAs

Titanium nitride (TiN) is commonly employed as the material for micro-electrodes [57, 58]. Titanium is widely accepted as a biocompatible material and as a popular metal for processing in a cleanroom environment [54]. Gold (Au) and platinum (Pt) are also utilized as the metals in commercial MEAs [59]. However, these metals are relatively expensive and pose challenges during fabrication. They are often referred to as "red metals" and face restrictions in their utility inside a silicon micro-fabrication cleanroom environment. Au and Pt electrodes are generally impervious to corrosion with relatively lower values of impedance making them suitable for biological applications [54].

As mentioned previously, the main applications of MEAs during *in-vitro* testing is to either stimulate the electro-active cells or to record the electrical signals of these cells. Stimulation micro-electrodes are commonly defined by their charge delivery capacity (CDC), which refers to the maximum value of charge which can be safely applied to the sample without irrevocably altering the surface properties of the electrode or the neighbouring medium [53, 60, 61]. Whereas, the impedance of the micro-electrodes is the characterizing factor for recording electrodes [53, 62, 63]. Impedance of the electrode is directly related to the noise generated in the recorded electric signal. In order to have a satisfactory spatial resolution, the distance between electrodes and the size of the electrodes must be small [58]. However, with smaller electrode dimensions, the impedance of the electrode increases, which consequently results in a rise of the noise generated in the signal [58]. During electro-chemical characterization of electrodes, the current generated from the electrodes when subjected to an alternating current (AC) oscillating at a single frequency is recorded [64, 65]. These measurements are repeated at different frequencies within the range of investigation, based on which the impedance of the electrodes can be obtained.

In commercially available MEA platforms, the impedance of 30 μm diameter titanium nitride (TiN) circular electrodes is generally less than 100 kΩ [58].

2.2 Organ-On-Chip (OOC) Models

Technological developments have made it feasible to study and accurately regulate the behaviour, adhesion, morphology and distribution of cells in micro-fluidic platforms in the emerging field of *Organ-On-Chip (OOC)* [12]. The fundamental philosophy behind these devices is to successfully replicate the intricate machinery of cells *in-vitro*, while simultaneously providing dynamic signals, such as fluid flow, cyclic stretching and electrical stimuli to the cells [12]. OOC devices also provide cells with the added benefit of interacting with other cell-types in a 3D environment through micro-porous membranes, which consequently resembles the physiology of humans. Incorporation of micro-fabrication techniques makes it viable to scale-up the production of OOC devices. There are certain characteristics which OOC platforms must possess [7, 8]. A model OOC platform must maintain the appropriate micro-environment for studying the interactions at tissue interfaces, which is hard to achieve in the traditional testing methodologies. Additionally, OOC platforms must also offer the right electrical and mechanical environment for the cells, which can be achieved by the integration of recording and stimulating electrodes, and the incorporation of external perfusion components that control the rate of flow of fluids.

Several successful Organ-On-Chip solutions have been developed for multiple organs such as the lungs, liver, blood-brain barrier, kidneys and the heart. Details of the lungs, liver, blood-brain barrier and kidney OOC platforms are further elucidated in Appendix A.1. Heart-On-Chip models are the main focus of this thesis, which is elaborated in the following section.

2.2.1 Heart-On-Chip (HOC)

The heart plays a major role in the circulation of blood throughout the body via the blood vessels. In this manner, oxygenated blood with the essential nutrients reaches different organs in the body, while the deoxygenated blood is redirected to the heart. In order to maintain accurate physiological functionality of the cardiac system in *in-vitro* models, the cellular vasculature organization and the precise dynamic micro-environment of the blood flow is paramount. Heart-On-Chip micro-fluidic platforms provide biologists with the ability to precisely control the above mentioned factors while studying the pathophysioloy and pharmaco-dynamics of the cardiac system [18].

In order to develop a physiologically precise *in-vitro* model of the heart, the endothelial cells and the smooth cells of the vasculature need to be organized in an anisotropic arrangement, with simultaneous presence of mechanical and electrical stimuli [18]. OOC devices are often fabricated by employing PDMS as the polymeric membrane on account of it being biocompatible, inexpensive and non-toxic [66, 67]. Additionally, PDMS can be easily molded into different patterns via soft-lithographic techniques and also serves as an elastomer, making it possible to modulate the stiffness of the polymer depending on the application of the platform. Nonetheless, PDMS, as all other materials, has several drawbacks. Owing to its porosity, small molecules, such as drugs, can diffuse into the material [24]. This in turn affects the bioavailability of drug compounds which influences the results of dose-dependent toxicology studies [24, 68]. This uptake of biochemical compounds can be prevented by covering the surface of PDMS with a layer of cells, or by coating with lipophilic layers [69, 70]. Moreover, by coating the PDMS membranes with proteins forming the extracellular matrix (ECM), challenges associated with the hydrophobicity of the polymer surface can be avoided [18].

Replication of the electrical activity of cardiomyocytes and the anisotropy of these cells are important characteristics that are essential for the successful maintenance of Heart-On-Chip devices [18]. In the human body, the pumping motion of the heart is a result of the stimulation of cardiac cells, which originates in the sinoatrial node. The propagation of the stimuli across the heart through the cardiac cells are periodically depolarized resulting in rhythmic contractions of the heart. The concept of Muscular Thin Films (MTFs) was developed by the research group of Parker at al. [20] wherein cardiac cells and polymer thin films are assembled utilizing micro-fabrication techniques. This was one of the earliest steps taken towards establishing an *in-vitro* model that intimately resembles the physiology of the human heart as illustrated in Figure 2.3. This platform led to extensive studies conducted for measuring the contractile properties of cardiomyocytes and for understanding the propagation of the action potential along cardiac cells [12]. Additional strategies such as integration of electrodes, optically transparent modules for visualization of deformations and introduction of flow of drug compounds widened the application of the MTFs. Grosberg et al. [71] developed a Heart-On-Chip model which was based on the concept of MTF, with the addition of electrodes made of platinum to stimulate the cultured cardiomyocytes.

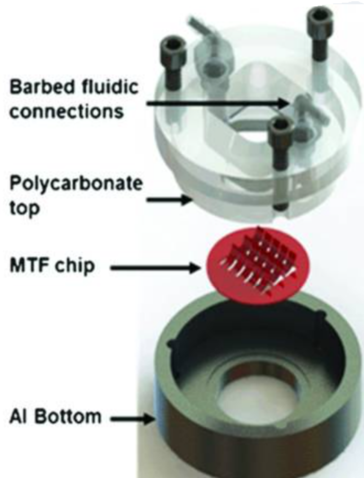

Figure 2.3: A schematic representation of a Heart-on-Chip platform comprising of a Muscular Thin Film (MTF) chip attached to a polymeric micro-fluidic device, which accounts for the dynamic representation of the human heart [18]

The scientific community requires a comprehensive Heart-On-Chip model with all the appropriate electrical, mechanical and dynamic stimuli offered to the cells in a cardiac co-culture. This is necessary to obtain an accurate representation of the cell-cell interactions between cardiomyocytes and the cells of the blood vessels in an *in-vitro* environment. Though the Cytostretch device offers appropriate electrical cues and provides an unique platform to stretch the cells while simultaneously monitoring them, biologists require the added ability to monitor CMs along with its vasculature, as explained in Section 1.3. Also, other Heart-On-Chip models such as those incorporating the MTF technology fail in providing an environment suitable for the inclusion of co-cultures. As previously described in Section 1.4, Bi/ond's *inCHIPit*^{TM} offers biologists the ability to seed cardiac muscle cells in the open well and

endothelial cells of the associated cardiac vasculature in the micro-fluidic channel, enabling researchers to investigate the interactions of the cardiac co-culture under dynamic conditions. Therefore, Bi/ond's OOC device offers one of the best platforms in which micro-electrodes can be successfully integrated, and consequently employed for the fabrication of the most physiologically accurate Heart-On-Chip disease models. Such platforms, with integrated micro-electrodes, are feasible alternatives to a 2D *in-vitro* assay for accurate screening of cardiotoxicity. To realize the incorporation of micro-electrodes in the *inCHIPit*^{TM} device, several technological details require investigation, which are discussed in detail in Section 2.3.

2.3 Design Challenges Of MEAs for OOC Application

To ensure successful stimulation and monitoring of electro-active cells in an OOC platform, micro-electrodes should be designed in a manner where they observe the necessary mechanical, electrical and chemical properties while also complying with the standards of biocompatibility. In order to successfully integrate MEAs in an Organ-On-Chip device, certain technological challenges need to be tackled:

1. The study of formation of cracks during fabrication and the post-fabrication process: The metal electrodes experience considerable stress while traversing the soft polymeric membrane, and finally across the rigid frame of silicon. Significant amount of stress is developed at the interface between the flexible polymer membrane and the rigid silicon frame [23]. Accordingly, by customising the mechanical design of the membrane structure [23] as well as the structure of the metal lines themselves [72], the stress developed can be well distributed to avoid cracks in the metal structures at the interface. Moreover, during the final dicing phase of fabrication, the probability of the metal lines cracking is substantial [24]. This is mainly attributed to the fact that the pressure exerted by the water jet during dicing applies undue stress on the device which is transmitted to the metal lines, thereby breaking the connectivity of the metal structures [24].

2. The electrical insulation to the metal electrodes is currently provided by polymers, such as polyimide and parylene, in a majority of the OOC platforms. Polymers require dedicated equipment for their processing in a silicon-based cleanroom environment, making it difficult to process these structures on a large scale. Polyimide leaves behind a lot of residues after lithographic and etching techniques, as is further explained in Section 2.3.2.1. Additional cleaning steps are necessary in order to fully eliminate issues associated with residues. Moreover, for enhanced adhesion between the polyimide layer and the PDMS membrane, supplementary treatment protocols are required [73]. Etching of a polymer requires an added hard mask, which in turn requires special treatments to improve the adhesion of the hard mask to the polyimide layer. Although PDMS is employed as the membrane material for the current OOC platform, the aforementioned challenges associated with processing of additional polyimide layers can be avoided by investigating the viability of alternate materials for the interconnects.

Based on the above mentioned technical challenges, it is vital to design a Heart-On-Chip platform which can successfully sustain the stress developed during micro-fabrication processes. This can be achieved by innovating a novel design of the membrane which provides a path in which the metal lines can traverse the membrane in a region of minimal stress. These regions of low stress can be determined by performing Finite Element Model (FEM) analysis on the membrane. Based on the results of the analysis, the trajectory of the metal lines in a low stress path can be easily determined, as elucidated in Section 2.3.1. Additionally, it is crucial to look into alternative dielectric materials for insulating the electrodes, without the need for dedicated equipment, as in the case of polyimide processing. Silicon nitride (SiN_x) is a commonly employed dielectric material in micro-fabrication. The details concerning the feasibility of SiN_x as an alternative are discussed in Section 2.3.2.2.

2.3.1 Mechanical Design of Electrodes and Interconnects

The materials and design approaches assumed for the interconnects, running from the metal electrodes to the bond-pads, are crucial for the development of a Heart-On-Chip platform. The interconnects must be capable of sustaining the strain introduced in the elastic membrane when it is stretched in order to reproduce the rhythmic contraction of cardiac cells in an *in-vivo* environment [23, 74]. The materials

frequently utilized for the interconnects in micro-fabrication processes do not possess intrinsic stretching properties, making them unsuitable to be incorporated in a Heart-on-Chip device. Moreover, OOC devices innovated for screening drug compounds should also be feasible for mass production via micro-fabrication techniques. To overcome these restrictions, alternate materials that are both conductive and stretchable need to be adopted. On the other hand, novel distinctive designs of the interconnects can be embodied [23, 75, 76].

Materials that have the innate ability to be stretched, such as elastomers which have a thin layer of metal deposited on them [77], or elastomers embedded with particles that are made of conductive materials [78], or liquid alloys of conductive metals [79] are unfit candidates for micro-fabrication protocols. This is mainly attributed to the difficulty associated with patterning these materials via common lithographic techniques [74]. The other approach for the design of interconnects is to assume a horseshoe shape, or commonly referred to as meanders as shown in Figure 2.4. Meanders increase the surface area which help in distributing the strains over a broad region rather than having the strains concentrated over a smaller region [74]. Research indicates that by substituting straight thin lines of metal with complicated structural designs drastically improves their ability to be stretched [72]. However, the consequent increase in the area occupied by the interconnects restrains the repetitions permitted which in turn restricts the intricacy that can be integrated in a micro-device.

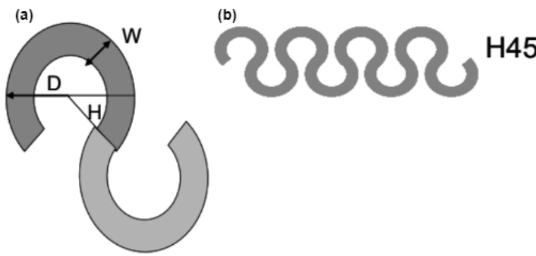

Figure 2.4: (a) Meander design for interconnects specified by three important parameters: the diameter (D), the angle (H) and the width (W); (b) Meanders assuming an angle of 45° are termed as horseshoe shaped meanders [74].

Horseshoes with a width (W) of five micrometers (μm), an angle of 45° and a radius (R) of 100 micrometers (μm) are expected to withstand strain induced by stretching the flexible membrane up to 250%, as depicted in Figure 2.5 [72]. Based on the findings of the research conducted by Sosin, 2011 [72], it is evident that metal lines can endure its elongation with an increased radius together with an increased angle. However, larger radii result in an inadequate utilization of the area available for the metal lines. Taking these into consideration, meander structures with an adequate radius and with an angle of 45° is optimum for interconnects intended to be integrated on a flexible platform.

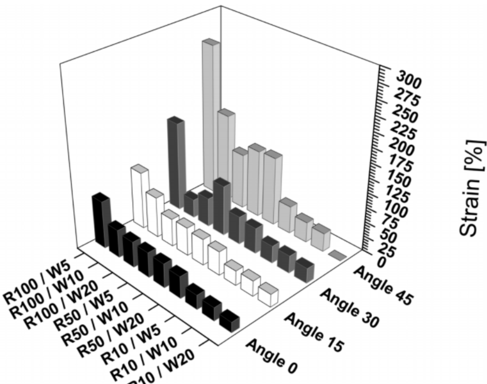

Figure 2.5: The average values of strain sustained by the horseshoe interconnects before their failure for different values of radius (R), width (W) and angle [72].

The strategy adopted by Khoshfetrat Pakazad, 2015 [23] was based on the findings of Finite Element Model (FEM) simulations of the principal strains of the Cytostretch membrane when subjected to

mechanical stretching. From these simulations, the tracks for the interconnects are designed in a manner where they experience minimal stress. The magnitude and direction of the minima (second principal) and maxima (first principal) of the principal strains are commonly used to determine the path for the interconnects [80, 81]. The Cytostretch membrane with the dogbone shape was developed in order to inculcate concave corners which offers an eventual bending moment in the trajectory of the interconnects as it moves from the stiff silicon frame to the flexible polymeric membrane when it is distended. The schematic representation of the dogbone shape assumed for the Cytostretch membrane is illustrated in Figure 2.6.

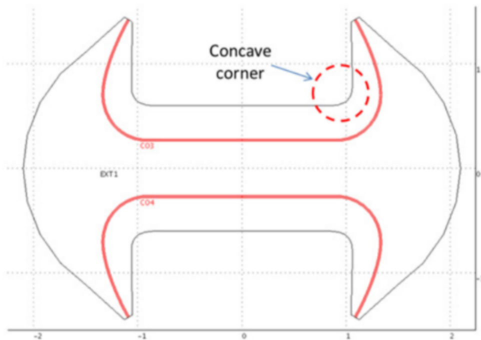

Figure 2.6: The dogbone shape of the Cytostretch membrane comprised of four concave corners. The red lines represent the route assumed by the interconnects [23].

The paths assumed for the interconnect lines in the Cytostretch membrane are such that they are arranged in parallel to the direction of the second principal strain, while simultaneously being perpendicularly organized with respect to the first principal strain [23]. With this arrangement, the lines are exposed to the largest strain in the transverse direction, making them sturdy in this respect. However, the interconnects must be dimensioned in such a fashion that they can endure the longitudinal second principal strain applied to the elastic membrane. Figure 2.7 displays the results of the FEM analysis of one part of the PDMS Cytostretch substrate of 25 μm thickness when it is stretched by a pressure of 10 kPa.

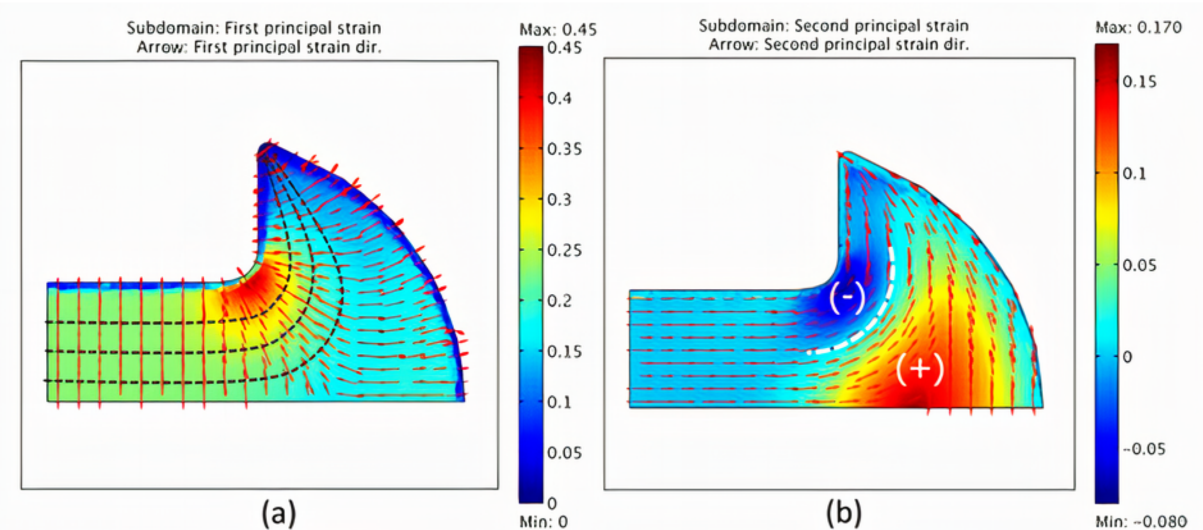

Figure 2.7: Principal strain directions sustained in one corner of the Cytostretch membrane. (a) Directions of the first principal strain, as indicated by the red arrows. The dotted black lines represent the possible multiple tracks for the interconnects; (b) Directions of the second principal strain. The white lines indicate the path for the interconnects where they experience zero strain [23].

Incorporating the design rules mentioned above, multiple paths for the lines are presumed, as depicted by the black lines in Figure 2.7 (a). The magnitude of the second principal strain assumes a negative value in the region close to the concave region, which eventually changes to a positive value while

following a trajectory which leads to the central region of the membrane, as seen in Figure 2.7 (b). In consequence, there exists a narrow path in the membrane, termed as the "zero-crossing path", near each of the four corners where the lines experience virtually zero stress, making this an optimal route for the interconnect lines [23].

Figure 2.8 (a) displays the effect of the interconnect path on the distribution of the strain in the PDMS membrane, while Figure 2.8 (b) illustrates the magnitude of the strain developed in the path followed by the interconnect.

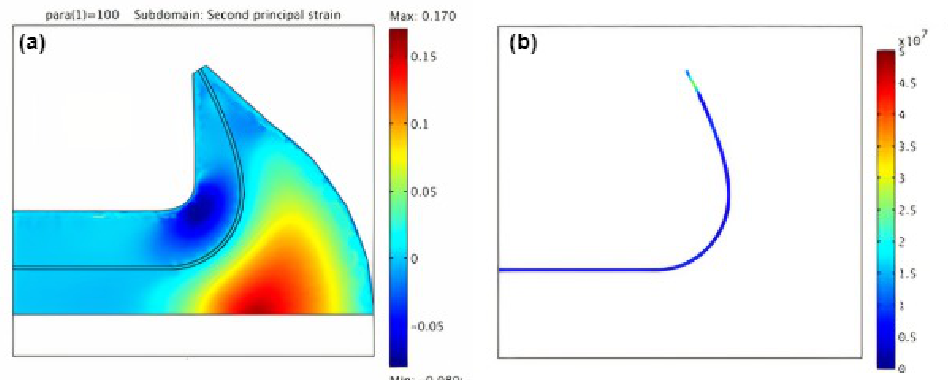

Figure 2.8: (a) The effect of the interconnect track on the magnitude of the second principal strain in the Cytostretch flexible membrane; (b) The stress developed in the interconnect with a width of 20 μm and a thickness of 4 μm [23].

Stress develops in the interconnect lines when they are transitioning from the unbending silicon substrate to the flexible polymer. This is termed as the bending stress (σ), which is related to the radius and the thickness of the bending path as follows:

$$\sigma = E\frac{t}{r} \tag{2.1}$$

Where, σ is the bending or flexural stress, E is the Young's modulus of the material of the interconnects, t is half the thickness of the interconnect and r is the bending radius [23]. With the dogbone design of the Cytostretch membrane, the bending radius of the interconnects is increased due to the incorporation of the concave corners. In this manner, the stress experienced by the interconnects along their trajectory displays only a moderate change while traversing from the elastic membrane to the stiff frame.

Figure 2.9 depicts the cracks developed in the titanium nitride (TiN) lines during the dicing process. The pressure exerted by the water jet on the silicon wafers during dicing consequently breaks the continuity of the interconnects, thereby causing the electrical connections to discontinue [24]. By designing shorter interconnects, it is possible to reduce the frequency at which cracks develop in the interconnects [24].

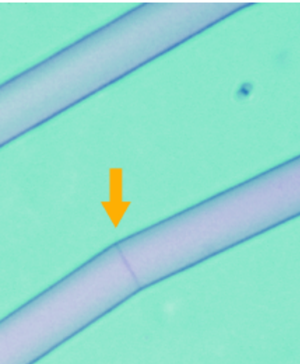

Figure 2.9: Cracks observed in the metal (Titanium nitride, TiN) lines after the dicing process as shown by the yellow arrow [24].

The design principles utilized for formulating the final design and integration of micro-electrodes in

Bi/ond's *inCHIPit*^{TM} OOC platform are based on the aforementioned strategies, which are further elucidated in Chapter 3.

2.3.2 Insulation Materials

Micro-electrodes integrated in an OOC platform need to be electrically isolated from the conductive cell culture medium. Therefore, it is necessary to investigate the properties and feasibility of commonly employed insulation materials in current micro-fabrication techniques.

2.3.2.1 Polyimide Insulation

Polyimide (PI) is a thermosetting polymer which finds application in various fields. Research has proved the use of PI as a structural layer, a sacrificial layer, a photoresist and also as a substrate in certain MicroElectroMechanical Systems (MEMS) devices [82]. PI is a multifaceted material owing to its property of being able to accommodate various chemical compounds into its core composition [82]. In this fashion, the properties of the material can be easily tailored to suit the application. They also prove to be inert to chemicals [82]. During the fabrication of micro-electrodes, its dielectric properties make it highly suitable as an electric insulator for the metal lines [83].

Despite the many advantages offered by polyimide, the processing of a polymer in a cleanroom is still a challenging operation. Polymers, in general, require a longer time to be cured. PI needs to be manually coated on the sample in the liquid form, and later on requires to be cured thermally to form a layer [84]. Additionally, polymers like PI require dedicated equipment that is specifically reserved for their processing.

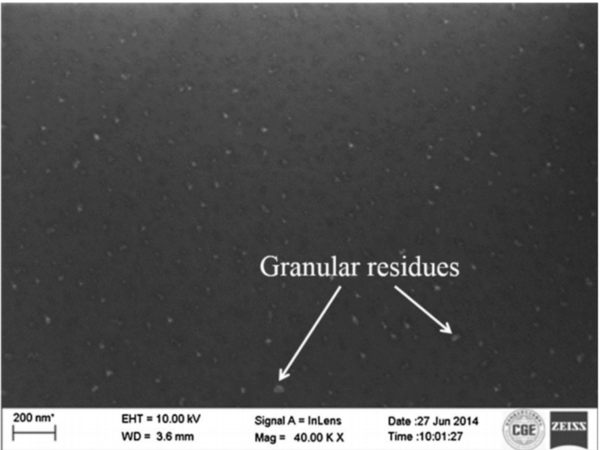

Figure 2.10: SEM image of a MEMS device with polyimide insulating layers post Deep Reactive Ion Etching (DRIE) process. Granular residues remain on the surface of the device after plasma treatment [85].

Furthermore, processing a polymer, such as PI, via lithographic techniques leaves behind residues, as depicted in Figure 2.10. These residues pose issues related to the adhesion, reliability and electrical properties of polyimide [85]. It is therefore necessary to ensure that all the residues produced during processing are completely removed. Hence, additional processes need to be performed in order to fully remove the residues. This includes an oxygen plasma treatment [85]. Oxygen atoms in the plasma interact with the organic residues to form products that are volatile and can subsequently be removed from the device [86]. In most cases, an oxygen plasma treatment is insufficient for the complete elimination of the residues, and an additional wet stripping process is required [85].

Polymer patterning requires either a hard-etch mask or a resist-mask [73]. Generally, the type of mask selected depends mainly on the etch selectivity of the mask. During the dry etch process of PI, the presence of oxygen in the etch chamber renders the etch selectivity towards the resist weak [73]. Due to this, both the resist and the polymer are etched at the same rate. One strategy to overcome this is to employ a thick resist as a mask, which results in a low lithographic resolution. Utilization of a hard-etch mask is a more commonly employed fabrication technique for patterning a polymer. These masks are

often metals like aluminium, titanium or molybdenum that are uninfluenced by the chemistry of the plasma etch of polymers [73]. However, etching of PI using an aluminium hard-mask produces "fur-like" residues, as illustrated in Figure 2.11. It has been reported that the adhesion of metals to polyimide is inadequate due to the poor surface energy of the untreated polymer [87]. Therefore, to improve the adhesion properties of PI, an argon sputter-etch is suggested [87].

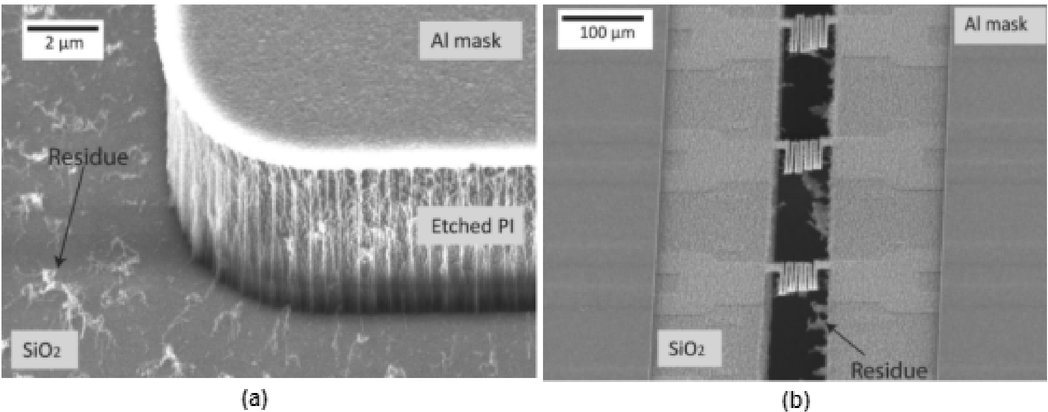

Figure 2.11: (a) Residues observed on the silicon oxide layer after etching of polyimide using an aluminium (Al) hard mask; (b) "Fur-like" residues seen on the device with free-standing interconnects after etching of polyimide [73].

Although polyimide has been utilized as an electrical insulator for metal electrodes, based on the above mentioned drawbacks, it is necessary to research the feasibility of alternative materials.

2.3.2.2 Silicon Nitride Insulation

Silicon nitride (SiN_x) is a ceramic material that is commonly utilized in micro-fabrication. Owing to its excellent chemical, mechanical and physical properties, silicon nitride is favoured as the layer to be deposited on silicon substrates during the fabrication of various devices. Some of its salient properties include [88]:

- Good thermal stability
- Resistant to corrosion
- Reliable optical absorption characteristics
- Remarkable mechanical attributes
- Good dielectric properties

It has been previously applied as a barrier layer in fabrication [89]. Silicon nitride is also generally employed as an electrical insulator [89], like the MEA developed by Multichannel Systems (MCS). Silicon nitride is either thermally grown in a furnace or deposited via vapor deposition techniques. A layer of silicon nitride can be patterned easily with a resist-mask, without the requirement for additional surface treatments to improve adhesion or the need for a hard-mask, as is the case with the processing of polymers. Therefore, the processing of SiN_x layers via common lithographic techniques makes it a more attractive material as an electrical insulator. Furthermore, since SiN_x is an inorganic material, the challenges associated with cleaning of the wafers after the etching process are eliminated. It does not leave behind any residues on the surface during the etching process, as in the case of polymer etching (Figure 2.10).

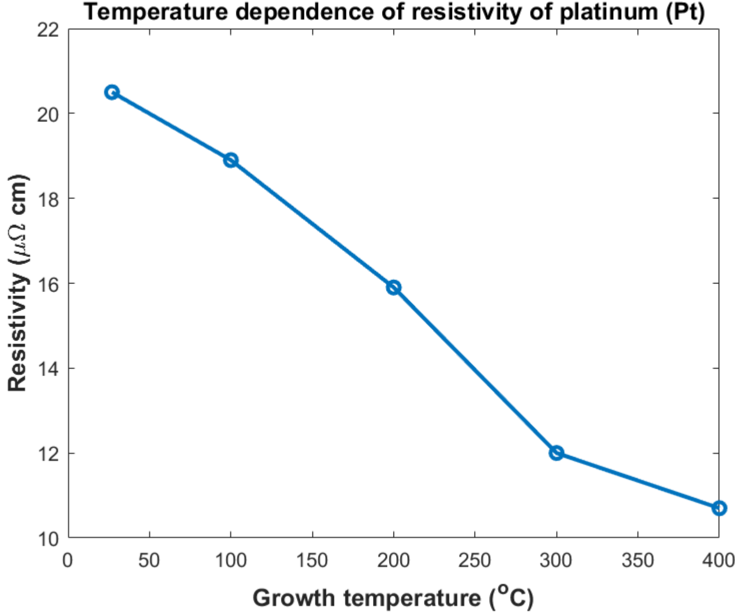

Figure 2.12: Sputtering temperature dependence of the resistivity of platinum (Pt). Adapted from [90].

One of the added benefits of choosing a ceramic material as an insulator for micro-electrodes is the ability to sputter metals and metal-alloys like titanium nitride (TiN) at higher temperatures, around 350°C. Polymers, such as polyimide, are not suitable to withstand higher temperatures during metallization. The preference to sputter metals at higher temperatures is two-fold: (i) Sputtering duration is drastically reduced at higher temperatures; (ii) At higher temperatures, the metal atoms have more energy to arrange themselves in a compact manner, resulting in a lesser resistivity. This trend is illustrated in Figure 2.12 which depicts the reduction in the room temperature resistivity of the sputtered platinum with higher deposition temperatures. This can be attributed to the increase in the grain size of the metals with increasing sputtering temperatures [90].

3 | Mechanical Design of the MEA

The development of an ideal Heart-On-Chip platform requires several technological aspects to be considered. As stated in Section 2.3.1, the metal interconnects should be capable of withstanding the stress introduced during the fabrication process and consequently during the post-fabrication process of dicing. The metal interconnects can be designed to occupy a larger surface area, as in the case of meandering structures. These structures help to redistribute the strains over a larger region and can therefore better accommodate the stress developed during the fabrication protocol [74]. Previous studies have indicated the increased ability of intricate structures, such as meanders, to withstand stress, making them a viable design option when building a Heart-On-Chip device [72].

The design of the interconnects were determined by performing FEM analysis to obtain the optimum trajectories while traversing across the interface between the PDMS membrane and the silicon frame. From the FEM simulations, information regarding the magnitude and direction of the maximum (first principal) and minimum (second principal) strains developed in a stretchable platform can be obtained [23, 80, 81]. This is crucial for establishing the ideal routes for the interconnects where they experience the lowest stress. The interconnects are designed such that they are arranged in parallel to the direction of the second principal strain while simultaneously being perpendicularly organized with respect to the first principal strain [23]. Accordingly, the lines can be appropriately positioned in the flexible PDMS membrane to ensure they experience the least amount of stress.

In this chapter, the multiple designs assumed for the metal interconnects are elaborated, based on the findings obtained from FEM analysis. This design methodology adopted for two different designs namely, the *oval* and the *turtle* designs are further explained in the upcoming sections. Additionally, the strategy utilized for the design of the meander structures as well as for the straight interconnects are illustrated in the following sections.

3.1 The Oval Design

The *oval* platform of Bi/ond is utilized as the base for the development of a HOC platform equipped with micro-electrodes. The development of the *oval* shape membrane was inspired by the design of the Heart-Dyno system, where the shape of the cell culture substrate is of an elliptical geometry [91]. In this platform, the elliptical substrate also comprises two elastomeric posts which promotes thick cardiac muscle bundles to condense around these pillars [91]. Figure 3.1 illustrates the 3D rendering of a chip that is fabricated with the oval design developed by Bi/ond, wherein multiple modules can be potentially integrated in the PDMS membrane which is supported by the rigid silicon frame. In the *oval* design, the PDMS membrane assumes an oval geometry of 2x3 mm. The platform was designed to provide appropriate mechanical stimuli to the cell culture by means of stretching the polymeric membrane. Additionally, it can also be equipped with micro-pores to provide relevant dynamic fluid perfusion to the cardiomyocytes and endothelial cells cultured across the open well. Micro-pillars can also be incorporated into the platform to aid in investigation of the biomechanics of cells adhered to the membrane, and to facilitate the formation of cardiac muscle bundles [91, 92]. Moreover, MEAs can be potentially integrated in the membrane of the oval platform in order to detect and monitor the activity of electrogenic cells.

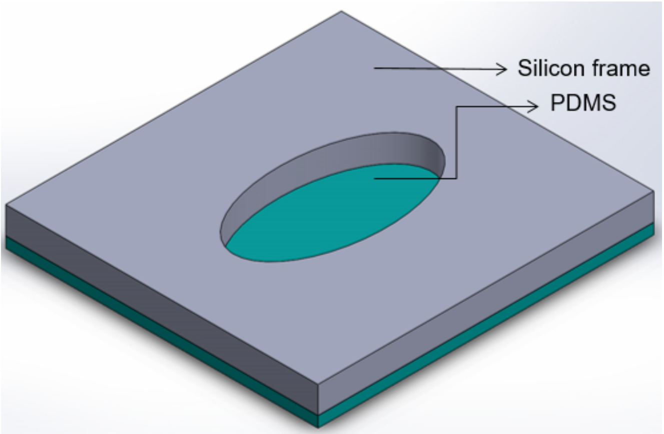

Figure 3.1: 3D rendering of the Bi/ond *oval* platform in which the MEA is integrated. The figure is not drawn to scale.

The *oval* geometry was utilized to perform FEM analysis in order to obtain information regarding the principal strains that act on the PDMS membrane when subjected to an external pressure. Inspired by previous studies, the trajectories assumed by the interconnects on the stretchable membrane should be such that they are arranged perpendicularly with respect to the direction of the first principal strain [23]. Moreover, it is necessary to design the interconnects in a region of minimal second principal strain [23]. Figure 3.2 illustrates the magnitude and the direction of the first principal strains developed in the *oval* PDMS membrane when it is subjected to an external pressure. As depicted, the first principal strain acts along the transverse direction towards the center of the ellipse, while acting radially towards the periphery of the membrane. At the interface, a maximum strain of ∼30% was obtained.

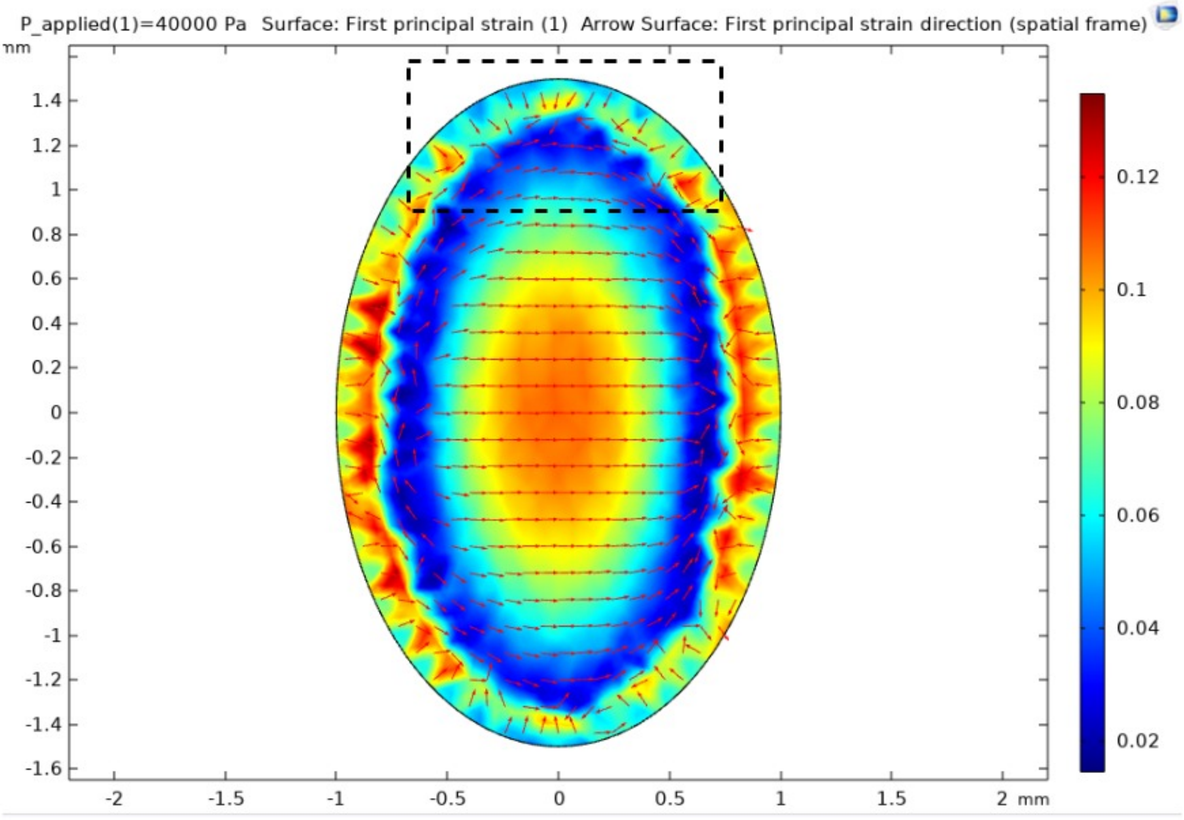

Figure 3.2: Magnitude and direction of the first principal strain developed in the *oval* membrane when it is subjected to an external pressure. The rectangular box marked by the black dashed lines depict the area where the magnitude of the first principal strain at the interface is relatively low.

In Figure 3.3, the magnitude and direction of the second principal strain acting on the oval membrane is illustrated. It can be seen that the magnitude of the second principal strain is positive towards the central region of the oval and eventually becomes negative at the periphery of the oval. Accordingly, a region of virtually zero second principal strain is defined, which is depicted by the region within the black dashed lines in Figure 3.3. It can be seen that regions of zero-second principal strain cannot be obtained at the interface between the *oval* PDMS membrane and the silicon frame.

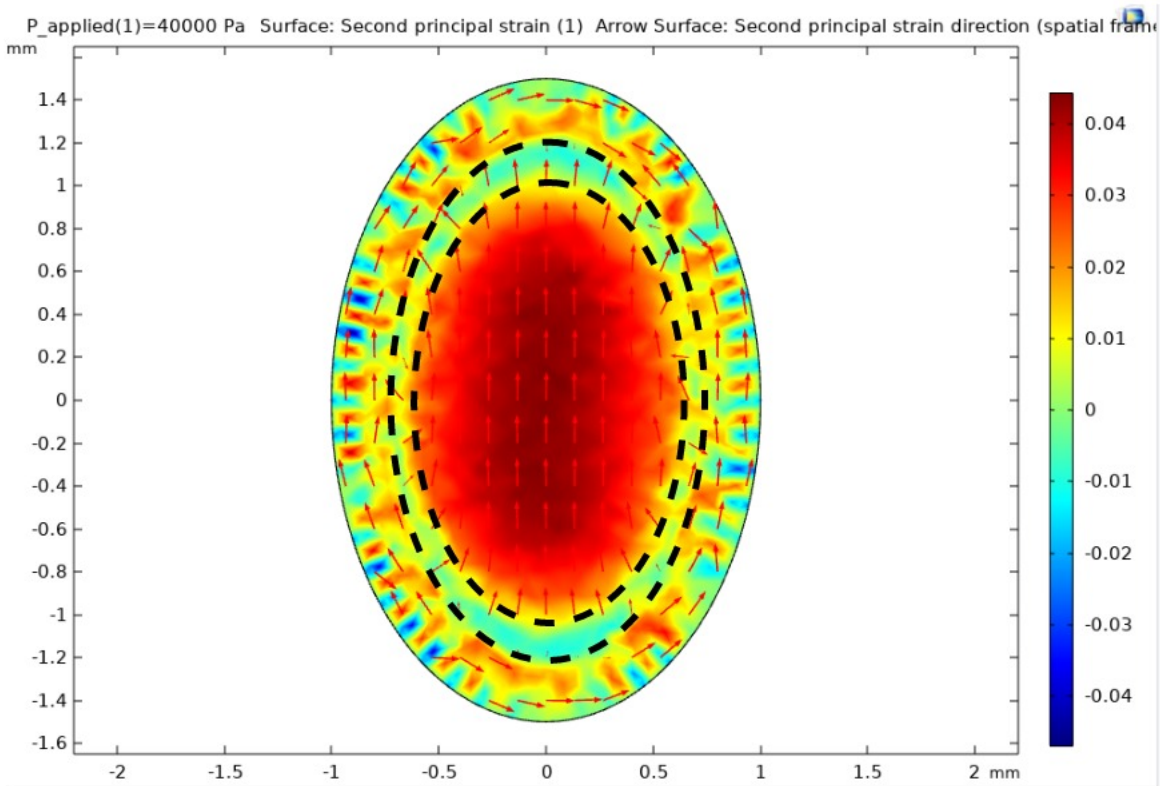

Figure 3.3: Magnitude and direction of the second principal strain of the *oval* PDMS membrane when subjected to an external pressure. The smaller concentric ellipse enclosed within the black dashed lines represent the regions of zero-second principal strain.

As depicted in Figure 3.2 and Figure 3.3, the stress analysis obtained for the *oval* membrane defines a smaller concentric oval region where the magnitude of the second principal strain is minimum and where the direction of the first principal strain is perpendicular to the major axis of the ellipse. Taking the previously mentioned design rules into consideration, the trajectories assumed for the interconnects in one-half of the *oval* PDMS membrane is illustrated in Figure 3.4.

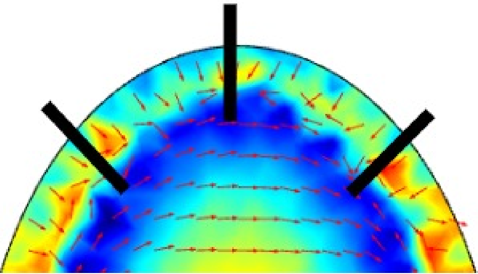

Figure 3.4: The direction of the first principal strain, indicated by the red arrows, acting on one half of the *oval* membrane when subjected to an external pressure. The black lines depict the trajectories assumed for the interconnects when traversing from the membrane to the silicon substrate.

It can be seen that there exists an issue with the symmetries in the simulations of the principal strains

(Figures 3.2 and 3.3). This is mainly due to the larger mesh size utilized for these simulations. Further analysis of the stress distribution in the membrane was made to effectively position the electrode openings in regions of low stress. The simulation results of one-quarter of the *oval* membrane indicates a smaller concentric oval-shaped region, of 0.4 mm, where the magnitude of the principal strains are smallest, as depicted in Figure 3.5. Therefore, we decided to place the electrode openings in this region. We decided to investigate both *short* and *long* interconnects. Accordingly: (i) *short* interconnects, with the electrode openings at a distance of 300 μm from the outer periphery of the membrane, and (ii) *long* interconnects, with the openings for the electrodes positioned at a distance of 500 μm from the outer boundary of the membrane, were designed.

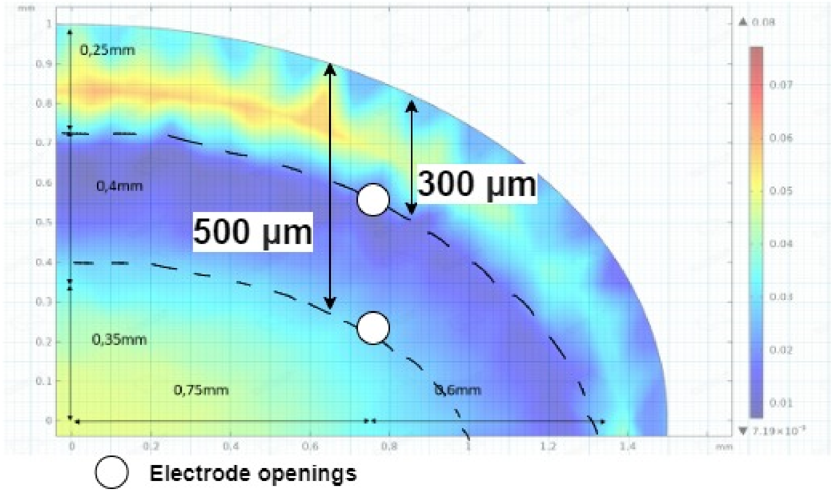

Figure 3.5: The different ranges of the magnitude of the principal strains acting on one-quarter of the *oval* membrane when subjected to an pressure. A region of minimum strain is defined (indicated by the black dashed lines), which approximately spans a distance of 0.4 mm from the outer periphery of the *oval* membrane.

Moreover, we decided to look into the effect of different interconnect shapes on the stress developed while traversing along the PDMS membrane and eventually across the rigid frame of silicon. As mentioned previously in Section 2.3.1, horseshoe-shaped meanders help to redistribute the strains over a broader area [74]. Therefore, we developed interconnects with two different designs: (i) *straight* lines (Figure 3.6 (a)), and (ii) *meanders*, as depicted in Figure 3.6 (b).

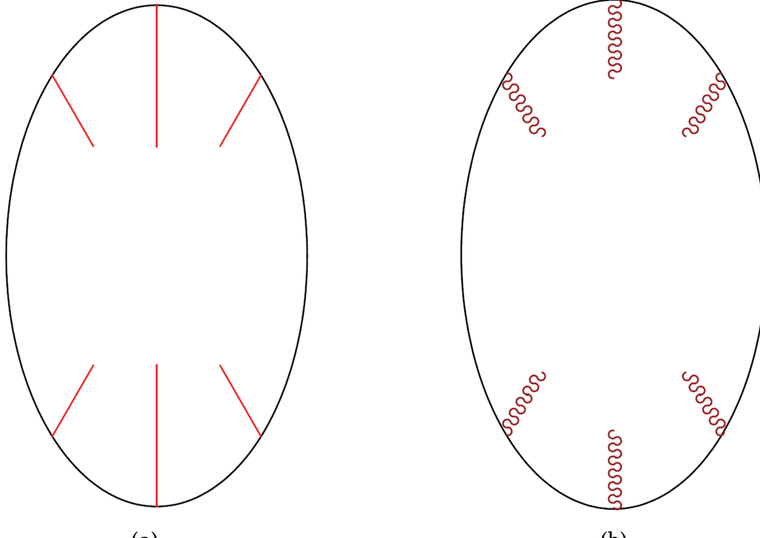

Figure 3.6: The schematic representation of the oval design. The interconnect tracks are represented by the red lines. (a) The arrangement of six straight interconnect lines; (b) The arrangement of six interconnects which are designed in the form of meanders. The figures are not drawn to scale.

The width of the interconnects also influences their mechanical integrity during the fabrication process and, consequently during the mechanical stretching of the polymeric membrane [72, 93]. By employing narrow metallization strategies for designing the interconnects, a minimum concentration of strain along the structures can be obtained [93]. Therefore, we decided to design the metal lines with different widths: (i) *thin* lines of 10 μm, and (ii) *thick* lines of 30 μm.

The mask designs for the interconnects with different shapes (*straight* and *meanders*), different lengths (*short* and *long*) and with different widths (10 μm and 30 μm) on the *oval* membrane are illustrated in Figure 3.7 and Figure 3.8.

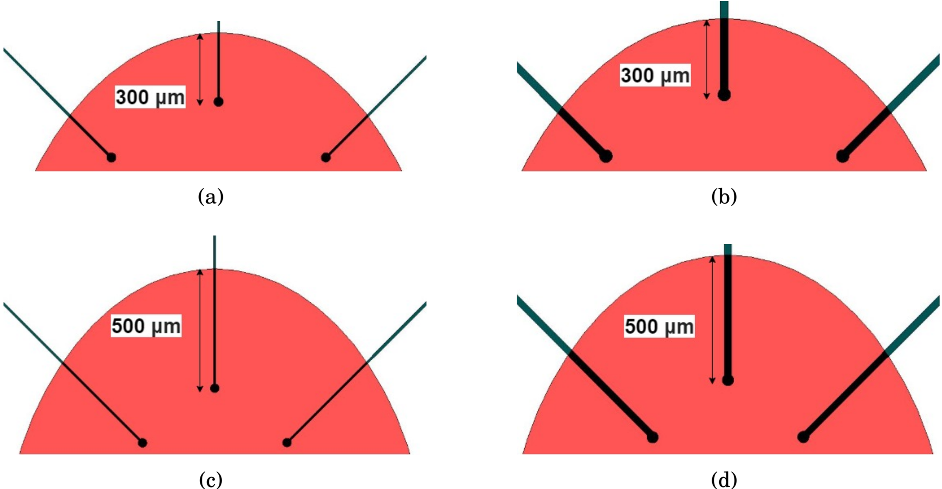

Figure 3.7: Different designs of the *straight* metal lines and the interconnects in one half of the oval membrane: (a) Shorter metal lines with a width of 10 μm; (b) Shorter metal lines with a width of 30 μm; (c) Longer metal lines with a width of 10 μm; (d) Longer metal lines with a width of 30 μm.

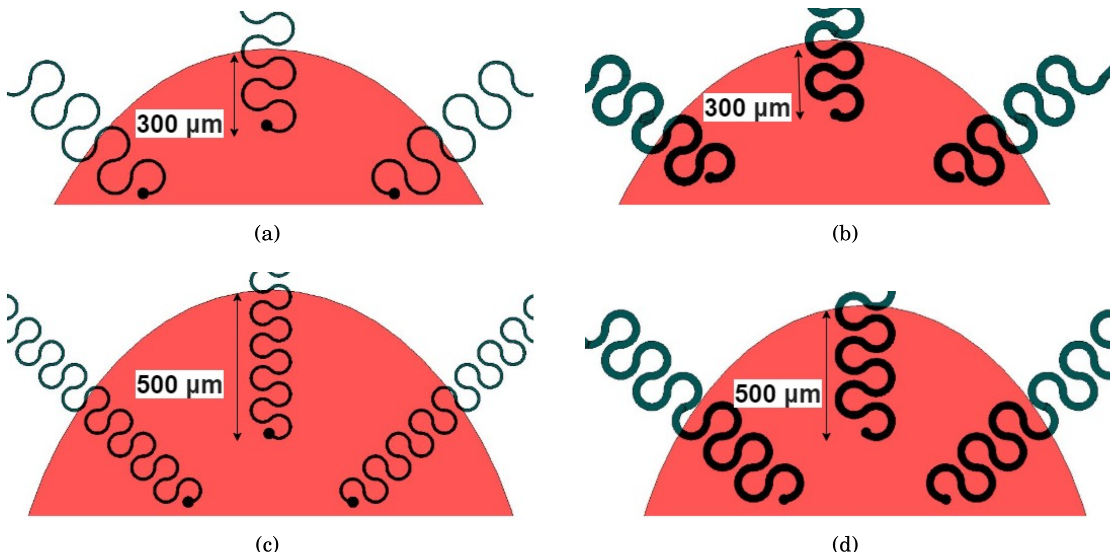

Figure 3.8: Different designs of the horseshoe-shaped *meanders* as the metal lines and the interconnects in one half of the oval membrane: (a) Shorter meanders with a width of 10 μm; (b) Shorter meanders with a width of 30 μm; (c) Longer meanders with a width of 10 μm; (d) Longer meanders with a width of 30 μm.

Based on the simulations performed for the *oval* membrane, regions of zero-second principal strain are not defined at the interface of the membrane and the silicon substrate, as shown in Figures 3.2, 3.3 (b). Consequently, the interconnects passing through these regions are subjected to stress, thereby increasing the possibility of cracks during the post-fabrication process. Therefore, with the *oval* design it is not feasible to obtain a trajectory where the interconnects develop minimal stress while traversing across the membrane to the silicon substrate. However, we were able to achieve regions of virtually zero second principal strain at the interface by modifying the geometry of the *oval* membrane. We formulated novel membrane designs which address the issues of stress along the path of the interconnects to improve the yield of the metal lines during the fabrication process, which is explained in the following section.

3.2 The Turtle Design

To obtain optimum trajectories for the interconnects while moving from the PDMS membrane to the silicon frame, regions of zero-second principal strain need to be identified at the interface. With the *oval* design, these regions of low stress cannot be achieved. Therefore, we developed new membrane designs by including progressively tapering extensions in the *oval* membrane, as shown in Figure 3.9. These novel designs are referred to as the *turtle* designs. The extensions of the *turtle* membrane defined for accommodating the meanders are wider in comparison to the extensions defined for the straight interconnect lines. Figure 3.9 (a) depicts the *turtle* geometry with the wider extensions. While, Figure 3.9 (b) depicts the *turtle* membrane with the extensions intended for the straight interconnects. With the *turtle* geometry, the accumulation of stress at the interface was reduced drastically, as explained in the following section.

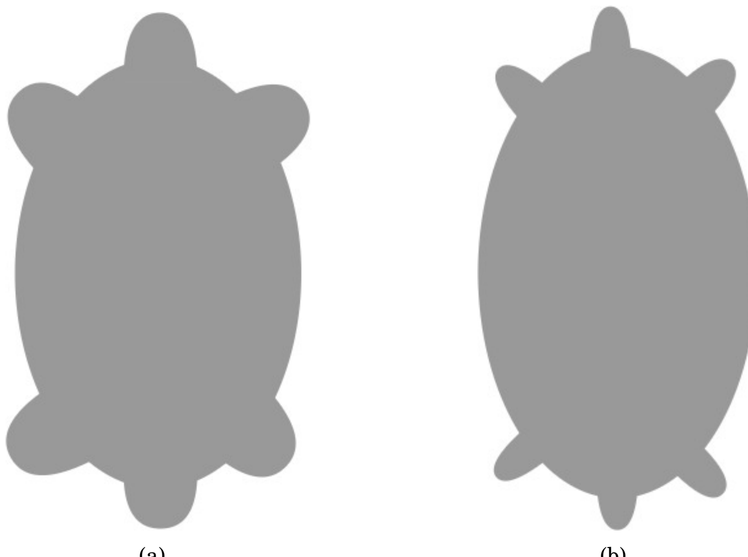

Figure 3.9: Mask designs of the *turtle* membrane. (a) The geometry of the *turtle* membrane accommodating the meandering interconnects; (b) The design of the *turtle* membrane for the straight interconnects. The figures are not drawn to scale.

The above mentioned *turtle* geometries were utilized for the FEM analysis. Figure 3.10 illustrates the magnitude and direction of the first and second principal strains acting on the novel *turtle* shaped membranes when subjected to an external pressure. Figure 3.10 (a) depicts the direction of the first principal strain, as shown by the red arrows. While, Figure 3.10 (b) is a 3D representation of the first principal strain distribution across the *turtle* membrane designated for the meander interconnects, when it is inflated. In Figure 3.10 (c-d), the 2D and 3D illustration of the first principal strain across the *turtle* membrane intended for the straight interconnect lines are shown.

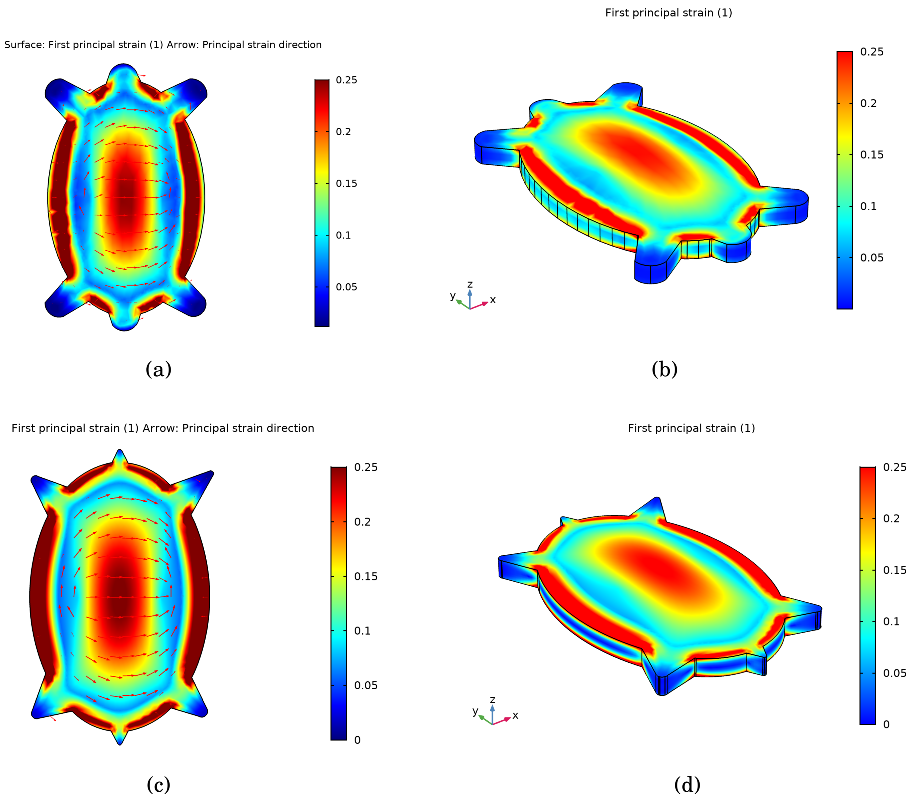

(a) (b) (c) (d)

Figure 3.10: The magnitude and direction (indicated by the red arrows) of the first principal strains acting on the *turtle* PDMS membrane when subjected to an external pressure: (a-b) Results of the FEM analysis for the membrane defined for the *meander* interconnects; (c-d) Direction of the first principal strain (indicated by red arrows), for the membrane to accommodate *straight* interconnects, along with its 3D representation.

Similarly, Figure 3.11 (e-f) represents the magnitude and direction (depicted by the red arrows) of the second principal strain in the *turtle* membrane for the meander shaped interconnects. Figure 3.11 (g-h) illustrates the second principal strain profile of the *turtle* membrane for the straight interconnect lines.

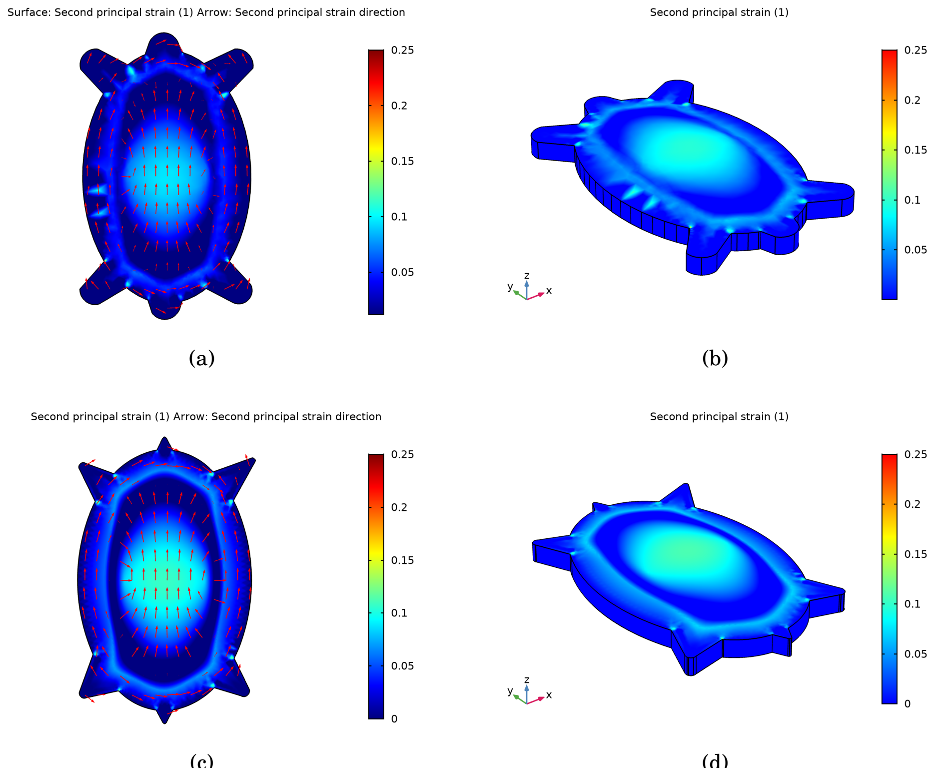

Figure 3.11: The magnitude and direction of the first and second principal strains acting on the *turtle* PDMS membrane when subjected to an external pressure. (a-b) Second principal strain profile and its 3D illustration of the membrane designed for the *meanders*; (c-d) Second principal strain profile and its 3D illustration of the membrane designed for the *straight* lines.

Three optimum trajectories obtained for the interconnects in one half of the *turtle* membrane, based on the magnitude and direction of the principal strains, are depicted in Figure 3.12 (regions of dark blue). These paths are defined in regions of near zero principal strains (∼5%). In comparison to the *oval* geometry, which develops a strain of ∼30% at the interface, the *turtle* membrane displays ∼83% reduction in the strain at the interface. It is at these regions that the optimum trajectories for the interconnects are defined.

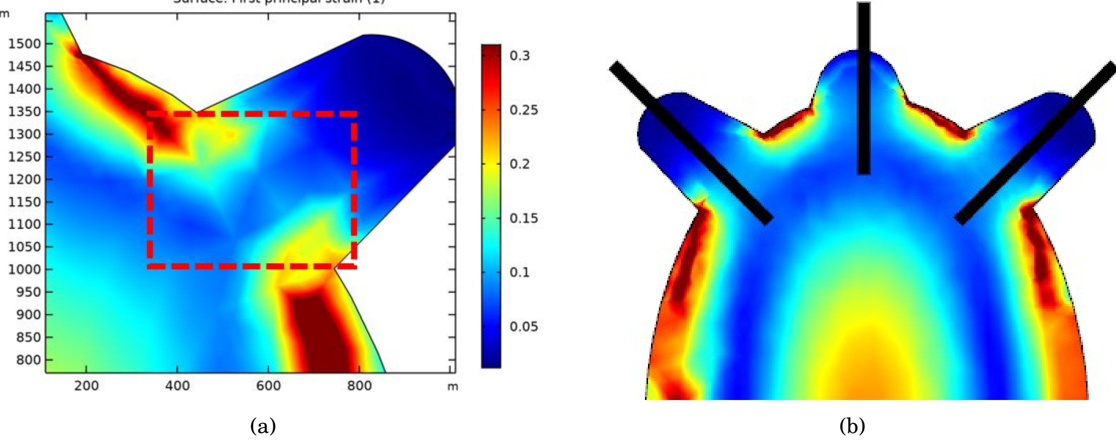

Figure 3.12: The magnitude of the first principal strain acting on one half of the *turtle* membrane when subjected to an external pressure. (a) The region marked by the red lines depict the area of interest, where the maximum strain obtained is ∼5%; (b) The black lines depict the trajectories of the interconnects when traversing from the PDMS membrane to the silicon substrate.

Figure 3.13 illustrates the influence of the interconnects on the stress profiles of the *turtle* membrane. In Figure 3.13 (a), the influence of the addition of the straight interconnect lines on the distribution of the first principal strain is shown. Figure 3.13 (b) depicts the 3D representation of the effect of the straight interconnects on the second principal strain.

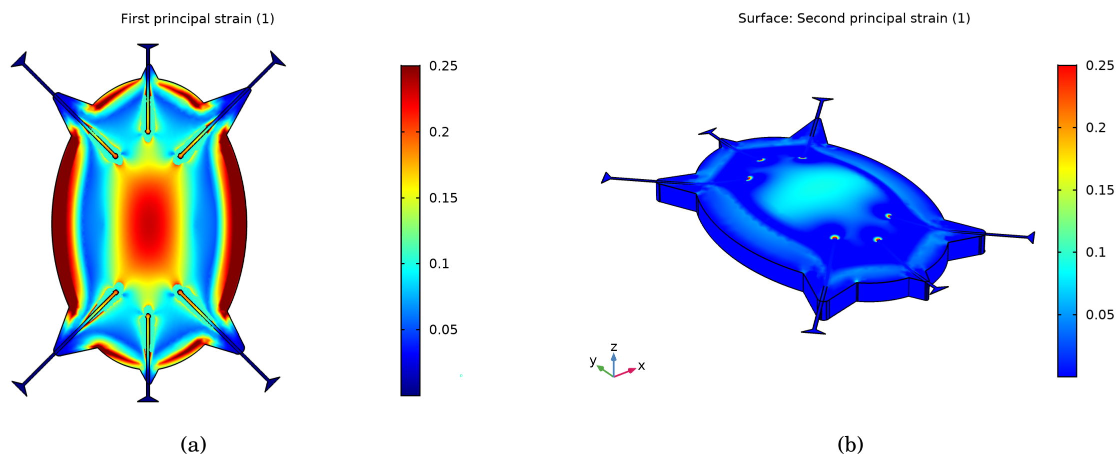

(a) (b)

Figure 3.13: The influence of the interconnect paths on the stress distribution of the *turtle* membrane. (a) The distribution of the first principal strain when *straight* interconnects were integrated on the membrane; (b) 3D representation of the influence of the *straight* interconnect lines.

We designed the interconnects as: (i) *straight* lines, and (ii) *meanders*, for the *turtle* membrane. The schematic representation of these designs are illustrated in 3.14.

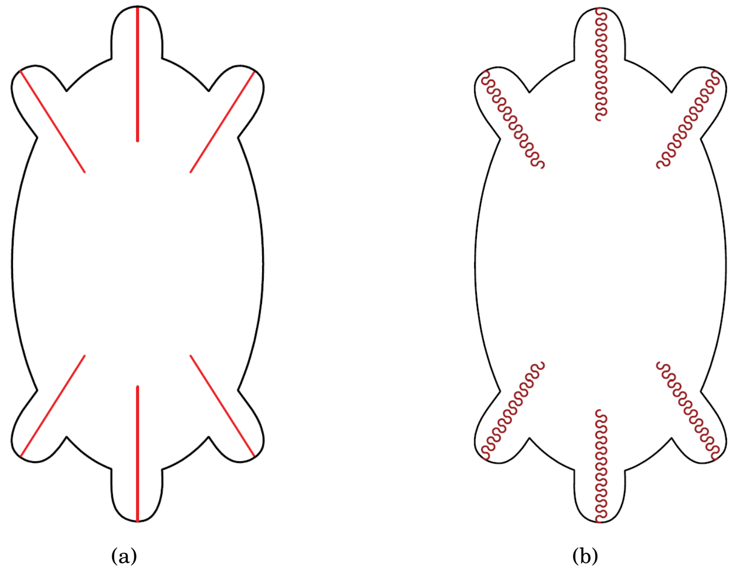

(a) (b)

Figure 3.14: The schematic representation of the *turtle* design. The interconnect tracks are represented by the red lines. (a) The arrangement of six straight interconnect lines; (b) The arrangement of six interconnects which are designed to assume the shape of horseshoe meanders. The figures are not drawn to scale.

The design of the interconnects themselves remained the same across the *oval* and the *turtle* membranes. Accordingly, the interconnects were designed as *short* and *long* with varying widths (10 μm and 30 μm) for both *straight* lines and the *meanders*. These different designs incorporated in the *turtle* membranes are shown in Figure 3.15.

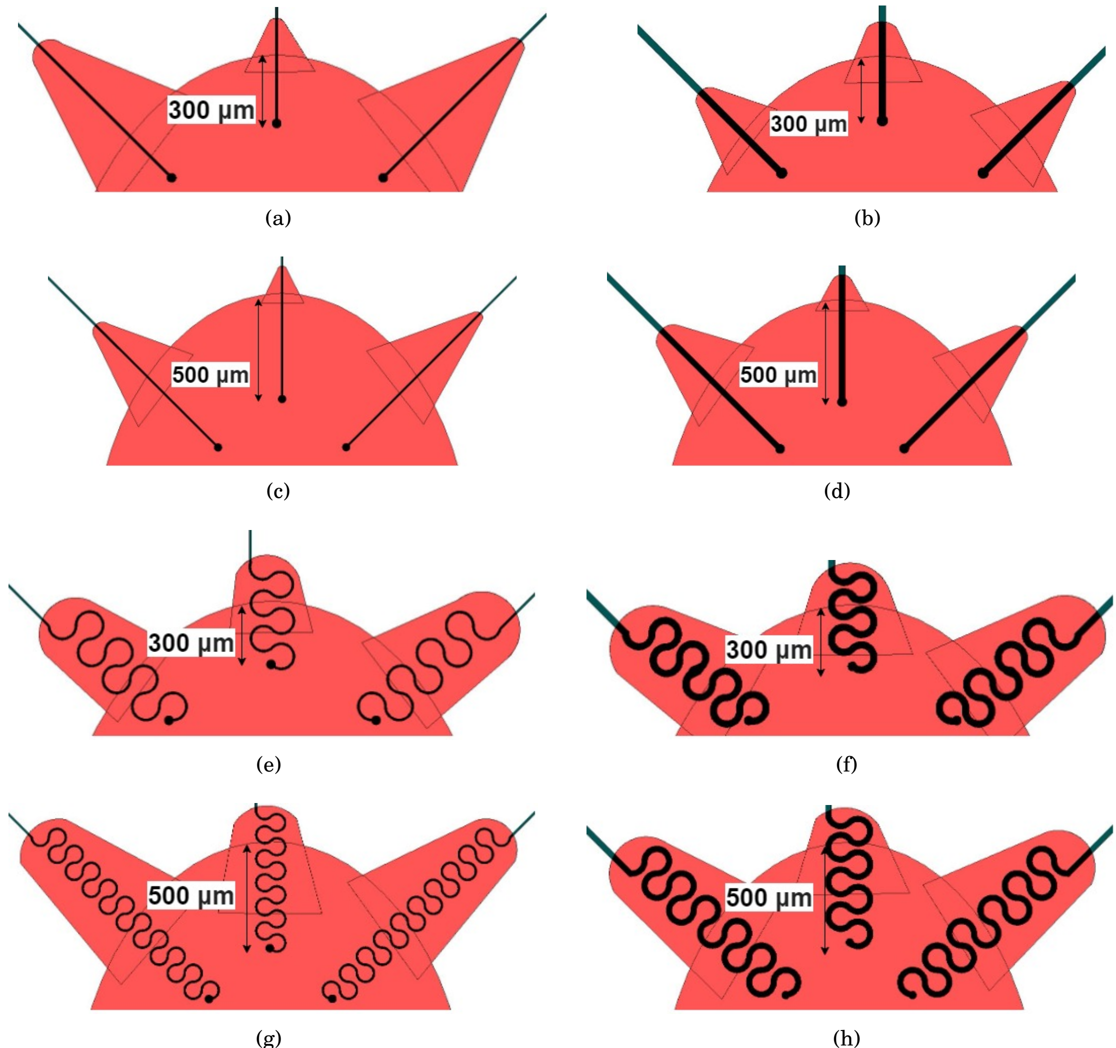

Figure 3.15: Different designs of the *straight* and *meander* interconnects in one half of the *turtle* membrane: (a) Shorter *straight* metal lines with a width of 10 μm; (b) Shorter *straight* metal lines with a width of 30 μm; (c) Longer *straight* metal lines with a width of 10 μm; (d) Longer *straight* metal lines with a width of 30 μm; (e) Shorter *meanders* with a width of 10 μm; (f) Shorter *meanders* with a width of 30 μm; (g) Longer *meanders* with a width of 10 μm; (h) Longer *meanders* with a width of 30 μm.

By introducing progressively tapered extensions in the geometry of the *oval* membrane, we were able to achieve regions of zero-second principal strain at the interface of the PDMS membrane and the silicon frame. These novel *turtle* designs are expected to improve the yield of the metal lines by making them less prone to cracks during the post-fabrication process, on account of adequately low regions of strain at the interface.

3.3 Summary of the Designs

In this chapter, the different designs adopted for the interconnect lines were presented. The optimum trajectories adopted for the interconnects were such that they were perpendicular to the direction of the first principal strain while simultaneously traversing along regions of least second principal strain. Three different designs for the membrane geometry were presented in Section 3.1 and 3.2, as illustrated in Figure 3.16. The *oval* design (3.16) does not offer regions of near-zero second principal strain at the interface. While, for the *turtle* designs, the tapering extensions introduced to the *oval* geometry resulted in regions of nearly zero second principal strain.

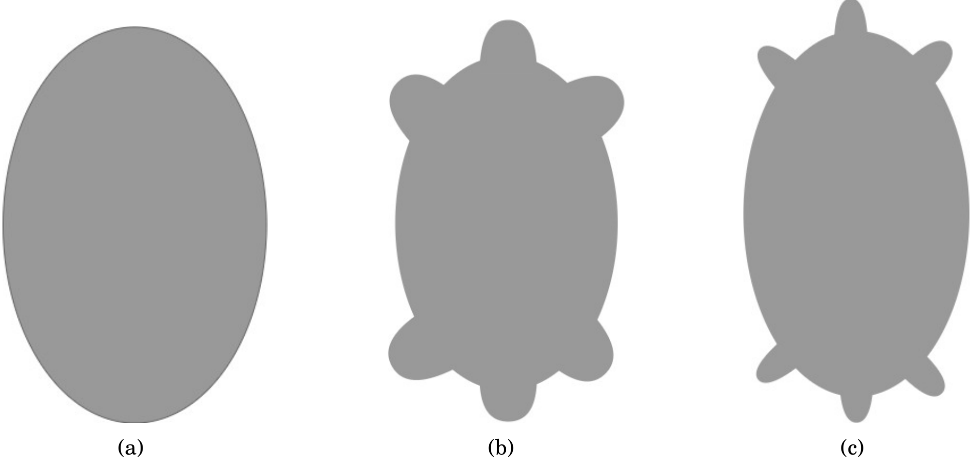

Figure 3.16: Mask designs of the membrane geometry adopted for the current Heart-On-Chip device. (a) The geometry of the *oval* membrane; (b) The geometry of the *turtle* membrane accommodating the meandering interconnects; (c) The design of the *turtle* membrane intended for the straight interconnects. The figures are not drawn to scale.

Apart from the geometry of the membrane area, several other design parameters were considered. An overview of the parameters taken into consideration are depicted in Figure 3.17. Based on the position of the electrode openings relative to the periphery of the membrane, the designs of the interconnects and metal lines can be classified as:

- Short interconnect lines- With the electrodes placed at positions that are 300 μm with respect to the membrane periphery.
- Long interconnect lines- With the electrode openings placed at positions that are 500 μm with respect to the membrane periphery.

On the basis of the shape adopted for the design of the interconnects, they can either be:

- Straight lines or,
- Horseshoe-shaped meanders.

Lastly, the effect of varying widths of the interconnects on its stress profile were taken into consideration while drafting different sets of designs:

- Interconnects with a smaller width of 10 μm.
- Interconnects with a larger width of 30 μm.

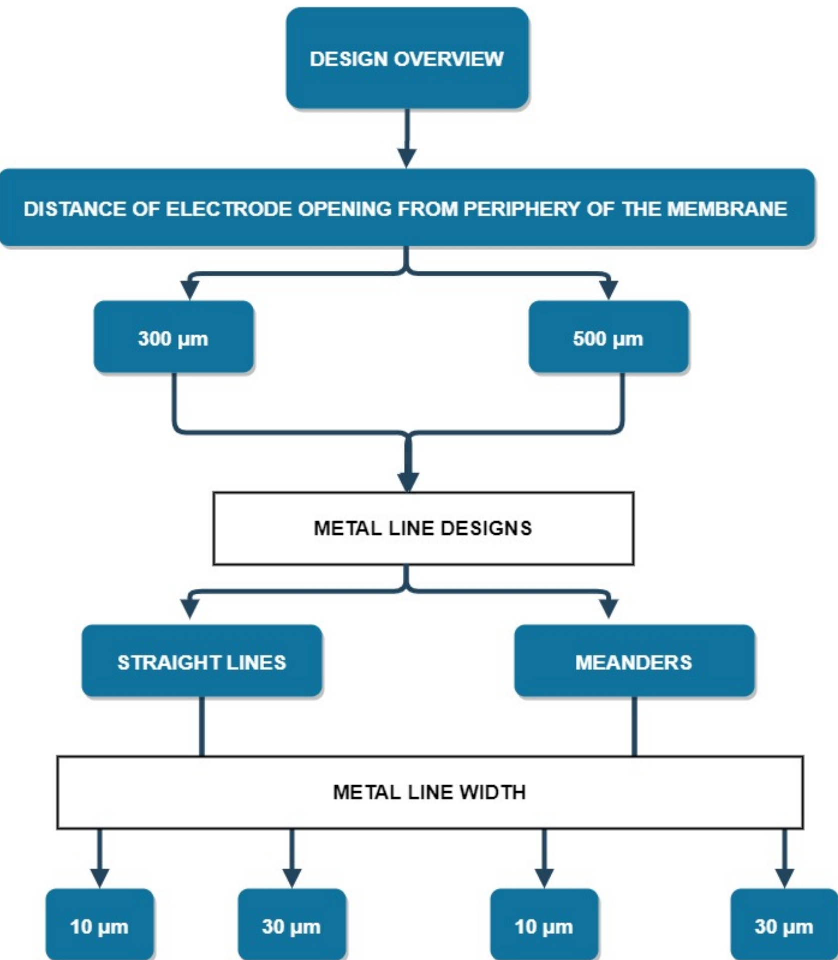

Figure 3.17: Summary of the different parameters based on which multiple designs for the metal interconnects were devised.

Simulations clearly show that the introduction of extensions in the *oval* membrane, provide regions of zero-second principal strain at the interface improving the yield during fabrication. As explained previously in Sections 3.1 and 3.2, interconnects with a smaller width that are integrated in the *turtle* membranes are expected to develop the least amount of stress during fabrication. Moreover, the horseshoe-shaped *meanders* are expected to redistribute the stress over a wider region, thereby preventing the accumulation of strain, ultimately resulting in cracks.

Table 3.1 provides information regarding the nomenclature adopted for the different sets of designs and their respective descriptions. The nomenclature assigned to each design was based on the position of the electrode openings, the shape of the interconnects, the width of the interconnect lines and the geometry of the membrane area. Essentially, the first letter of the nomenclature refers to the shape of the interconnects: **E** refers to the straight lines, while **M** refers to the meanders. The second letter is assigned based on the length of the interconnects spanning over the membrane area: **E** refers to the shorter lines that are closer to the membrane periphery, while **C** refers to the longer lines that are closer to the center of the membrane. The width of the interconnects are represented by the numbers in the nomenclature. The designs integrated on the *turtle* membrane have the term **Extend** appended at the end of the nomenclature. In the coming few sections, the different designs will be addressed according to the nomenclature that is assigned.

Table 3.1: Overview of the design nomenclature and their descriptions.

DESIGN NOMENCLATURE	DESCRIPTION
EE10	10 μm wide *straight* metal lines originating from a point that is at a distance of 300 μm from the periphery of the *oval* membrane.
EE30	30 μm wide *straight* metal lines originating from a point that is at a distance of 300 μm from the periphery of the *oval* membrane.
EC10	10 μm wide *straight* metal lines originating from a point that is at a distance of 500 μm from the periphery of the *oval* membrane.
EC30	30 μm wide *straight* metal lines originating from a point that is at a distance of 500 μm from the periphery of the *oval* membrane.
ME10	10 μm wide *meanders* originating from a point that is at a distance of 300 μm from the periphery of the *oval* membrane.
ME30	30 μm wide *meanders* originating from a point that is at a distance of 300 μm from the periphery of the *oval* membrane.
MC10	10 μm wide *meanders* originating from a point that is at a distance of 500 μm from the periphery of the *oval* membrane.
MC30	10 μm wide *meanders* originating from a point that is at a distance of 500 μm from the periphery of the *oval* membrane.
EE10_Extend	10 μm wide *straight* metal lines originating from a point that is at a distance of 300 μm from the periphery of the *turtle* membrane.
EE30_Extend	30 μm wide *straight* metal lines originating from a point that is at a distance of 300 μm from the periphery of the *turtle* membrane.
EC10_Extend	10 μm wide *straight* metal lines originating from a point that is at a distance of 500 μm from the periphery of the *turtle* membrane.
EC30_Extend	30 μm wide *straight* metal lines originating from a point that is at a distance of 500 μm from the periphery of the *turtle* membrane.
ME10_Extend	10 μm wide *meanders* originating from a point that is at a distance of 300 μm from the periphery of the *turtle* membrane.
ME30_Extend	30 μm wide *meanders* originating from a point that is at a distance of 300 μm from the periphery of the *turtle* membrane.
MC10_Extend	10 μm wide *meanders* originating from a point that is at a distance of 500 μm from the periphery of the *turtle* membrane.
MC30_Extend	10 μm wide *meanders* originating from a point that is at a distance of 500 μm from the periphery of the *turtle* membrane.

Table 3.2 represents all the different parameters taken into consideration while designing the interconnects for the *oval* and the *turtle* membranes. These, along with the nomenclature assigned to the different designs are depicted in Table 3.2, in the form of a matrix.

Table 3.2: Matrix depicting the different design parameters considered for the *oval* and the *turtle* membrane and their respective nomenclatures.

OVAL MEMBRANE			***TURTLE MEMBRANE***		
STRAIGHT LINES			**STRAIGHT LINES**		
	WIDTH			**WIDTH**	
LENGTH	10 μm	30 μm	**LENGTH**	10 μm	30 μm
LONG	EC10	EC30	LONG	EC10_Extend	EC30_ Extend
SHORT	EE10	EE30	SHORT	EE10_Extend	EE30_Extend
MEANDERS			**MEANDERS**		
	WIDTH			**WIDTH**	
LENGTH	10 μm	30 μm	**LENGTH**	10 μm	30 μm
LONG	MC10	MC30	LONG	MC10_Extend	MC30_Extend
SHORT	ME10	ME30	SHORT	ME10_Extend	ME30_Extend

4 | Fabrication Challenges Associated with Silicon Nitride Interconnects

This chapter focuses on the challenges associated with the processing of silicon nitride interconnects for the current Heart-On-Chip device. Previous studies have shown the formation of cracks in the metal lines during the fabrication process while utilizing parylene [23], or polyimide [24] as the insulating materials. Alternatively, we decided to study the feasibility of silicon nitride encapsulated interconnects in this device. As mentioned previously (Section 1.5), one of the goals of this thesis is to integrate a TiN MEA insulated by silicon nitride structures, that are embedded in a 200 μm thick PDMS layer. A 2D overview of the final device is illustrated in Figure 4.1. The "elastomer-last" fabrication strategy utilized during the development of the Cytostretch platform is adopted for the current device. Shifting to silicon nitride requires looking into different silicon nitride depositions to avoid etching away of the material while releasing the membrane. Preliminary studies were conducted to determine the etching rates of low pressure chemical vapor deposition (LPCVD) Si_3N_4 vs plasma-enhanced chemical vapor deposition (PECVD) SiN_x in HF and BHF solutions (Appendix A.2). Based on the data obtained, LPCVD nitride seems to be the optimal deposition technique owing to its slow etching rate in HF and BHF. Another critical point to consider, is the adhesion between the nitride structures and the PDMS membrane, to avoid the delamination of the interconnects (Section 4.1). The challenges encountered during the adhesion test and the alternate solutions are further elaborated on in Section 4.2.

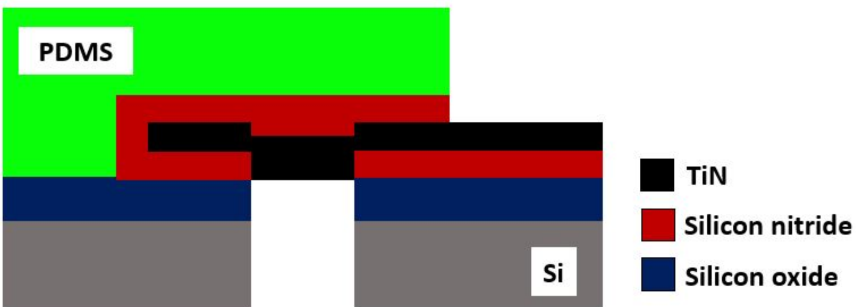

Figure 4.1: A 2D cross-sectional overview of the process flow to fabricate the current device. In this device, TiN electrodes that are insulated by silicon nitride structures are embedded in a thick PDMS membrane. The figure is not drawn to scale.

4.1 Adhesion Between Silicon Nitride and PDMS

The adhesion of silicon nitride (SiN_x) interconnects to the PDMS membrane is an important feature to consider while validating the viability of employing a ceramic material such as SiN_x for OOC applications. To investigate the adhesion between silicon nitride and PDMS, three samples were fabricated, which will be further referred to as the *control*, the *oxide-BEFORE* and the *oxide-AFTER* devices. The first insulating layer for the metal lines was fabricated from LPCVD Si_3N_4 due to its slow etch rate in HF and BHF solutions, as described in Appendix A.2 (Figure A.5).

The samples were fabricated on a 4" double side polished (DSP) n-type wafer of 525 μm thickness. The

overall fabrication sequence is as follows: 2 μm of PECVD tetraethyl orthosilicate (TEOS) and 4 μm of PECVD SiO_2 were deposited on the front and backside, respectively. The oxide on the backside was patterned to assume the shape of the membrane and acts as a hard mask later, as depicted in Figure 4.2 (a). A layer of 300 nm of LPCVD Si_3N_4 was then deposited on the front side and patterned as shown in Figure 4.2 (b), to form the first layer of the interconnects. This layer insulates the metal lines in the final device, but in order to simplify the fabrication process for the adhesion test, the metal interconnects and electrodes were not integrated in these test samples. A layer of 300 nm of PECVD SiN_x was deposited on top of the LPCVD silicon nitride layer to form the second insulating layer (Figure 4.2 (c)).

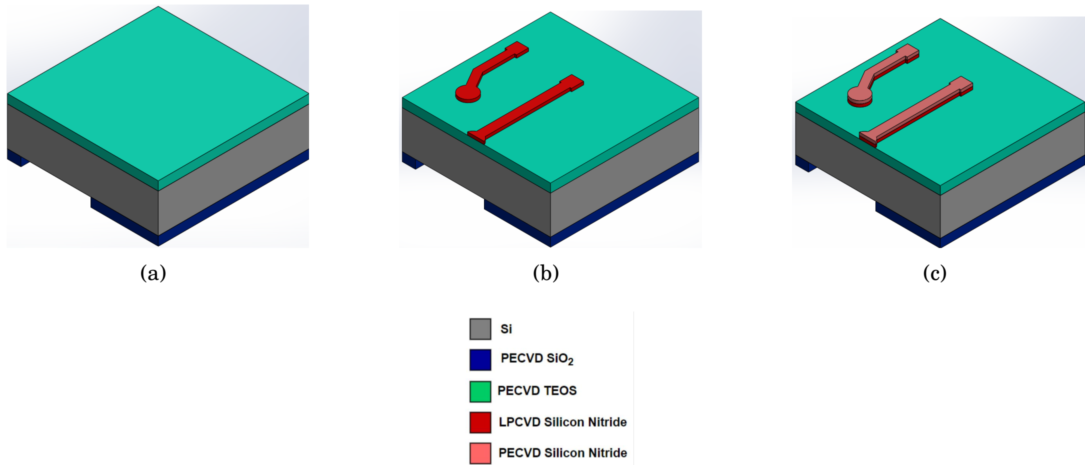

Figure 4.2: Fabrication flow of the test device for the adhesion test. (a) Deposition of the PECVD TEOS landing layer on the front and processing of the backside PECVD SiO_2; (b) Patterning of LPCVD silicon nitride insulating layer; (c) Deposition and patterning of the second insulating PECVD SiN_x layer. The figures are not drawn to scale.

In the *oxide-AFTER* samples, a thin layer of PECVD SiO_2 was deposited after processing the top PECVD SiN_x layer, as illustrated in Figure 4.3 (a). For the *oxide-BEFORE* samples, a 50 nm thin PECVD SiO_2 layer was deposited on the second nitride layer. The stack of PECVD SiN_x and silicon oxide layers were later processed together, as shown in Figure 4.3 (b). In the *control* set, there was no oxide on top of the nitride stack. This was performed to assess whether the thin oxide layer helps in the adhesion of the nitride layer to PDMS. A 200 μm thick PDMS layer was spin coated on the front side of the wafer and cured at 90°C for one hour, to form the stretchable membrane. After the PDMS membrane was cured, the SiN_x layers were covered by the membrane, as shown in Figure 4.4 (a) for the *control* set, Figure 4.4 (d) for the *oxide-AFTER* devices, and Figure 4.4 (g) for the *oxide-BEFORE* samples.

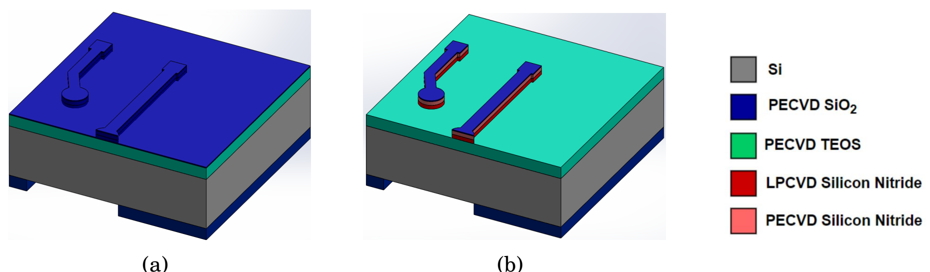

Figure 4.3: (a) *oxide-AFTER* device, with a thin PECVD SiO_2 layer deposited on top of the patterned nitride stack; (b) *oxide-BEFORE* sample, where the thin oxide layer is patterned lithographically along with the stack of nitride layers. The figures are not drawn to scale.

The final steps of the fabrication involves releasing the PDMS membrane via Deep Reactive Ion Etching (DRIE) process, wherein the silicon substrate was etched through from the backside of the wafer. The 4 μm SiO_2 on the backside of the wafer functions as a hard mask during the DRIE process, while the 2 μm TEOS on the front serves the purpose of a landing layer, to protect the structures on the PDMS

membrane. Once the silicon substrate was etched, the 2 μm TEOS was wet etched to expose the nitride layers secured on the PDMS membrane, as shown in Figures 4.4 (e-h). Through these open areas, these test devices were immersed in various solvents to test the adhesion between SiN_x and the PDMS layer.

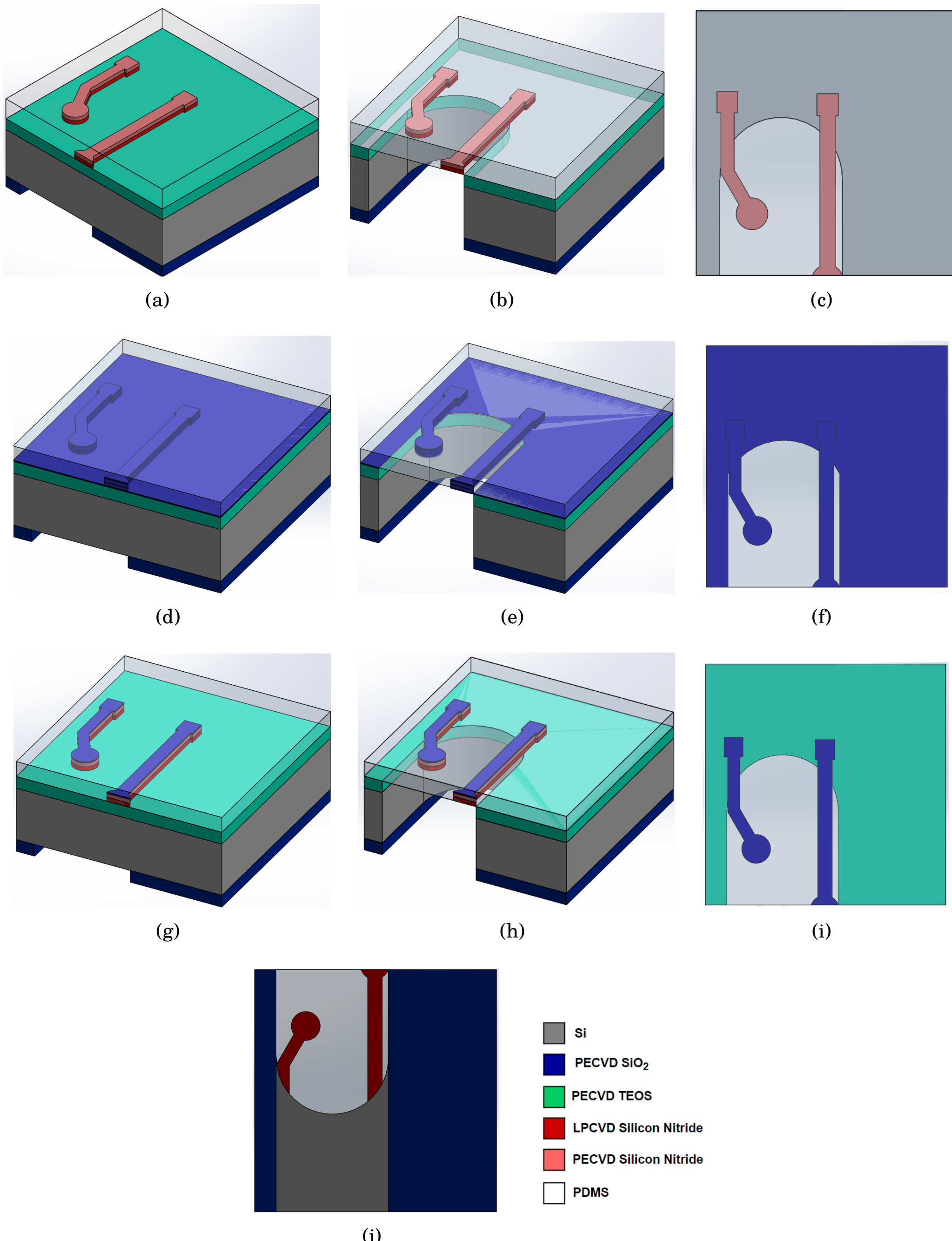

Figure 4.4: Process flow of the *control* set: (a) Curing of PDMS; (b) Membrane releasing; (c) Top view of the *control* samples, after releasing of the membrane. Process flow of the *oxide-AFTER* devices: (d) PDMS coating; (e) Membrane releasing; (f) Top view, illustrating the deposition of the oxide layer over the entire surface of the sample. Process flow of the *oxide-BEFORE* samples: (g) Coating with PDMS; (h) Membrane releasing; (i) Top view of the *oxide-BEFORE* samples, which shows the processing of the oxide layer along with the nitride stack; (j) Bottom view of the devices after releasing the membrane. The figures are not drawn to scale.

With this experiment, it was expected to observe the detachment of the PECVD SiN_x layer from the PDMS membrane. Accordingly, microscopic images of the samples were taken before and after the immersion in different solvents. Also, the samples were observed with SEM after its exposure to the

different solvents. The experiment was carried out as follows:

1. Imaging under a microscope **before** immersion of the samples in the solvents.
2. Immersion of samples from the three sets (*control*, *oxide-AFTER* and *oxide-BEFORE*) in the following solvents for 5 minutes:
   - Acetone, at room temperature (RT)
   - Acetone, at 40°C
   - Ethanol, at room temperature (RT)
   - Ethanol, at 70°C
   - Ultrasonic bath (USB): Acetone, at 40°C
   - Ultrasonic bath (USB): Ethanol, at 70°C

   **To ensure that the solvent was in direct contact with the nitride layer and the PDMS membrane, the samples were placed with the backside of the wafer facing up.*
3. Samples were rinsed in DI water for 5 minutes to wash away any remaining solvent from the samples.
4. Samples were imaged under a microscope to observe the adhesion between the nitride and the PDMS layers after the immersion test.
5. Steps (1-4) were repeated for the samples which did not exhibit any delamination of the nitride layers. These samples were immersed in the above mentioned solvents in increments of 5 minutes for each run.
6. Samples which exhibited delamination after immersion in a solvent for 5 minutes were not utilized for further testing.
7. Additionally, the *oxide-BEFORE* devices were placed in an ultrasonic bath (USB), with acetone and ethanol, for up to 20 minutes to validate the adhesion.

Figure 4.5 depicts the SEM images of the three samples after completion of the immersion test in an ultrasonic bath (USB) bath containing acetone at 40°C. The nitride layers were peeled off from the polymeric membrane from the samples with no additional oxide layer, when they were immersed in acetone at 40°C in an USB. This is represented in Figure 4.5 (a-c). Similar results were observed for the *oxide-AFTER* samples, as illustrated in Figure 4.5 (d-f). It is clearly evident that the *oxide-BEFORE* samples display improved adhesion between the SiN_x layer and the PDMS membrane, even when they were immersed in acetone at 40°C in an ultrasonic bath. Similar patterns were observed for the samples when they were immersed in the above mentioned solvents (Table 4.1).

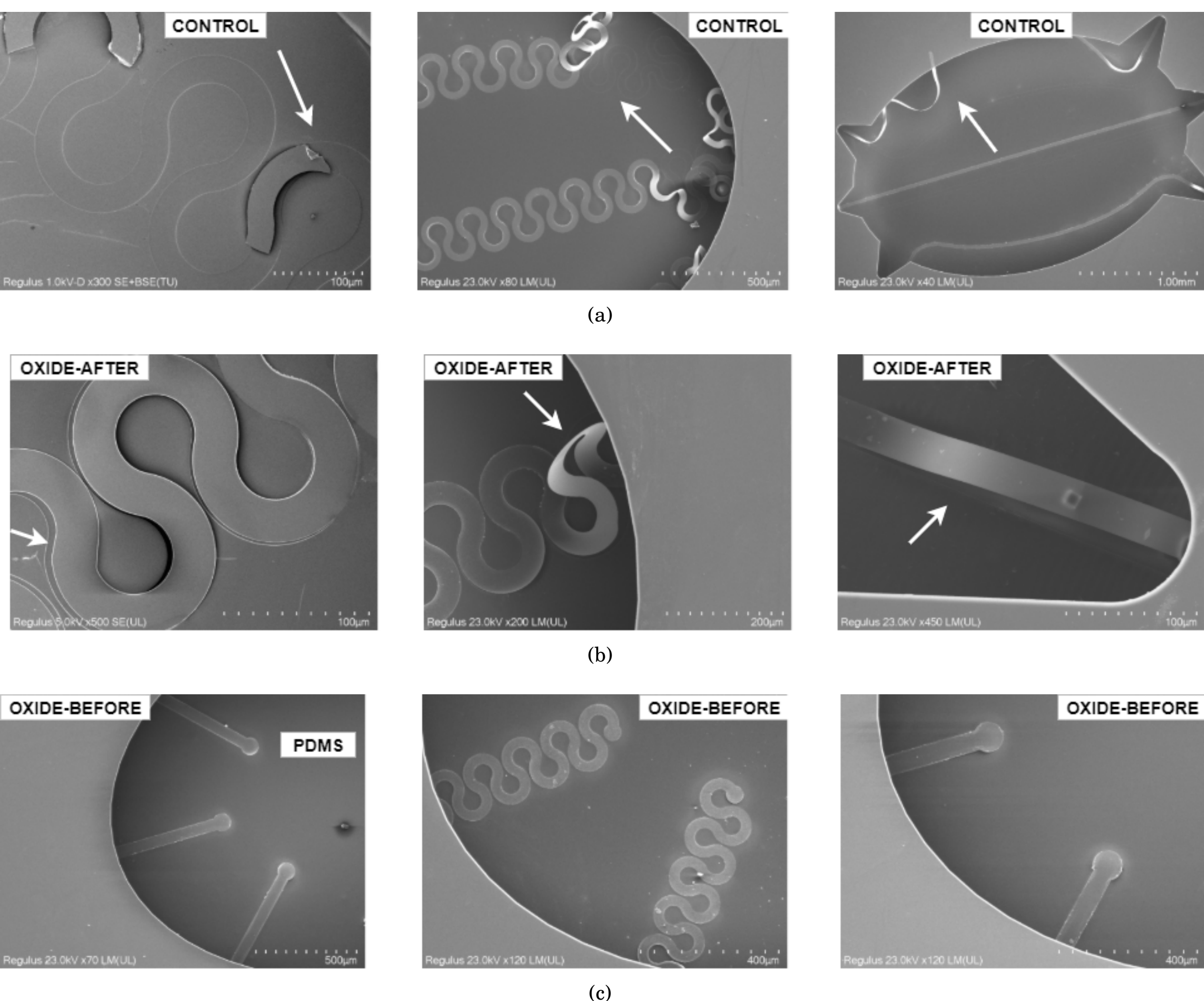

Figure 4.5: (a) Delamination of the silicon nitride layer from the PDMS membrane when immersed in an USB with acetone at 40°C, as seen in the *control* set; (d), (e) and (f) Delamination of the nitride layers, as observed in the *oxide-AFTER* devices; (g), (h) and (i) The effect of the additional oxide layer in the *oxide-BEFORE* samples which do not exhibit any delamination of the SiN_x layer after being exposed to the same solvent for a period of 20 minutes.

The results of the immersion test in various solvents are tabulated in Table 4.1. It is evident that in the *oxide-BEFORE* devices, the thin oxide layer significantly improved the adhesion of the silicon nitride stack to the PDMS membrane, even when they were exposed to the solvents in an ultrasonic bath for 20 minutes. Both the *control* set (with no additional oxide layer) and the *oxide-AFTER* devices show poor adhesion between the SiN_x layer and the polymer membrane. In Table 4.1, delamination of the nitride structures are represented by the red cells marked with 'x'. In these samples, delamination was observed in more than 60% of the devices. while, the samples with good adhesion are represented by the green cells marked with 'o'. In these samples, the nitride structures display good adhesion in at least 52 devices.

Table 4.1: Results of the adhesion test of the test samples in different solvents.

	Control set				Oxide-BEFORE				Oxide-AFTER			
	5 min	10 min	15 min	1x20 min	5 min	10 min	15 min	1x20 min	5 min	10 min	15 min	1x20 min
SOLVENTS												
Acetone RT	o	o	o	-	o	o	o	-	o	o	o	-
Acetone 40°C	o	o	o	-	o	o	o	-	o	o	o	-
Ethanol RT	x	x	x	-	o	o	o	-	o	o	o	-
Ethanol 70°C	x	o	-	-	o	o	o	-	o	o	o	-
Ultrasonic bath: Acetone 40°C	x	x	-	-	o	o	o	o	x	-	-	-
Ultrasonic bath: Ethanol 70°C	x	x	-	-	o	o	o	o	x	-	-	-

'o' = No delamination in at least 50 devices
'x' = Delamination in more than 60% of the devices
'-' = Adhesion test not performed.
5,10,15 min = Sample immersed in a solvent for a total of 15 minutes, in increments of 5 minutes each.
1x20 min = Immersion of sample in the solvent for 20 minutes continuously.

The SiO_2 landing layer is wet etched in 5% HF (Figure 4.4 (b, e, h)) to release the PDMS membrane. In the *oxide-AFTER* samples during wet etching, the thin oxide layer covering the sidewalls of the nitride structures (**SIDE-SiO₂**) are etched away by the HF molecules (Figure 4.6 (a)). This provides a path for the small HF molecules to also etch the (**TOP-SiO₂**) layer, which results in the poor adhesion between the SiN_x and PDMS layers for the *oxide-AFTER* samples. In contrast, in the *oxide-BEFORE* samples (Figure 4.6 (b)), the **TOP-SiO₂** adhesion layer remains intact while releasing the membrane, thereby ensuring good adhesion. Based on these results, patterning of an additional thin oxide layer together with the PECVD SiN_x layer in the final device is imperative to ensure good adhesion.

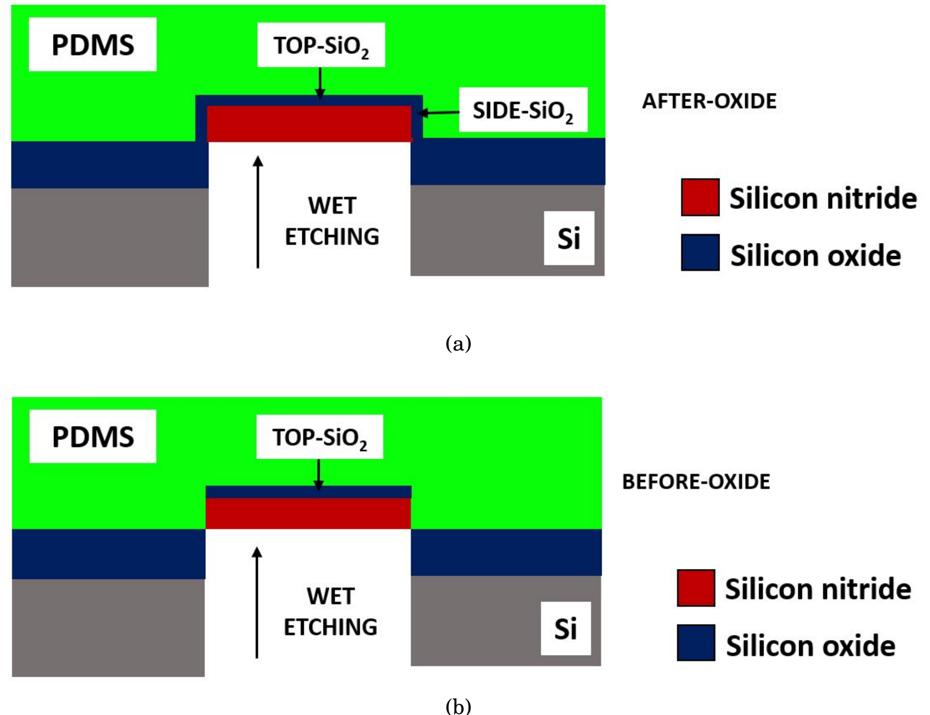

Figure 4.6: a 2D sketch of the (a) *oxide-AFTER* and, (b) the *oxide-BEFORE* samples.

4.2 Stress Analysis

While inspecting the adhesion between SiN_x layer and the PDMS membrane, it was observed that the PDMS layer displayed surface buckling, or *wrinkles*, as illustrated in Figure 4.7. Topological cues have been shown to influence the alignment of cells and the formation of the extracellular matrix (ECM) architecture [94]. The presence of *wrinkles* in the PDMS membrane may also result in the formation of cracks in the electrodes. Moreover, the *wrinkles* also make it difficult to optically image the structures embedded in the thick PDMS layer. Therefore, it is necessary to investigate the origin of *wrinkles* to avoid the above mentioned issues. To reiterate, the process flow for the fabrication of the test devices for the adhesion test is illustrated in Figure 4.2, Figure 4.3 and Figure 4.4. As previously described, a layer of LPCVD Si_3N_4 served as the first insulating layer for the metal lines, while the second insulation layer was provided by a thin film of PECVD SiN_x. LPCVD depositions are generally carried out at high temperatures (~800-900°C) in comparison to PECVD depositions (~300-400°C) [95]. It was hypothesized that the high temperature deposition of LPCVD Si_3N_4 results in increased residual stress, which consequently leads to the buckling of the soft PDMS membrane. The phenomenon of surface buckling occurs when compressive forces are applied to a thin, rigid layer that is bound by a soft membrane, such as PDMS [96, 97, 98]. In order to investigate the origin of *wrinkles* in the PDMS layer, two samples were fabricated. These test samples were aimed to explore the:

1. Effect of the novel membrane designs on the development of stress across the PDMS layer (Section 4.2.1).
2. Effect of the deposition technique of the silicon nitride layer- PECVD vs LPCVD- on the formation of *wrinkles* (Section 4.2.2).

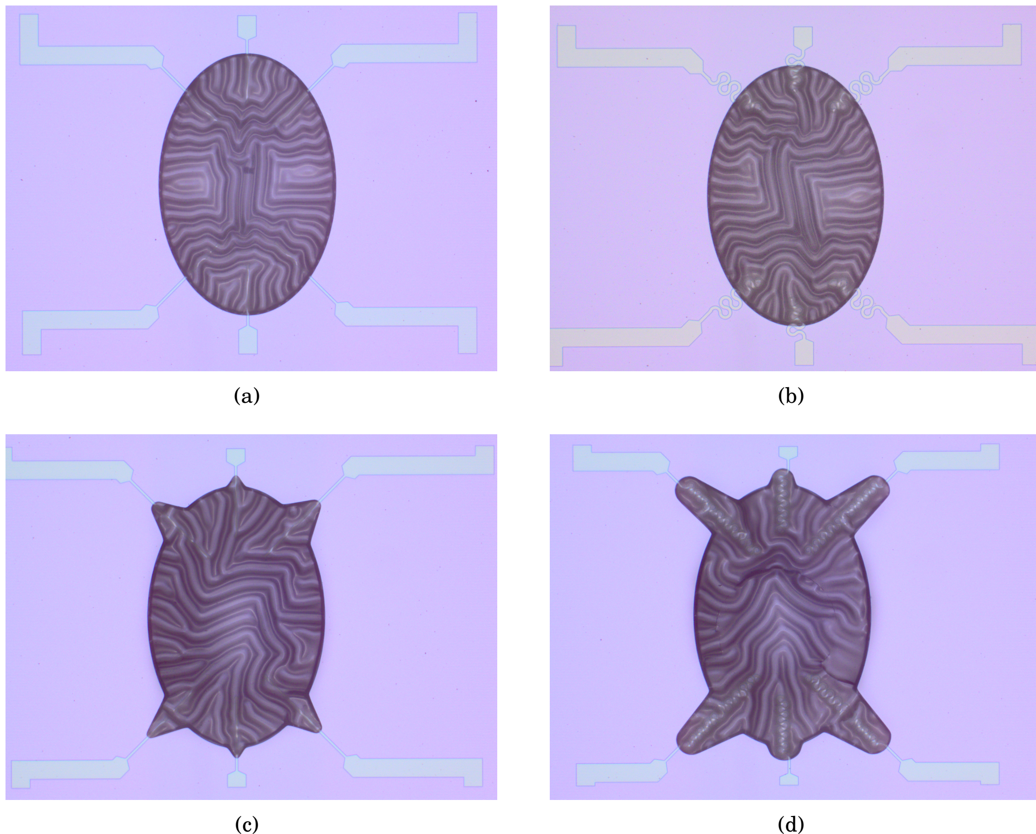

(a) (b) (c) (d)

Figure 4.7: The occurrence of wrinkles on the PDMS membrane as observed under a microscope during the adhesion test, for different designs: (a) EC10; (b) ME30; (c) EC10_Extend; (d) MC10_Extend.

4.2.1 Effect of the Novel Membrane Designs

To ensure that the novel membrane designs formulated for the current device (Section 3.3, Figure 3.16) do not contribute to the development of stress across the PDMS membrane, test samples were fabricated with *no structures* embedded in the polymer. The overall fabrication sequence is as follows: 2 μm and 4 μm of PECVD SiO_2 was deposited on the front and backside of a DSP wafer, respectively. The oxide on the backside was patterned to assume the geometry of the membrane, as shown in Figure 4.8 (a). A thick layer of 200 μm PDMS was spin coated on the front side of the wafer and was subsequently cured at 90°C for 60 minutes to form the membrane layer, as depicted in Figure 4.8 (b). By utilizing the SiO_2 on the backside of the wafer as a hard mask, the silicon substrate was etched through to land on the front side oxide. Finally, the membrane was released by wet etching the oxide etch stop layer to expose the PDMS membrane (Figure 4.8 (c)).

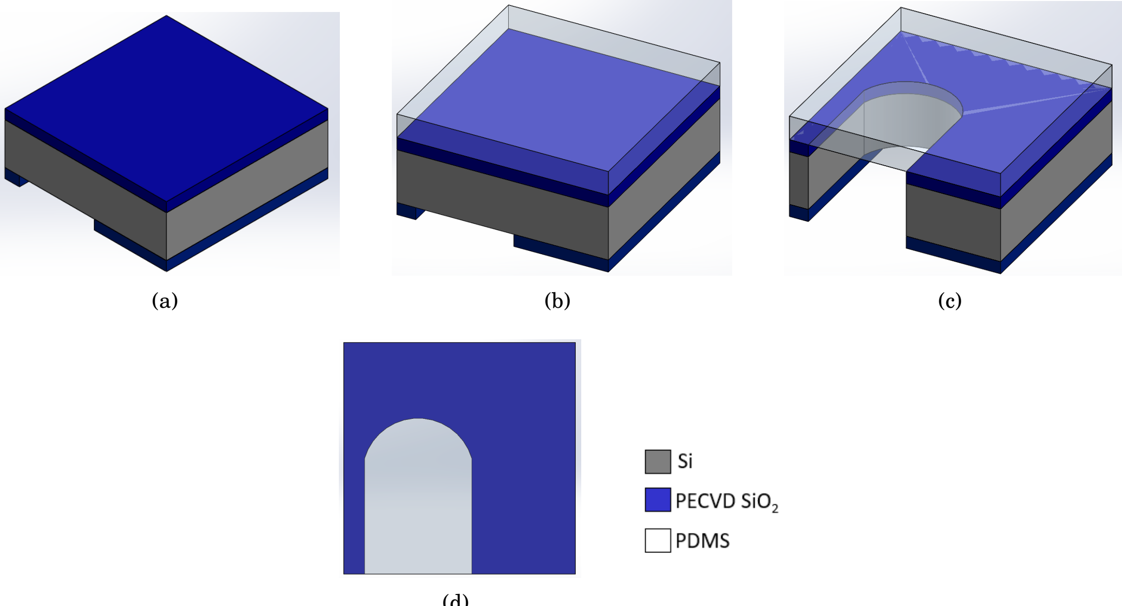

Figure 4.8: Process flow for the fabrication of test devices to investigate the effect of the membrane design on the stress profile of the PDMS membrane: (a) Processing of the backside and front side PECVD SiO_2; (b) PDMS coating; (c) Through-silicon etching and membrane releasing; (d) Bottom view of the final test sample. The figures are not drawn to scale.

After releasing the membrane, the samples were observed under the microscope. The results of the experiment are depicted in Figure 4.9. Based on these results, it was concluded that the novel membrane designs developed in this project were not responsible for the formation of *wrinkles* in the PDMS membrane.

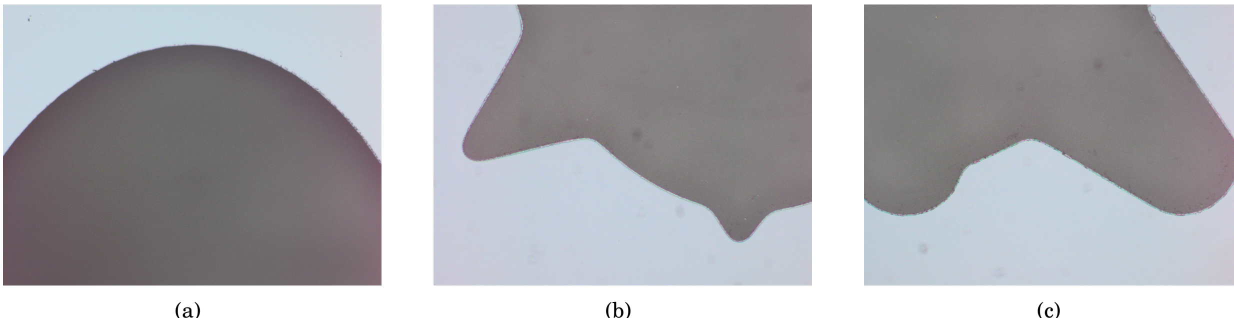

(a) (b) (c)

Figure 4.9: Microscope images of the PDMS membrane as observed in the samples fabricated for evaluating the effect of the membrane design on the formation of *wrinkles* in different designs, such as the: (a) Oval membrane; (b) Turtle membrane, for the straight metal lines; (c) Turtle membrane, to accommodate the meanders.

4.2.2 Effect of the Deposition Technique of Silicon Nitride

Based on the information obtained from the previous experiment (described in Section 4.2.1), it was apparent that the novel designs developed for the membrane do not contribute to the formation of *wrinkles*. Following this, it was necessary to study the effect of the deposition technique employed for silicon nitride, by fabricating samples with PECVD SiN_x structures embedded in the PDMS layer. This was contrary to the LPCVD Si_3N_4 insulation layer employed for the adhesion test (Section 4.1). The process flow for the samples utilized for this experiment is as follows: 2 μm and 4 μm of PECVD SiO_2 was deposited on the front and back of a wafer, respectively. The oxide on the backside of the wafer was dry etched to form the membrane area (Figure 4.10 (a)). A stack of 700 nm of PECVD SiNx and a thin 50 nm PECVD SiO_2 were processed to form the second layer of interconnects (Figure 4.10 (b)). A thick 200 μ PDMS layer was spin-coated on top of the SiN_x and was cured at 90°C for 60 minutes (Figure 4.10 (c)). The silicon substrate on the backside was etched through via DRIE process using the oxide on the back as a hard mask. Subsequently, the membrane was released by wet etching the SiO_2 on the front, to expose the PECVD SiN_x structures that were embedded in the PDMS membrane, as depicted in Figure 4.10 (d-e).

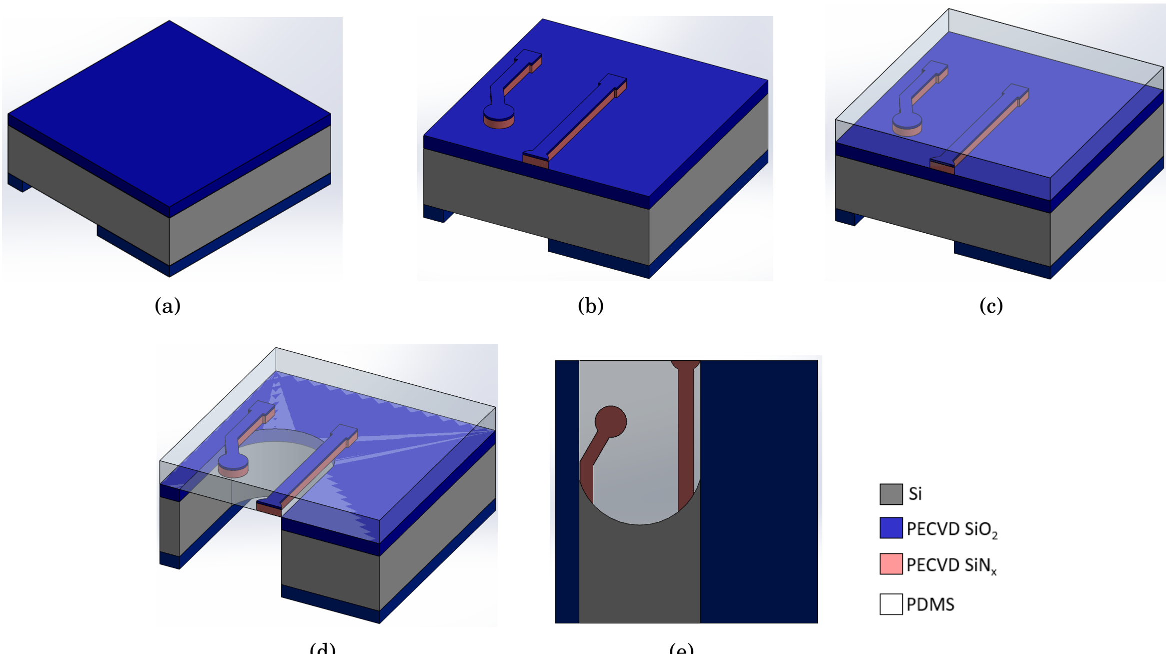

Figure 4.10: Fabrication flow for the samples utilized to analyze the effect of PECVD SiN_x structures on the formation of *wrinkles* when the PDMS membrane is released via DRIE process: (a) Processing of PECVD SiO_2 on the backside and front side of a DSP wafer; (b) Patterning of a stack of PECVD SiN_x and an oxide adhesion layer; (c) PDMS coating; (d) Membrane releasing; (e) Bottom view of the final sample, which displays the PECVD SiN_x insulation structures embedded in the PDMS membrane. The figures are not drawn to scale.

The samples were observed and imaged under a microscope after releasing the PDMS membrane. The images of the PDMS membrane with the PECVD SiN_x structures for different designs are shown in Figure 4.11. These samples displayed no *winkles* on the PDMS layer. It was apparent that the high temperature LPCVD deposition of Si_3N_4 caused the soft PDMS membrane to buckle (Figure 4.7). Alternatively, the PECVD SiN_x structures that were processed at much lower temperatures did not lead to the formation of *wrinkles*.

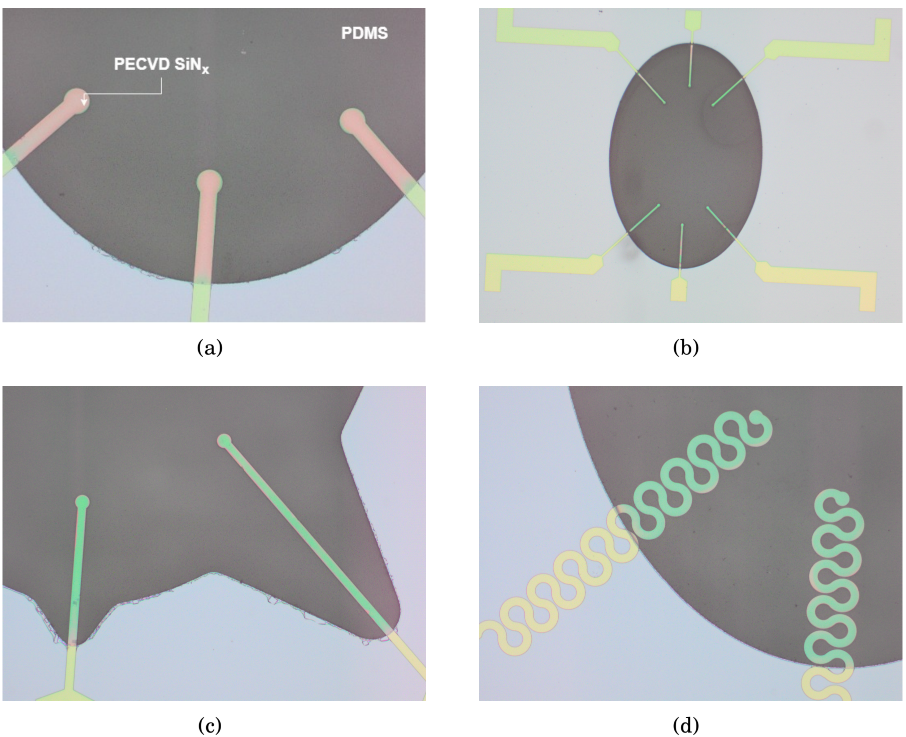

Figure 4.11: Microscope images of the test samples with PECVD SiN_x structures embedded in the PDMS membrane on a DSP wafer after releasing the membrane, as observed for different designs such as: (a) EE30; (b) EC10; (c) EE10_Extend; (d) MC30.

Based on the results of this experiment, it was concluded that the thermal mismatch due to the high-temperature LPCVD Si_3N_4 deposition, resulted in the formation of *wrinkles* in the PDMS membrane (Figure 4.7). As mentioned previously, these *wrinkles* may cause the metal lines (in the final device) to crack during the fabrication process, and can also influence the behaviour of cells when they are seeded on the PDMS substrate [94]. Therefore, we decided to process both the insulation layers as PECVD SiN_x for the final device as an alternate solution (Section 5.1).

5 | Fabrication and Characterization of the Device

Taking into consideration the novel designs presented in Chapter 3 and the fabrication challenges associated with SiN_x interconnects (addressed in Chapter 4), a fabrication protocol for the final devices was defined in this chapter. Section 5.1 provides the details of the process flow to integrate the TiN MEA encapsulated by PECVD SiN_x layers in a Heart-On-Chip device. Furthermore, the formation of cracks in TiN metal lines was investigated for all the different designs of the interconnects for the *oval* and the *turtle* membranes (Section 5.2). In this manner, the yield obtained for different designs was assessed during the fabrication and post-fabrication process. Finally, electrochemical impedance spectroscopy (EIS) measurements were carried out to prove the functionality of the TiN electrodes.

5.1 Fabrication of the Final Device

During the fabrication of the test samples for the adhesion test (Section 4.2), *wrinkles* were observed on the PDMS membrane (Figure 4.7). Further investigation proved the role of the LPCVD Si_3N_4 deposition on the formation of *wrinkles*. Accordingly, PECVD SiN_x was used as an alternative for the isolation layers, to avoid the occurrence of *wrinkles*. Since PECVD SiN_x is etched faster in HF and BHF solutions (Appendix A.2), we decided to increase the thickness of the nitride isolation structures to compensate for the higher etch rate. Based on the above mentioned optimization approaches, a revised wafer-scale process flow was developed for the current device (Figure 5.1).

The devices were fabricated on a 4" double side polished (DSP) n-type wafer of 525 μm thickness. The overall fabrication sequence is as follows: A 2 μm thick and a 4 μm thick layer of PECVD SiO_2 was deposited on the front side and backside (5.1 (a)). The oxide on the backside was patterned to define the membrane area. This layer of oxide behaves as a hard mask during the later stages of processing. PECVD SiN_x of 400 nm thickness was patterned on the front side, to form the first isolation layer. The electrode openings were defined in the first nitride layer (Figure 5.1 (b)). A layer of titanium nitride (TiN) with a thickness of 300 nm was sputtered at 350°C on the first isolation layer of PECVD nitride. Unlike previous works [23, 24], we were able to achieve a lower resistivity value for the TiN by sputtering at higher temperatures (Appendix A.3). The TiN was then patterned and dry etched to form the electrodes, metal lines and the bond pads (Figure 5.1 (c-d)). A layer of PECVD SiN_x of 300 nm thickness and a thin adhesion layer of PECVD SiO_2 was patterned to form the second isolation layer (Figure 5.1 (e)). Subsequently, a 200 μm thick layer of PDMS was spin coated on the front side of the wafer and cured at 90°C for 60 minutes (Figure 5.1 (f)). The silicon substrate was etched through from the backside using the DRIE process by utilizing the PECVD SiO_2 on the backside as a hard mask. The oxide on the front serves as a landing layer during the DRIE process and was subsequently wet etched to release the PDMS membrane (Figure 5.1 (g-h)). This enables the electrode openings to be accessed from the back. The TiN bond pads on the front side of the wafer were opened by manually removing the PDMS layer covering them (Figure 5.1 (i-j)).

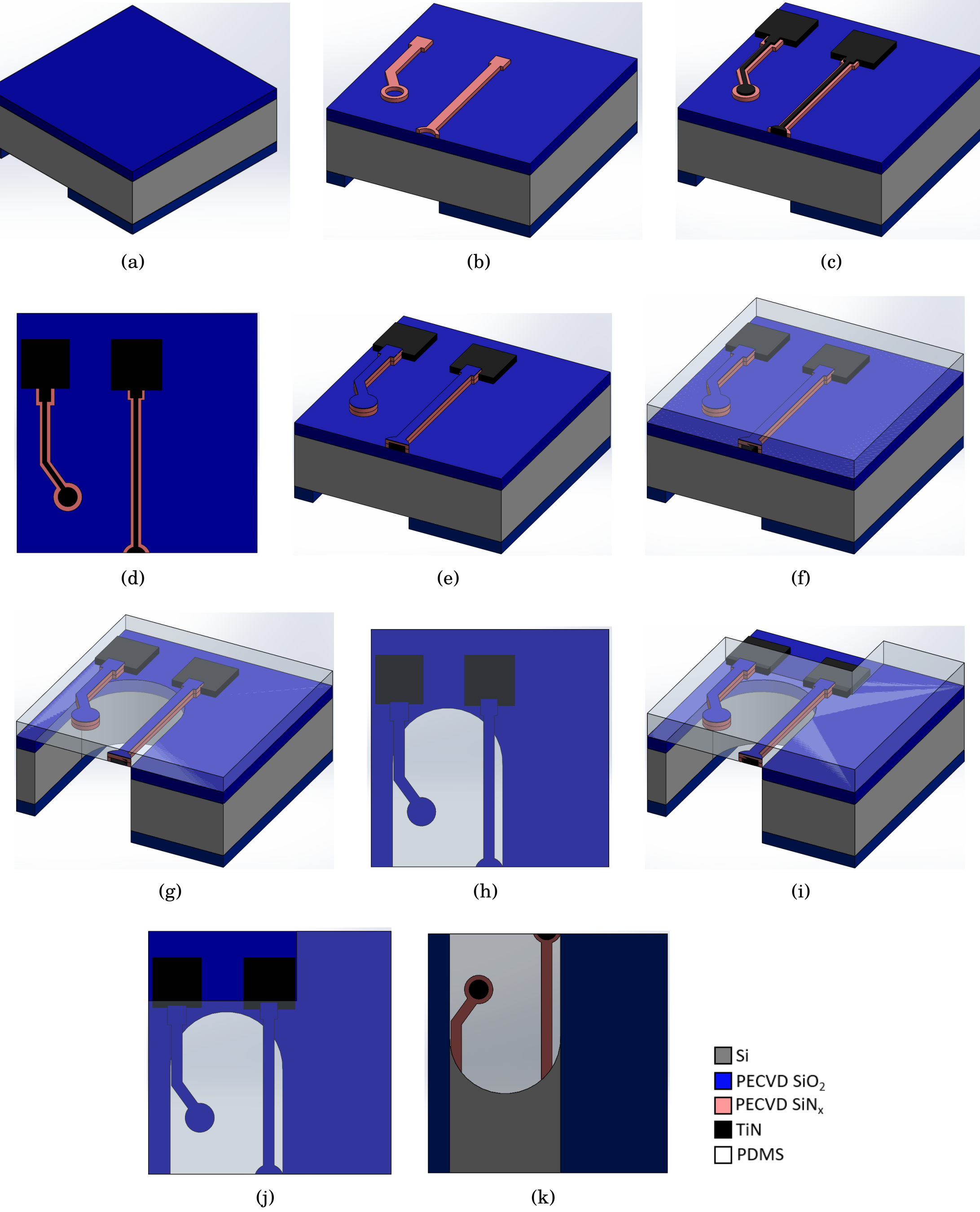

Figure 5.1: Process flow for the fabrication of the final device: (a) Deposition of the PECVD SiO_2 landing layer on the front and the patterning of the PECVD SiO_2 on the back; (b) Patterning of the electrode openings and the first isolation layer defined by PECVD SiN_x; (c) Patterning of TiN to form the electrodes and the bond pads, and its (d) Top view; (e) Deposition, patterning and dry etching of the second PECVD SiN_x isolation layer along with the thin oxide adhesion layer; (f) PDMS coating; (g) Membrane releasing, and its (h) Top view; (i) Opening of the bond pads, and its (j) Top view; (k) Bottom view of the device depicting the electrode openings embedded in the PDMS membrane. The figures are not drawn to scale.

As previously described in Sections 3.1 and 3.2, different designs were formulated for the interconnects: short and long lines, with varying widths (10 μm and 30 μm) for both *straight* lines and *meanders*. These designs were integrated in both the *oval* and the *turtle* membranes. A schematic overview of the design of the *straight* and *meanders-shaped* metal lines adopted for the current Heart-On-Chip device is depicted in Figure 5.2. The design of the first isolation layer of silicon nitride with the electrode openings are shown in Figure 5.2 (a-b). Commercial MEAs employ TiN electrodes of 30 μm diameter [58]. Hence, we

designed micro-electrodes with a diameter of 30 μm for the *inCHIPit*^{TM} device. Figure 5.2 (c-d) depicts the design of the TiN *straight* and *meander* lines. The designs of the second layer of silicon nitride which insulates the metal structures are shown in Figure 5.2 (e-f).

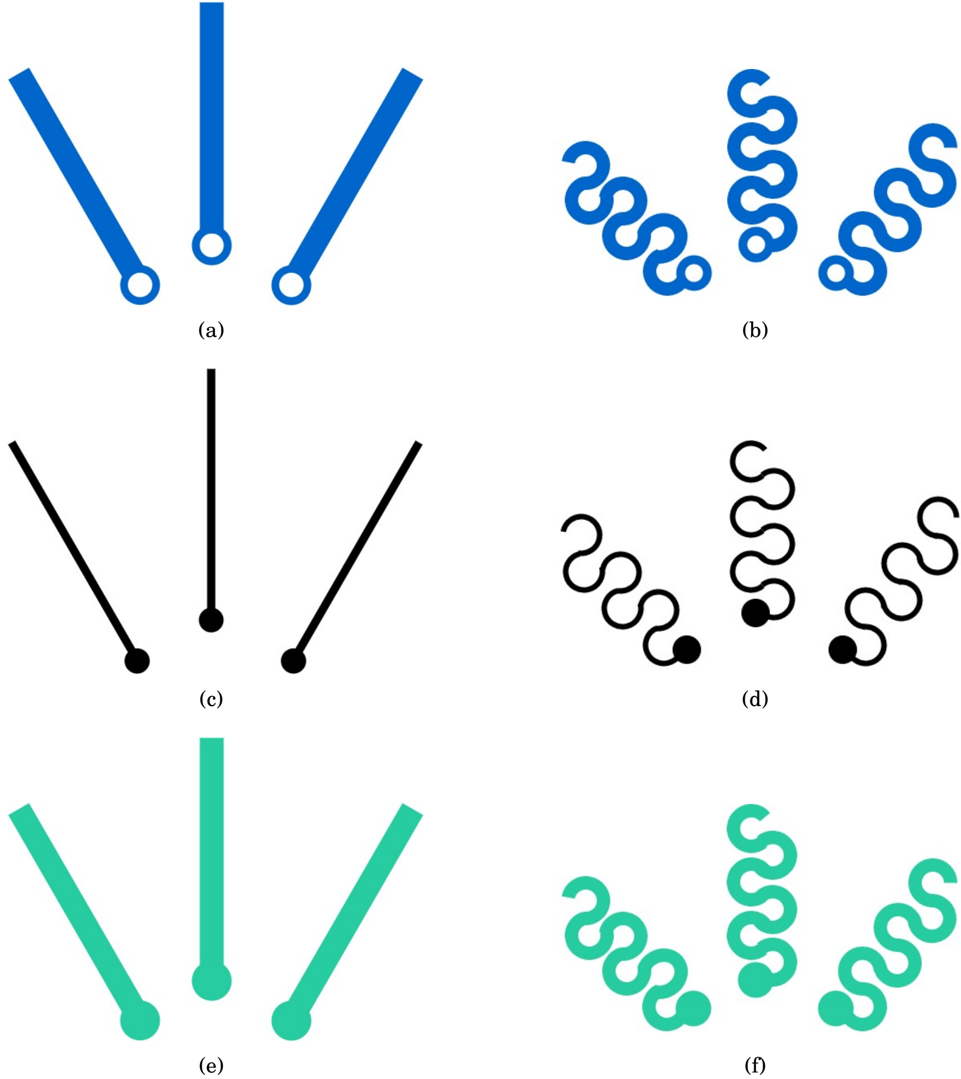

Figure 5.2: Mask designs adopted for the current Heart-On-Chip device illustrated for one half of the membrane. (a) Design of the first layer of silicon nitride *straight* lines insulating the metal lines, with an opening of 30 μm for the TiN electrodes; (b) Design of the horseshoe-shaped *meanders* of the first layer of silicon nitride with the 30 μm electrode openings; (c) Design of the *straight* metal lines and electrodes; (d) Design of the horseshoe-shaped *meanders* for the metal lines; (e) Design of the second insulating layer of silicon nitride (*straight* lines); (f) The second layer of silicon nitride (*meanders*). The figures are not drawn to scale.

The following figures display the SEM images of the current Heart-On-Chip device at different stages of fabrication. Figure 5.3 shows the SEM images of the first isolating layer of PECVD SiN_x patterned on a layer of PECVD SiO_2, with 30 μm wide electrode openings. This process of fabrication is shown in Figure 5.1 (b).

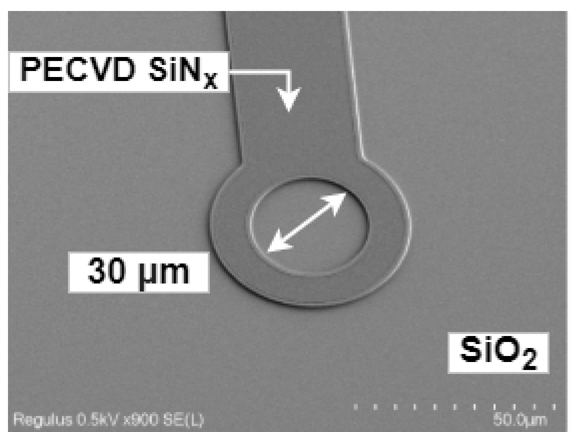

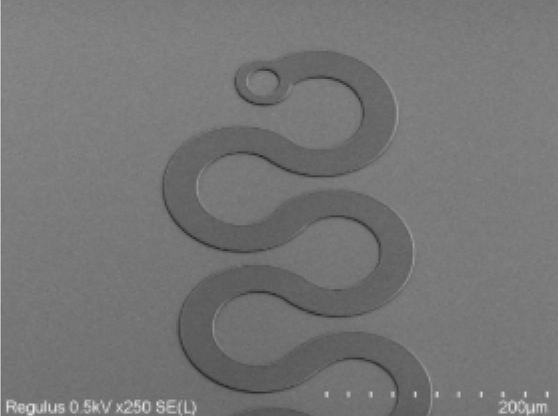

Figure 5.3: SEM images of the first layer of PECVD SiN_x isolation structures (*straight* lines and the *meanders*), with the 30 μm electrode openings.

TiN was sputtered and patterned on the first layer of PECVD SiN_x to form the 30 μm diameter electrodes and the metal lines (Figure 5.1 (c-d)). The SEM images of the TiN layer is depicted in Figure 5.4.

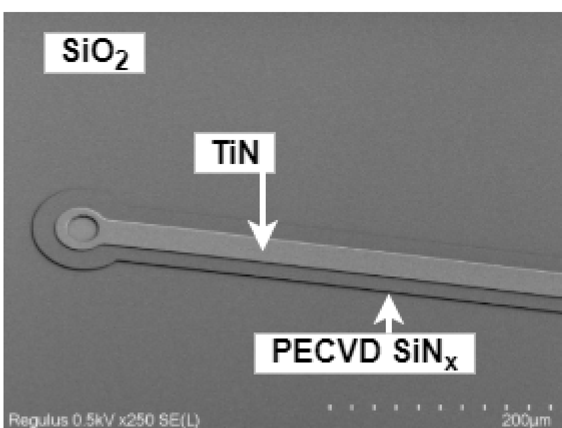

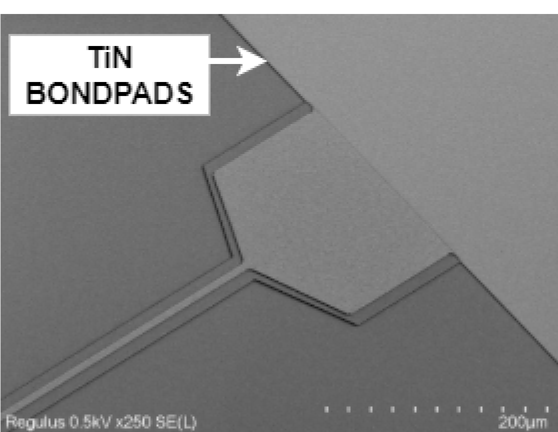

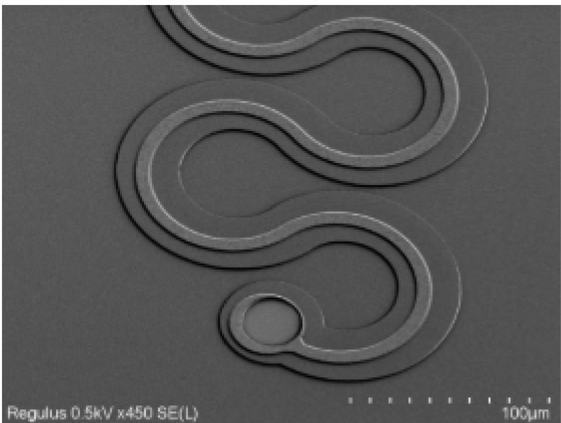

Figure 5.4: SEM images of the TiN metal lines (*straight* lines and *meanders*) on the first SiN_x isolation layer, and the TiN bondpads.

The TiN electrodes and the metal lines are completely insulated by the second layer of PECVD SiN_x.

This second insulating layer was patterned in order to keep the bondpads open, as shown in Figure 5.1 (e). The SEM images showing the insulated TiN metal lines and the exposed bondpads are depicted in Figure 5.5.

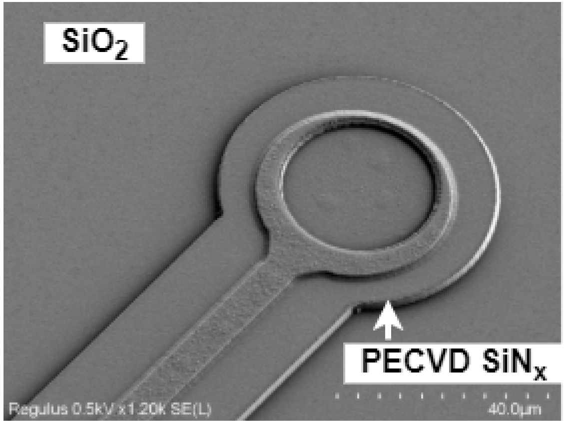

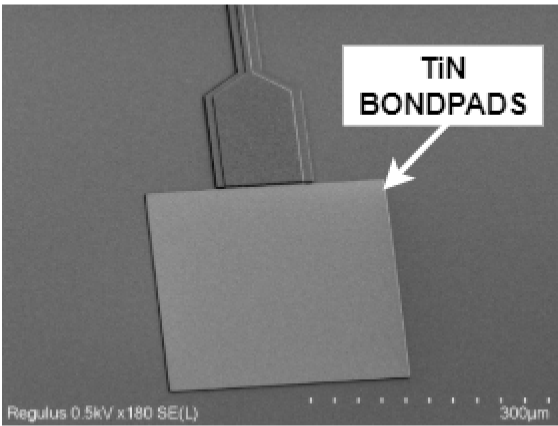

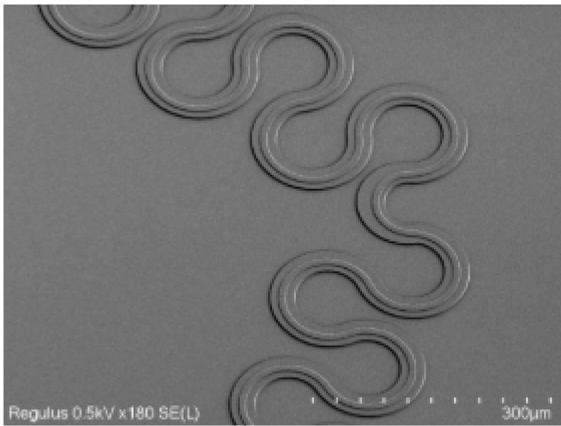

Figure 5.5: SEM images showing the insulated TiN metal lines (*straight* lines and *meanders*) by the second layer of PECVD SiN_x, leaving the TiN bondpads exposed.

The PDMS membrane was released by wet etching the PECVD SiO_2 landing layer, in order to access the TiN electrodes (Figure 5.1 (g)). The final device was imaged from the backside to view the TiN electrodes embedded in a 200 μm thick PDMS membrane, which is supported by a silicon frame. The TiN metal lines are insulated by PECVD SiN_x. The TiN MEA integrated in the *oval* membrane and the novel *turtle* membranes are shown in Figures 5.6, 5.7, and 5.8.

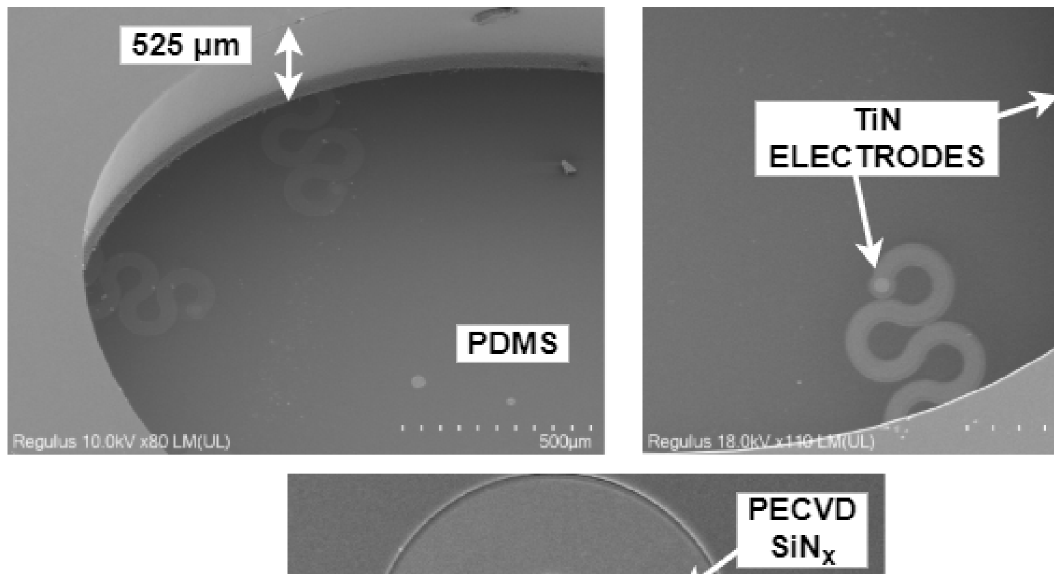

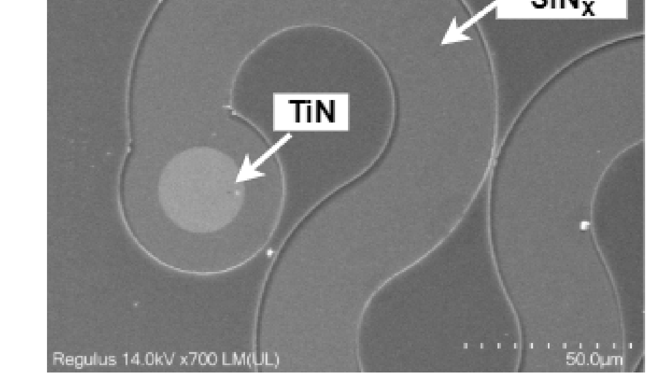

Figure 5.6: SEM images of the 30 μm TiN electrodes embedded in a thick PDMS *oval* membrane. The TiN metal lines are insulated by short *meander* structures of PECVD SiN_x.

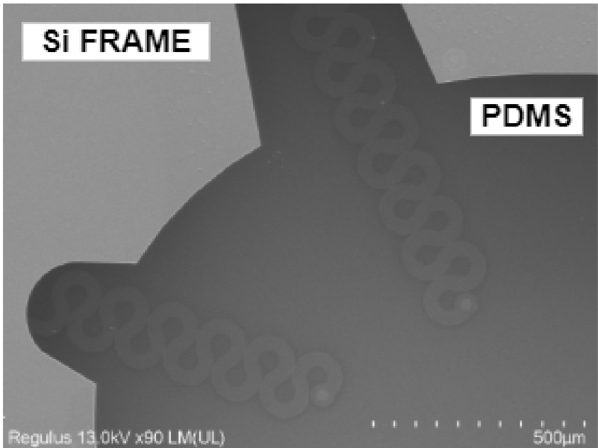

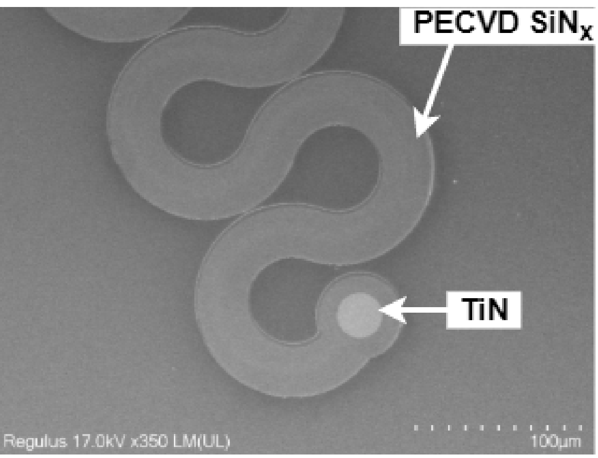

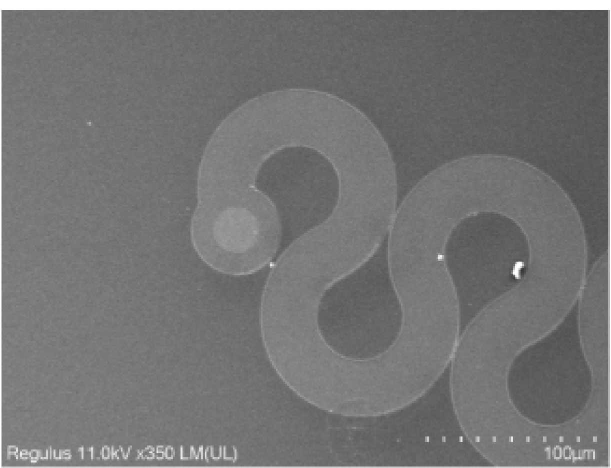

Figure 5.7: SEM images of the 30 μm TiN electrodes integrated in a thick PDMS *turtle* membrane. The TiN metal lines are insulated by long *meander* structures of PECVD SiN_x.

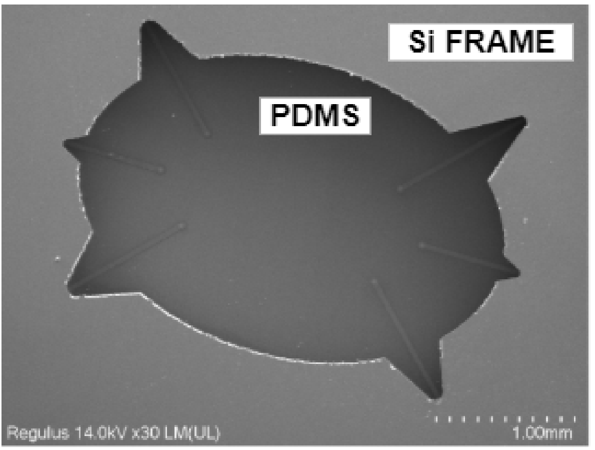

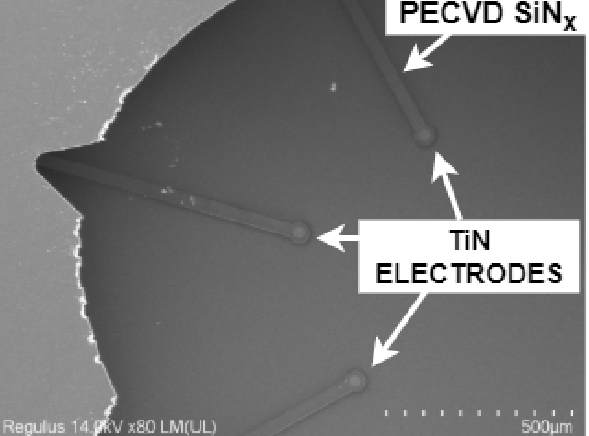

Figure 5.8: SEM images of the 30 μm TiN electrodes embedded in a thick PDMS *oval* membrane. The TiN metal lines are insulated by long *straight* lines of PECVD SiN_x.

Figure 5.9 displays the images of the final device taken under a microscope in which the TiN MEA is embedded in a thick PDMS membrane.

Figure 5.9: Images of the final device taken under an optical microscope, where the TiN electrodes and metal lines are integrated in a thick layer of PDMS, as seen in different designs: (i) EC10 (ii) EC10_Extend (iii) EC30_Extend (iv) EE30_Extend.

As shown in the SEM images, the TiN MEA insulated by PECVD SiN_x, developed in this project, was successfully integrated in a 200 μm thick PDMS membrane with novel designs.

Additionally, Bi/ond achieved the integration of the TiN MEA presented in this thesis in the *inCHIPit*^{TM} device, as shown in Figure 5.10. This was carried out to demonstrate that the TiN MEA developed with the fabrication flow presented in Section 5.1, is compatible for integration in a micro-fluidic device.

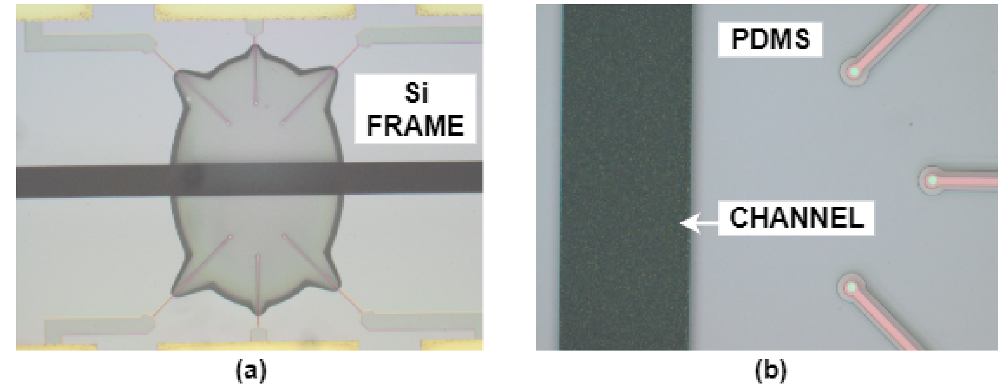

Figure 5.10: Images of the device with the EC10_Extend design, taken under a microscope, which: (a) displays the micro-fluidic channel integrated by Bi/ond, and (b) its magnified image.

5.2 Study of Formation of Cracks

As explained in Section 5.1, we fabricated a Heart-On-Chip device in which a TiN MEA insulated by PECVD SiN_x structures, were successfully embedded in a thick PDMS membrane (Figure 5.6). Previous studies have reported the formation of cracks in the metal lines during the fabrication and post-fabrication process, while using parylene [23], or polyimide [24] isolating structures. Alternatively, we decided to investigate the feasibility of a ceramic material, such as PECVD SiN_x, as the isolation layer for OOC applications.

During the adhesion test presented in Section 4.1, the designs with the *turtle* membrane resulted in fewer cracks, compared to the PECVD SiN_x structures in the *oval* membrane. To reinforce these findings, the final devices fabricated along with the TiN metal lines (Section 5.1) were analyzed under a microscope to study the formation of cracks. The number of cracks formed in the metal lines were calculated for each design, both *before* and *after* the process of dicing. We developed a total of 16 designs for the interconnects in the *oval* and the *turtle* membrane. By determining the number of cracks formed in the TiN metal lines against the total number of metal lines for each design, the yield was calculated.

After the optical inspection of the devices *before* dicing, we could already observe the difference between the *oval* and the *turtle* designs, which indicated that fewer cracks were formed in the lines of the *turtle* designs. Figure 5.11 shows the microscope images of some of the devices *before* dicing. Some of the designs (namely, EE30, EE30_Extend and ME30_Extend) which presented 100% yield *before* dicing are illustrated in Figure 5.11 (a-c). However, there were some designs where the TiN metal lines had broken at the interface of the PDMS membrane and the Si frame, like the ME30 design (Figure 5.11 (d)).

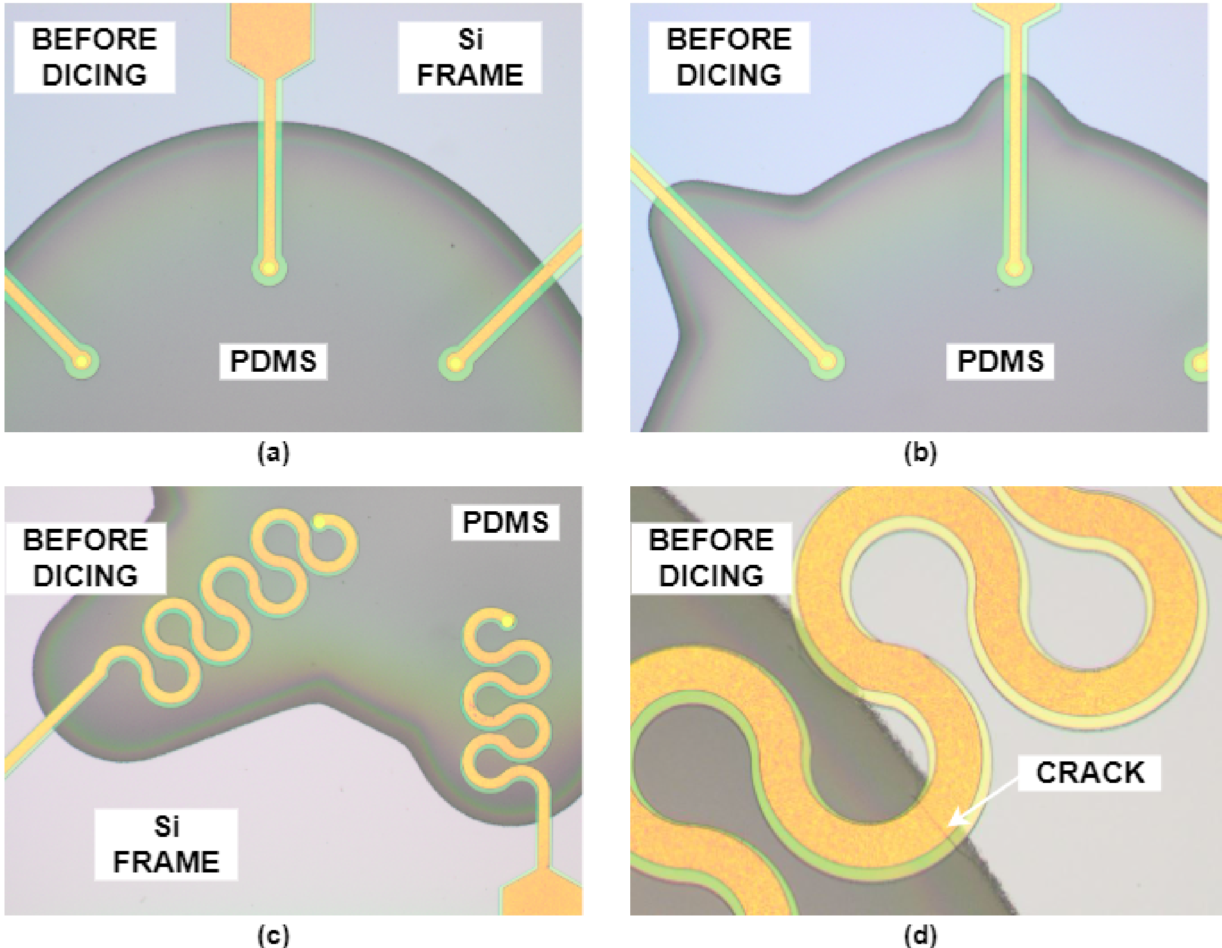

Figure 5.11: Different designs of the device as observed under a microscope *before* the dicing process. No cracks were observed in many of the designs, including: (a) EE30 (b) EE30_Extend, and (c) ME30_Extend designs. However, cracks in the TiN metal lines even *before* dicing were observed in some of the device designs, such as: (d) ME30.

In Figure 5.12 (a-b), the cracks observed in the metal lines *after* the dicing process for the *meanders* in the *oval* design are shown. In contrast, Figure 5.12 (c-d) shows the EC10_Extend device with the *turtle* membrane with *no* cracks in the metal lines.

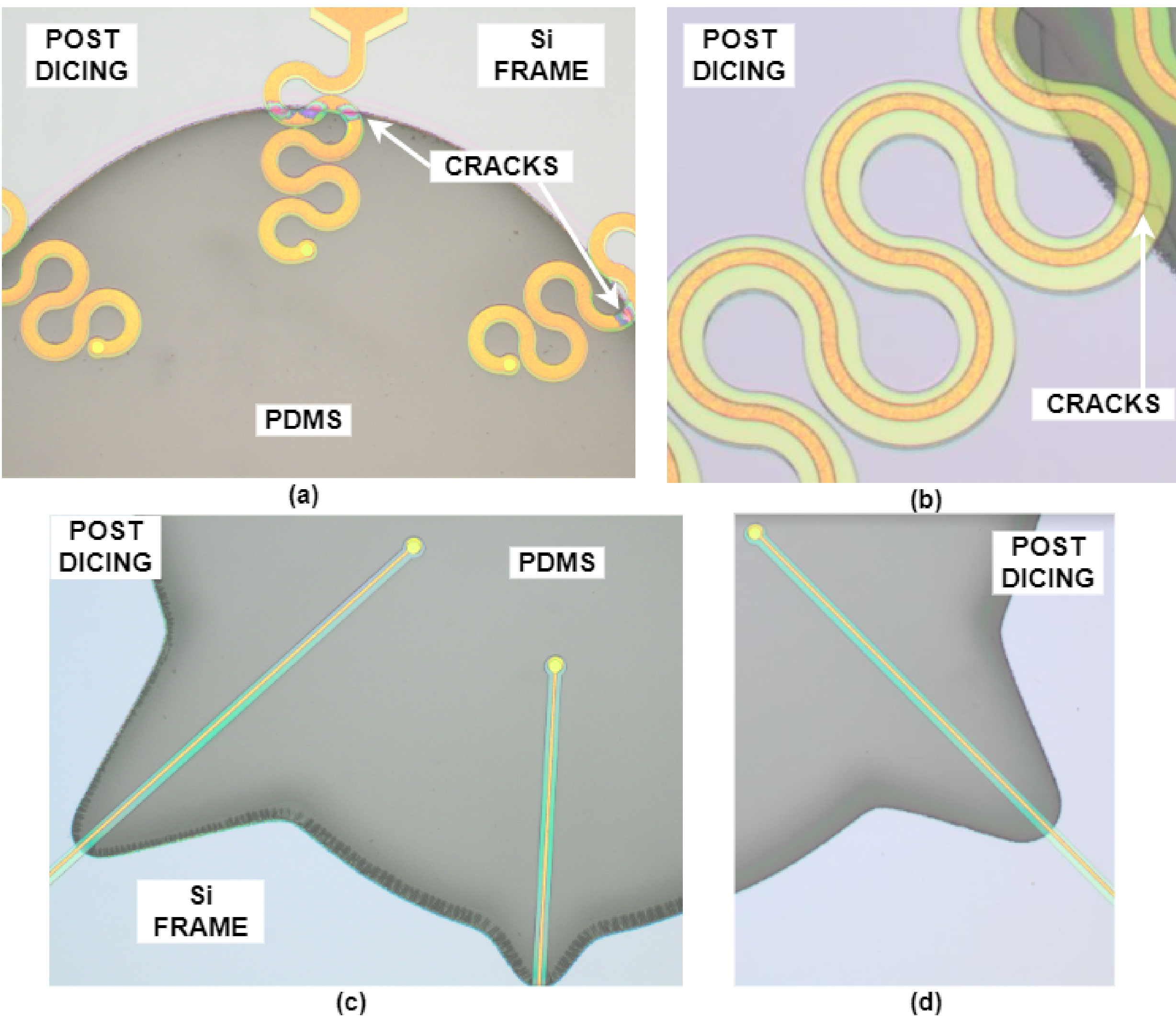

Figure 5.12: Formation of cracks (post dicing) in the horseshoe-shaped TiN *meanders* in the: (a) *oval* membrane, and (b) *turtle* membrane; (c, d) No cracks observed for the *straight* lines in the *turtle* membrane, *after* the dicing process.

An overview of the yield obtained for all the 16 designs are shown in Table 5.1. From the table, it can be seen that *before* dicing, almost all the *turtle* designs displayed a yield of 100% (namely: EE10_Extend, EE30_Extend, EC10_Extend, EC30_Extend, ME10_Extend, ME30_Extend and MC30_Extend). The MC10_Extend design of the *turtle* membrane displayed a high yield of ∼83%. While, only half of the *oval* designs showed 100% yield (namely: EE30, EC10, EC30 and MC30). The remaining *oval* designs showed a comparatively lower yield of ∼50-58%. These results are in line with the simulations performed in Section 3.2, which shows that the extensions in the *turtle* designs, help in improving the yield of the devices *before* the dicing process.

Table 5.1: Percentage yield of metal lines during fabrication and post fabrication process.

OVAL MEMBRANE			***TURTLE MEMBRANE***		
DESIGN NAME	**YIELD %**		**DESIGN NAME**	**YIELD %**	
	BEFORE DICING	**AFTER DICING**		**BEFORE DICING**	**AFTER DICING**
EE10 (300 µm)	**58.3**	**25**	EE10_Extend (300 µm)	**100**	**77.7**
EE30 (300 µm)	**100**	**91.6**	EE30_Extend (300 µm)	**100**	**100**
EC10 (500 µm)	**100**	**50**	EC10_Extend (500 µm)	**100**	**62.5**
EC30 (500 µm)	**100**	**66.6**	EC30_Extend (500 µm)	**100**	**91.6**
ME10 (300 µm)	**50**	**50**	ME10_Extend (300 µm)	**100**	**44.4**
ME30 (300 µm)	**58.3**	**50**	ME30_Extend (300 µm)	**100**	**58.3**
MC10 (500 µm)	**50**	**25**	MC10_Extend (500 µm)	**83.3**	**26.6**

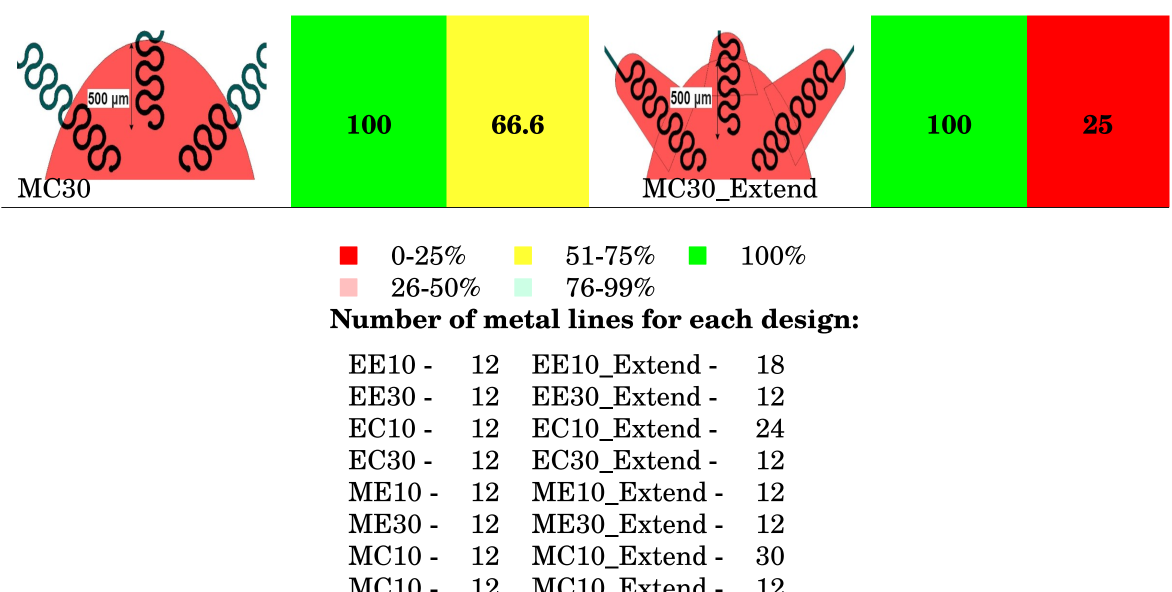

The yield of the devices for the different designs *after* dicing were obtained from optical inspection. As shown in Table 5.1, *straight* metal lines embedded in the *turtle* designs (namely: EE10_Extend, EE30_Extend and EC30_Extend) showed a higher yield (in the range of ∼77-100%). In comparison, the *meanders* in the *turtle* designs exhibited a lower yield (in the range of 25-44%). It should also be noted that only the EE30 design of the *oval* membrane displayed a high yield of 91%, while the other *oval* designs showed a comparatively lower yield (in the range of 25-60%). These results proved that the extensions in the *turtle* membrane reduced the stress developed in the metal lines at the interface, which in turn improved the yield, especially of the *straight* lines.

Based on the results shown in Table 5.1, *before* dicing, 7 of the 8 *turtle* designs displayed 100% yield. The other design of *meanders* in the *turtle* membrane had a yield of 83%. While, only half of the *oval* designs showed a yield of 100% *before* dicing.

After dicing, it was observed that even in the *turtle* designs (except for EE30_Extend), the yield was reduced by at least 9% across all the designs. From Table 5.1, it can be seen that 3 of the 4 *turtle* designs embedded with *straight* lines displayed a yield of 75% and higher. While, only *one* of the *oval* designs with the *straight* lines (namely, EE30) had a yield higher than 75%. All the other *oval* designs showed a comparatively lower yield (in the range of ∼25-65%). It should also be noted that these results may be partially affected by the position of the designs over the 4" wafer. In general, the *meanders* displayed a lower yield in both the *oval* and *turtle* membranes. As stated in Section 2.3.1, *meanders* were expected to survive the dicing process and provide a better yield in comparison to the straight lines. This is contrary to the results obtained in this project. This can be attributed to the limitations encountered during the design of the *meanders*. In order to design a horseshoe-shaped meander of 30 μm width, we were restricted in being able to have a smaller radii for the interconnects, due to which the meanders occupied a large area of the PDMS membrane. According to previous studies, *meanders* with a smaller radii are capable of withstanding larger strains, compared to *meanders* with a larger radii (as is the case in this thesis). Although the dicing process reduces the yield over most of the designs, the *straight* metal lines in the *turtle* designs displayed a higher yield, when compared to the *oval* designs. In conclusion, we could see that Goal 2 of this thesis (Section 1.5) was achieved, since we could identify the designs which reduced the stress in the metal lines at the interface and effectively improved the yield due to the formation of fewer cracks.

5.3 Electrochemical Impedance Spectroscopy (EIS)

Electrochemical Impedance Spectroscopy (EIS) was performed for some of the devices fabricated with the TiN MEA embedded in a 200 μm thick PDMS layer, as shown in Section 5.1. To ensure that the electrodes are functional and to check the electrical connection between the TiN electrodes and the bondpads, EIS

measurements were performed. The impedance measurement set-up is shown in Figure 5.13, which was similar to the three-cell set-up of previous work [99]. In this set-up, the TiN MEA integrated in this device is connected to the TiN bondpads, which served as the working electrode (WE). A platinum (Pt) wire (counter electrode, CE) was wound around an Ag/AgCl reference electrode (RE) and immersed in the blue well (Figure 5.13) containing phosphate buffered saline (PBS). These measurements were carried out over a frequency range of 1 Hz-100 kHz, inside a faraday cage to avoid electromagnetic interference from external sources.

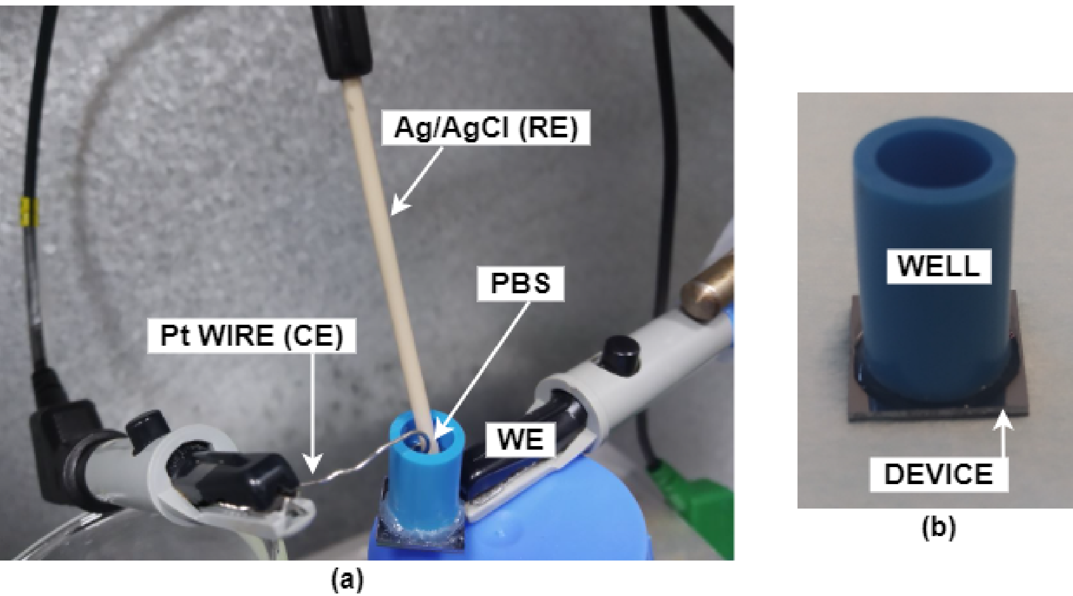

Figure 5.13: Set-up of a three-electrode system for performing EIS measurements for the current device (EC30_Extend).

The bode plots derived from the EIS measurements of the TiN MEA embedded in the thick PDMS membrane are shown in Figure 5.14. From the data obtained, the average impedance value of three working TiN electrodes measured at 1 kHz was found to be 785.9 kΩ. Commercial TiN MEAs report impedance values lower than 100 kΩ [58]. The higher impedance value observed in the TiN MEA embedded in this device can be attributed to its flat surface morphology, as opposed to a fractal morphology [100]. To solve this issue, a layer of PEDOT (Poly (3,4 – Ethylenedioxythiophene)) can be coated on the MEAs. PEDOT is a conductive, porous polymer which can improve the electro-chemical properties [99]. These measurements were carried out to get an impression of the electrical performance of the embedded TiN MEA. Additionally, by demonstrating the electrical connection between the TiN electrodes (in the PBS solution) to the bondpads on the silicon frame, we achieved Goal 3 of the thesis (Section 1.5). We successfully fabricated a Heart-On-Chip device with a working TiN MEA.

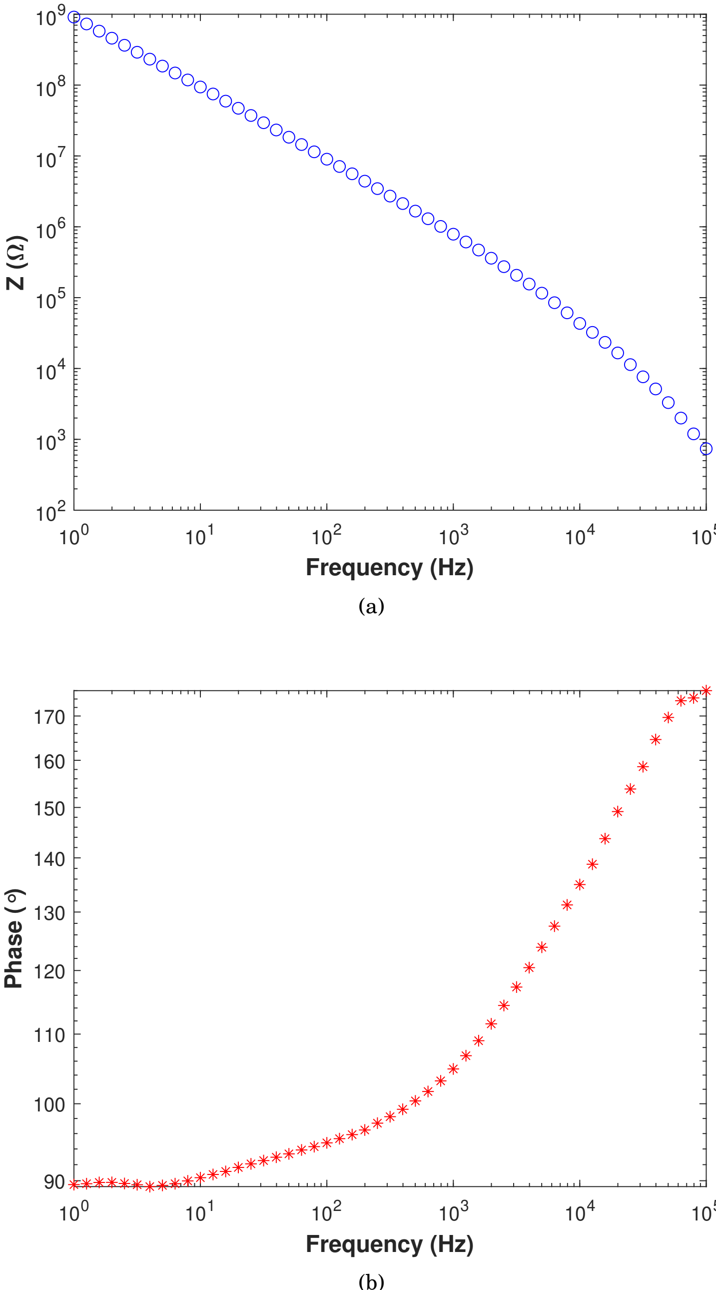

Figure 5.14: The bode plots from the EIS measurements, conduced over a frequency range of 1-100 kHz, of the TiN MEAs.

According to the goals defined in Section 1.5, we successfully integrated a TiN MEA encapsulated by SiN_x isolation structures embedded in a 200 μm thick PDMS membrane for HOC applications. The device was also compatible for the integration of a PDMS micro-fluidic channel (Figure 5.10), based on the techniques developed by Bi/ond. The yield of the TiN metal lines during the fabrication and post-fabrication process was determined for the novel designs developed (Chapter 3) for the *oval* and the *turtle* membranes. It was evident that the extensions introduced to the *oval* geometry of the membrane were instrumental in reducing the stress at the interface, thereby resulting in a higher yield (Table 5.1). The EIS measurements carried out proved that an electrical connection was established between the TiN electrodes in the PBS medium, with the bondpads (Figure 5.14).

6 | Conclusion

Previous OOC platforms have often utilized polymers such as, parylene [23] or polyimide [24], as the insulation layers for the metal interconnects. However, they have reported the formation of cracks in the metal lines during the fabrication and post-fabrication process. Moreover, polymers require dedicated equipment that is specifically reserved for their processing in a silicon-based cleanroom environment. In this thesis, three goals were defined to develop a Heart-On-Chip (HOC) device that addresses these issues. First, a study of the compatibility and characterization of SiN_x insulation layers with the PDMS membranes was performed. Secondly, the yield of the devices was improved by optimizing the mechanical designs of the interconnects and the PDMS membranes. Finally, a microfabrication-compatible protocol to develop a HOC device with a working TiN MEA encapsulated by SiN_x in a 200 μm thick PDMS membrane was optimized.

In this thesis, we investigated the feasibility of ceramic dielectrics, such as silicon nitride, as an alternative for insulating the metal electrodes in OOC devices. Shifting to silicon nitride insulation requires looking into the different depositions techniques to avoid etching away of the material while releasing the membrane. Preliminary studies were conducted to determine the etch rates of LPCVD Si_3N_4 vs PECVD SiN_x in HF and BHF solutions. Moreover, additional testing to determine the effect of the two deposition techniques on the development of stress in the PDMS membrane were performed. Additionally, the adhesion between the nitride structures and the PDMS membrane was addressed, to avoid the delamination of the interconnects. It was found that by integrating a thin SiO_2 layer on top of the nitride structures, an improved adhesion with the PDMS membrane was ensured. It should be noted that thick PECVD SiN_x layers were adopted for the final device to compensate for its higher etching rate in HF and BHF solutions. Moreover, by choosing to utilize a ceramic material for encapsulating the metal lines instead of polymers, TiN could be sputtered at higher temperatures, which resulted in a lower sheet resistance. These findings enabled us to realize Goal 1 (Section 1.5) of the thesis and to develop a process flow for the fabrication of the final device.

In order to obtain a high yield for the devices, the designs of the interconnects as well as the shape of the PDMS membrane were optimized. The trajectories defined for the interconnects were based on the FEM analysis of the magnitude and direction of the principal strains acting on the membrane, when subjected to an external pressure. From these simulations, novel membrane designs were developed, namely the *oval* and the *turtle* designs. The addition of progressively tapering extensions in the *turtle* membrane helped to reduce the stress developed at the interface of the membrane and the silicon frame. Different parameters were explored during the design of the interconnects, namely the shape (*straight* lines and *meanders*), the width (10 μm and 30 μm) and the length (*short* and *long*). In total, 16 novel designs were defined in this project.

The development of cracks in the TiN lines was investigated during the fabrication and post-fabrication process, for the different designs. Accordingly, the yield was calculated for each design. It was observed that the *straight* lines (long and short) in the *turtle* membrane displayed a yield of 75% and higher, even *after* the dicing process. In contrast, the majority of the *oval* designs exhibited a lower yield of $\sim$25-65% *after* dicing. SiN_x insulation in the novel *turtle* designs greatly improved the yield of the TiN metal lines due to the formation of fewer cracks. These results further confirmed the FEM simulation results performed for the different membrane designs. By simulating, testing and analyzing the yield of the different designs, we were able to identify the best designs that effectively improved the yield. In doing so, Goal 2 (Section 1.5) of this project was achieved.

By working on Goals 1 and 2, a silicon-based cleanroom compatible fabrication protocol for the current Heart on Chip device was defined. Additionally, the device was also demonstrated to be compatible with the integration in a micro-fluidic device, by the techniques developed by Bi/ond. Finally, EIS

measurements were carried out to confirm the functionality of the electrodes and to check the electrical connection of the embedded TiN electrodes with the bondpads. The average impedance value at 1 kHz of three working electrodes was measured to be in the order of 800 kΩ, proving that an electrical connection was successfully established in the PBS solution. Commercially available TiN MEAs have reported impedance values in the order of 100 kΩ [58]. he higher impedance value measured in this device can be attributed to its flat surface morphology, as opposed to a fractal morphology [100] of the commercially available MEAs. The electrochemical performance of the TiN MEA embedded in this device should therefore be improved.

6.1 Recommendations and Future Work

In this thesis, various parameters for the design of the interconnects were explored to identify the designs that provide good yield. Although some of the designs with *straight* interconnects in the novel *turtle* membrane exhibited a high yield (∼75-100%), the *meander* interconnects displayed comparatively lower yields (∼25-50%). In order to design horseshoe-shaped *meanders* of 30 μm width, a large radii of 120 μm was defined. Previous studies have demonstrated the improved ability of *meanders* with smaller radii (100 μm) to redistribute stress along their tracks [74]. Therefore, by defining smaller radii (such as, 100 μm) for the *meanders* in combination with narrow metallization strategies, their stress profile at the interface can be potentially improved. This might help to effectively improve the yield of the *meanders* in the novel *turtle* designs during the fabrication and post-fabrication process. With further investigation, the viability of *meanders* with small radii in the *turtle* membrane can be validated.

It has been established that dicing exerts undue pressure on the devices, which ultimately results in the formation of cracks in the metal lines. By defining scribe lines to cut along the crystallographic planes of the silicon wafer, the pressure exerted by the water jet during dicing can be avoided [101]. However, due to the presence of a polymer layer on the wafer, an additional step of cutting through the PDMS layer with a laser is necessary. Investigation of the effect of laser cutting on the biocompatibility of the PDMS membrane is further required.

For this project, the possibility of dry etching the PDMS layer as performed in previous work [102], was not feasible due to the 200 μm thickness of the PDMS membrane. Therefore, the thick PDMS covering the bondpads was removed manually in this thesis. While doing so, there is a high possibility of scratching the material of the bondpads, or breaking the electrical connection between the electrodes and the bondpads. In order to address this problem, we suggest to utilize a mould to pattern the thick 200 μm PDMS layer. This would at the same time solve the issue of the PDMS in the scribe lines mentioned above. However, such automated molding systems are quite expensive platforms and was therefore, beyond the scope of this project.

The impedance value obtained in this project for flat, non-fractal 30 μm diameter TiN electrodes was found to be in the order of 800 kΩ. Commercially available MEAs have reported lower impedance values in the order of 100 kΩ [58]. Therefore, it is necessary to improve the electrochemical properties of the TiN MEA in the current device. One of the ways in which this can be achieved is by increasing the surface roughness of the electrodes. By utilizing the sputtering settings required for a low-stress layer, the TiN layer can be sputtered as a porous layer with a grainy structure thereby increasing its surface roughness [103]. Alternatively, the viability of different electrode materials, such as gold (Au) and platinum (Pt), can be explored. Preliminary tests performed to look into the adhesion of the Au electrodes to the nitride structures showed a poor adhesion. Therefore, by conducting several optimizations for processing Au/Pt electrodes encapsulated by SiN_x, the impedance values can also be drastically improved. The impedance of the MEAs can also be reduced by coating them with a porous, conductive polymer- PEDOT:PSS [99]. But, doing so would require additional equipment to process polymers in a silicon-based cleanroom environment.

In order to develop a fully functional Heart-On-Chip device, a reference electrode and micro-pillars need to be integrated in the device. Finally, long-term biological testing needs to be performed to ensure the feasibility of the SiN_x insulation layers in a cardiac co-culture. Furthermore, the mechanical integrity of the nitride lines during mechanical actuation needs to be tested.

A | Appendices

A.1 Organ-On-Chip (OOC) Models

Some of the well established Organ-On-Chip platforms such as Lungs-On-Chip, Liver-On-Chip, Blood-brain Barrier and Kidney-On-a-Chip are elaborated in more detail below.

A.1.1 Lungs-On-Chip

Lungs are the chief respiratory organs, which receive the air inhaled from the trachea via the smaller bronchi branches. Further branching of the bronchi terminate with the alveoli, which is the primary structure responsible for gas exchange. Carbon dioxide from the body is expelled while oxygen from the inhaled air is absorbed into the bloodstream via capillaries covering the alveoli. This exchange is made possible due to the unique cellular arrangement of the alveoli-capillary interface, wherein the epithelium cells of the alveoli are separated from the endothelium cells of the capillary via a thin, porous membrane [104]. Therefore, it is essential for a Lung-on-Chip device to accommodate the intricate distribution of cells across a membrane that can sustain the periodic stretching which similar to the expansion and contraction of the lungs, as depicted in Figure A.1. These platforms can be applied for screening therapeutic drugs for the treatment of airborne illnesses.

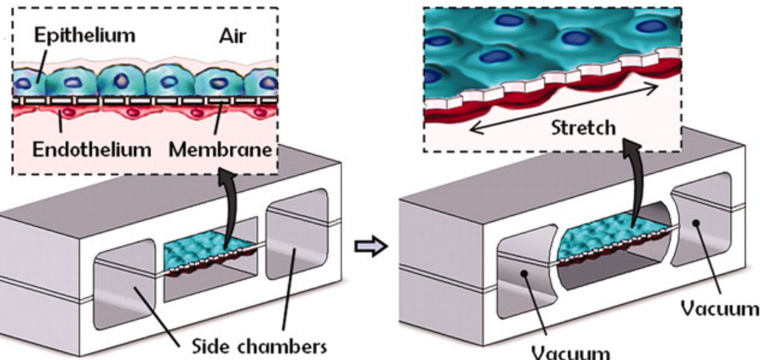

Figure A.1: Illustration of the Lungs-on-Chip platform which comprises of two chambers connected by a porous, thin and flexible polymer membrane; *(right)* Vacuum applied to the two compartments enables the polymer membrane to be stretched which emulates the breathing action in the lungs [105].

The Lung-On-Chip device developed by Huh et al. [105] is s well established platform which consists of two micro-chambers connected by a porous Polydimethylsiloxane (PDMS) membrane. On either side of the membrane coated with extracellular matrix (ECM), human epithelial alveolar cells and human endothelial vascular cells are cultured to replicate the alveoli-capillary interface in an *in-vitro* assay, as illustrated in Figure A.1. The delivery of air to the chamber containing epithelial cells and the introduction of a viscous blood-like fluid to the chamber with endothelial cells mimics the human physiological condition of the lungs with the appropriate flow of fluid and exchange of nutrients and gases. When the two compartments are maintained in vacuum, the connecting PDMS membrane is stretched to emulate the expansion and contraction of the lungs while breathing. In this manner, the immune reaction of the respiratory system can be analyzed.

A.1.2 Liver-On-Chip

The liver functions as an intracorporeal structure mainly involved in the control of ammonia and blood glucose levels, production of multiple hormones and plays a vital role in the metabolism of various compounds [106]. Drug-induced liver injury (DILI) is a common concern which hinders the development of drugs [106, 107]. Modelling the intricate machinery of the liver is a monumental challenge on account of the complex distribution of hepatic cells along the liver lobules. Since the hepatic cells contribute to specialized functions depending on their location in the liver, they develop a radial zone with multifaceted functionalities, which is difficult to recapitulate *in-vitro*. Hence, a physiologically relevant disease model of the liver will aid in accelerating the process of drug evaluation during clinical trials.

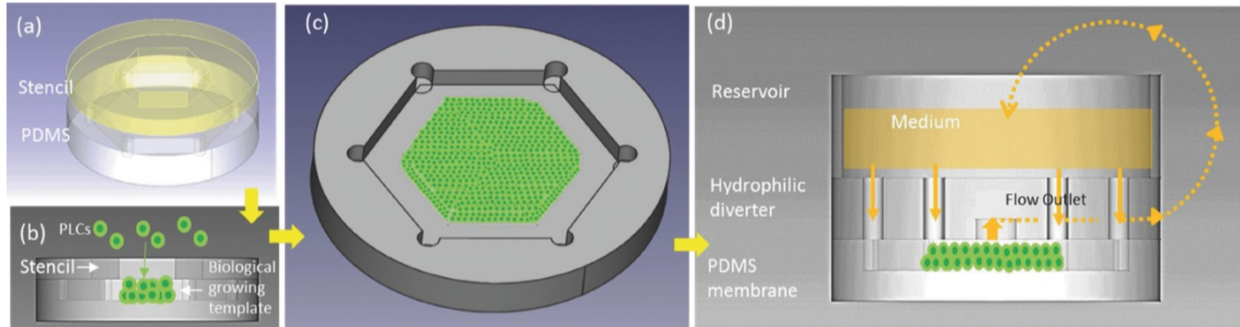

Figure A.2: Multiple layers of primary liver cells (PLCs) cultured on a PDMS substrate to provide (a) a biological guide for the growth of cells; (b) a hexagonal contour; (c) inclusion of a reservoir in the platform to enable circulation; (d) inclusion of a diverter for the purpose of vertical circulation [107]

The Liver-On-Chip platform developed by Weng et al. [107] relied on the utilization of a scaffold for the reconstruction of the 3-Dimensional hierarchy of the hepatic system. The device (as depicted in Figure A.2) is fabricated with a patterned, collagen-coated PDMS membrane on which the liver cells are cultured with the help of a scaffold. The membrane is encompassed within a flow diverter, to provide vertical circulation, which in turn is connected to a reservoir. With the help of a pump, flow is established between the reservoir and the device to recapture the circulation of substances between the liver and the bloodstream in a human body. The hexagonal structure of the membrane can support fluid flow on all six corners, which mimics the functionality of the hepatic portal vein. Additionally, an outlet is provided at the center of the membrane which depicts the flow of fluid from the portal to the central vein. The device demonstrates the viability of a long-term Liver-on-Chip device for evaluation of the pharmaco-kinetics of drugs with the appropriate oragnotypic arrangement of hepatic cells.

A.1.3 Blood-brain Barrier

The blood-brain barrier (BB) is an unique characteristic in the human body and it plays a principal role in the maintenance of homeostasis by offering protection to the brain from harmful substances that circulate in the peripheral blood. Certain neurological diseases adversely affect the barrier [108]. Drugs intended to treat or alleviate these conditions need to surpass the barrier in order to be effective, and is highly dependent on the permeability of the endothelial lining of the blood-brain barrier [108, 109]. The presence of astrocytes augment the tightness of the barrier which in turn affects its permeability to drug molecules. This calls for a pragmatic model of the blood-brain barrier which aid in the study of passage of drug compounds across the barrier and also to discern the underlying mechanisms of neurodegenerative disorders.

The innovative BBB platform developed by Griep et al. [108] comprises of a top and bottom PDMS structures with micro-grooves (for the integration of platinum wires) separated by a porous polycarbonate membrane, as illustrated in Figure A.3. The chip can measure the transendothelial electrical resistance (TEER) of the seeded endothelial cells of the human cerebrum via the platinum wires on the PDMS structures, which was the basis for comprehending the tight juntions of the human BBB. The BBB platform was utilized for studying the shear stress developed in the human blood-brain barrier by introducing fluid flow in the device.

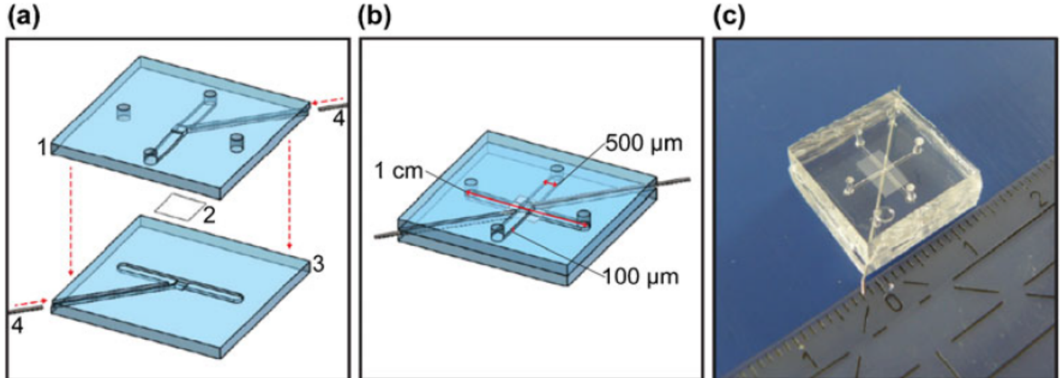

Figure A.3: Schematic illustration of the blood-brain barrier chip: (a) top and bottom faces of the chip; (b) integration of platinum electrodes in the chip; (c) assembled PDMS platform of the chip [108]

A.1.4 Kidney-On-a-Chip

The development of a fully functional kidney-on-a-Chip is an enormous task to achieve, owing to the complexity involved in the arrangement of kidney cells. Nephrons form the functional unit of kidneys, aiding in the formation of urine by regulating the solute and water concentration during the process of filtering blood [104]. Filtration of blood occurs at three regions of the nephrons namely, the glomerulus- where a majority of filtration takes place; the proximal tube- where reabsorption occurs; and the loop of Henle- where the concentration of urea is exponentially increased to form urine. The nephron-on-chip device designed by Weinberg et al. [110] was partially successful in replicating the functionality of nephrons. It consists of two layers that are microfabricated and connected by a membrane, as shown in Figure A.4. This device however, failed to accurately regulate the process of separating waste from the blood sample [104].

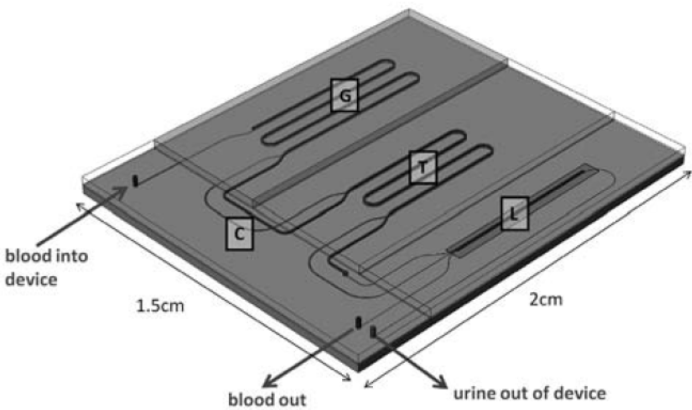

Figure A.4: Illustration of the Nephron-on-Chip device designed by Weinberg et al. [110].

The micro-fluidic platform innovated by Jan et al. [111] comprises of a porous polymeric membrane sandwiched between PDMS compartments for the purpose of investigating the proliferation of renal cells under the influence of shear stress which closely mimics the fluid flow at the interface of the tubule structures in the nephrons [104].

A.2 Wet Etching of Silicon Nitride

The oxide layer deposited on the front side of the wafer during the fabrication of the final device serves as a landing layer during the DRIE process. In order to release the membrane after etching through the silicon substrate (Figure 5.1 (g)), it is necessary to etch the oxide layer on the front side. This can be carried out by wet etching the oxide either in 5% hydrofluoric acid (HF) or in 1:7 buffered hydrofluoric acid (BHF). HF and BHF are known to etch both silicon oxide and silicon nitride at different rates [112, 113]. Therefore, it was crucial to determine the etch rate of LPCVD Si_3N_4 vs PECVD SiN_x in 5% HF and in 1:7 BHF. For this experiment, four test samples were fabricated: (1) LPCVD Si_3N_4 of 600 nm was deposited at 845°C on two samples; (2) PECVD SiN_x of 600nm was deposited at 400°C on the other two samples. Both the samples were patterned lithographically to define the membrane area and the step height between the nitride layer and the silicon substrate was measured on Dektak 8, to obtain the starting point for each sample. To investigate the etch rate in 5% HF, one LPCVD sample and one PECVD sample were immersed in the acid for 5 minutes which was followed by rinsing the samples in DI water. The step profile was again measured at this point to study the etching rate of silicon nitride in 5% HF. This process was repeated for the samples till a step height of approximately 100 nm was obtained between the nitride layer and the silicon substrate. The results of the experiment are depicted in Figure A.5 (a-b). Similarly, the above experiment in 1:7 BHF solution was performed on the remaining LPCVD and PECVD samples. The results of the etching rate of silicon nitride in 1:7 BHF solution are illustrated in Figure A.5 (c-d).

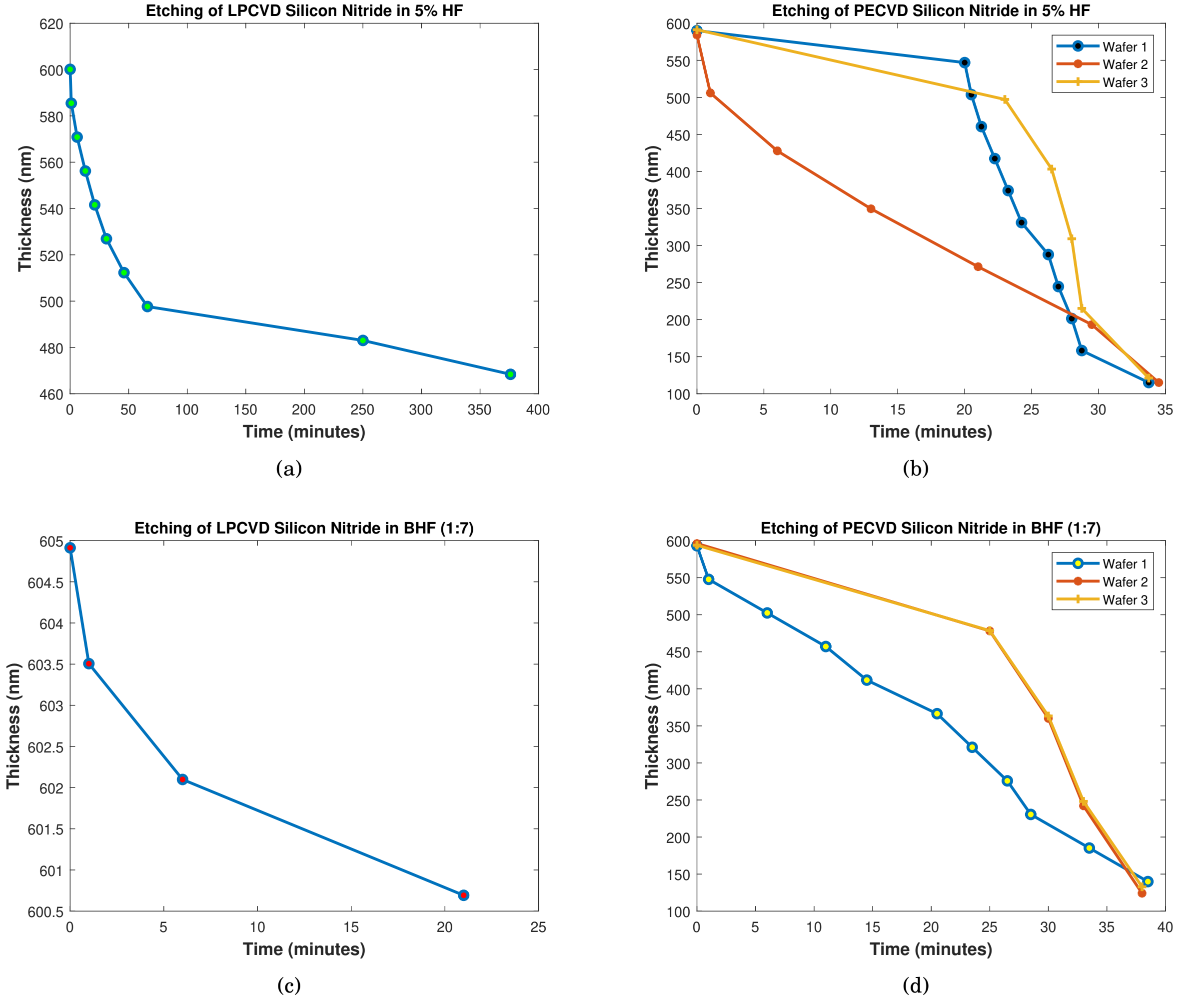

Figure A.5: (a) Etching of LPCVD Si_3N_4 in 5% HF; (b) Etching of PECVD SiN_x in 5% HF; (c) Etching of LPCVD Si_3N_4 in 1:7 BHF; (d) Etching of PECVD SiN_x in 1:7 BHF.

From Figure A.5 (a), it can be clearly observed that LPCVD Si_3N_4 etches at an extremely slow rate in 5% HF at room temperature (RT). To etch ~500 nm of LPCVD Si_3N_4 in 5% HF at RT, about 6 hours was required. After immersion in 5% HF for 5 minutes (which is the time required to etch 2 μm of PECVD SiO_2), only 4 nm of LPCVD Si_3N_4 was etched. In contrast, the PECVD SiN_x displayed a higher etching rate in 5% HF at RT, where ~70 nm was etched after 6 minutes, as shown in Figure A.5 (b). The etching of PECVD SiN_x in 5% HF was reproduced for three different samples. A similar trend was observed for the samples etched in 1:7 BHF. To etch 2 μm of PECVD SiO_2 in 1:7 BHF, ~8 minutes is required. After immersion in 1:7 BHF for 8 minutes, only 6 nm of LPCVD Si_3N_4 was etched, while ~70 nm of PECVD SiN_x was etched in the same period of time. Based on these results, it was concluded that a layer of LPCVD Si_3N_4 survived better when exposed to both 5% HF at RT and 1:7 BHF during the process of releasing the membrane. In this manner, the nitride structures are well protected against the action of HF and BHF, thereby securing the interconnects insulating the metal lines embedded in the PDMS membrane.

A.3 Sheet Resistance of Titanium Nitride

One of the important electrical properties of conductive thin films is its sheet resistance (R_s), which is related to the resistivity (σ) and thickness (t) as follows:

$$R_s = \frac{\rho}{t} \tag{A.1}$$

The measurement of sheet resistance of a material provides insight into the resistivity and conductivity of the material [114]. Due to the inverse relation between resistivity and conductivity, materials with a lower resistivity exhibit better conductive properties. It should also be noted that the temperature plays a significant role in the magnitude of the resistivity of the material [115]. With increasing growth temperatures of the material, the value of its resistivity decreases, resulting in increased conductivity [90]. Titanium nitride (TiN) can be sputtered on a silicon wafer at either lower or higher temperatures. Since TiN is commonly employed as the material for micro-electrodes, it is favourable to sputter TiN at higher temperatures, such as 350°C, to obtain a lower value of resistivity. On account of the fact that the interconnects for the current Heart-On-Chip platform are formed by silicon nitride, as opposed to PI, sputtering of the metal electrodes at higher temperatures was feasible. To experimentally verify the resistivity values of TiN, test samples were processed at different temperatures. 300 nm of TiN was sputtered on 4" DSP wafer of 525 μm thickness. On one sample, sputtering was carried out at 350°C, while for another sample. TiN was sputtered at 25°C (which is the temperature at which metals are commonly sputtered on PI structures). The sheet resistance of these samples was measured via the four-probe technique and the corresponding resistivity values were calculated. The results are depicted in Table A.1.

Table A.1: Resistivity values of TiN sputtered at different temperatures.

Sputtering of TiN	**Resistivity (Ω.cm)**
at 25°C	2.32×10^{-3}
at 350°C	2.69×10^{-4}

The resistivity value obtained for the sample with TiN sputtered at 25°C was higher by one order of magnitude, when compared to the sample with TiN sputtered at 350°C. This trend has been previously observed for platinum (Pt) films at different growth temperatures, as illustrated in Figure 2.12 [90]. These values were instrumental in reinforcing the choice of silicon nitride as a material for the interconnects, as opposed to PI.

Bibliography

[1] Holly Matthews, James Hanison, and Niroshini Nirmalan. "“Omics”-informed drug and biomarker discovery: opportunities, challenges and future perspectives". In: *Proteomes* 4.3 (2016), p. 28.

[2] *"Drug Discovery and Development: Understanding the R&D Process"*. Pharmaceutical Research and Manufacturers of America, Feb-2007.

[3] *“Pharmaceutical Research and Manufacturers of America, 2013 Biopharmaceutical Research Industry Profile.”*. Pharmaceutical Research and Manufacturers of America, Washington DC: PhPMA, Jul-2013.

[4] Oliver Gassmann et al. *Leading Pharmaceutical Innovation: How to Win the Life Science Race*. Springer, 2018.

[5] Aleksander Skardal, Thomas Shupe, and Anthony Atala. “Organoid-on-a-chip and body-on-a-chip systems for drug screening and disease modeling”. In: *Drug discovery today* 21.9 (2016), pp. 1399–1411.

[6] Anja van de Stolpe and Jaap den Toonder. “Workshop meeting report Organs-on-Chips: human disease models”. In: *Lab on a chip* 13.18 (2013), pp. 3449–3470.

[7] Lorna Ewart et al. “Application of microphysiological systems to enhance safety assessment in drug discovery”. In: *Annual review of pharmacology and toxicology* 58 (2018), pp. 65–82.

[8] Massimo Mastrangeli, Sylvie Millet, Janny van den Eijnden-van Raaij, et al. “Organ-on-chip in development: towards a roadmap for organs-on-chip”. In: (2019).

[9] Amalia M Issa et al. “Drug withdrawals in the United States: a systematic review of the evidence and analysis of trends”. In: *Current drug safety* 2.3 (2007), pp. 177–185.

[10] Mosha Abulaiti et al. “Establishment of a heart-on-a-chip microdevice based on human iPS cells for the evaluation of human heart tissue function”. In: *Scientific reports* 10.1 (2020), pp. 1–12.

[11] Joel Lexchin. “Drug withdrawals from the Canadian market for safety reasons, 1963–2004”. In: *Cmaj* 172.6 (2005), pp. 765–767.

[12] Yu Shrike Zhang et al. “From cardiac tissue engineering to heart-on-a-chip: beating challenges”. In: *Biomedical Materials* 10.3 (2015), p. 034006.

[13] Chung Yu Chan et al. “Accelerating drug discovery via organs-on-chips”. In: *Lab on a Chip* 13.24 (2013), pp. 4697–4710.

[14] Dongeun Huh et al. “Microengineered physiological biomimicry: organs-on-chips”. In: *Lab on a Chip* 12.12 (2012), pp. 2156–2164.

[15] Andries D van der Meer and Albert van den Berg. “Organs-on-chips: breaking the in vitro impasse”. In: *Integrative Biology* 4.5 (2012), pp. 461–470.

[16] Ashutosh Agarwal et al. “Microfluidic heart on a chip for higher throughput pharmacological studies”. In: *Lab on a Chip* 13.18 (2013), pp. 3599–3608.

[17] Dongeun Huh et al. “Microfabrication of human organs-on-chips”. In: *Nature protocols* 8.11 (2013), pp. 2135–2157.

[18] João Ribas et al. “Cardiovascular organ-on-a-chip platforms for drug discovery and development”. In: *Applied In Vitro Toxicology* 2.2 (2016), pp. 82–96.

[19] E Holt et al. “Electrical stimulation of adult rat cardiomyocytes in culture improves contractile properties and is associated with altered calcium handling”. In: *Basic research in cardiology* 92.5 (1997), pp. 289–298.

[20] Adam W Feinberg et al. “Muscular thin films for building actuators and powering devices”. In: *Science* 317.5843 (2007), pp. 1366–1370.

[21] Nikolas Gaio et al. “Cytostretch, an organ-on-chip platform”. In: *Micromachines* 7.7 (2016), p. 120.

[22] S Khoshfetrat Pakazad et al. “A novel stretchable micro-electrode array (SMEA) design for directional stretching of cells”. In: *Journal of Micromechanics and Microengineering* 24.3 (2014), p. 034003.

[23] S Khoshfetrat Pakazad. “Stretchable Micro-Electrode Arrays for Electrophysiology”. In: (2015).

[24] N Gaio. “Organ-on-Silicon”. In: (2019).

[25] Adam Timmis et al. “European Society of Cardiology: cardiovascular disease statistics 2019”. In: *European heart journal* 41.1 (2020), pp. 12–85.

[26] Michael B Bracken. “Why animal studies are often poor predictors of human reactions to exposure”. In: *Journal of the Royal Society of Medicine* 102.3 (2009), pp. 120–122.

[27] Neal D Barnard and Stephen R Kaufman. “Animal research is wasteful and misleading”. In: *Scientific American* 276.2 (1997), pp. 80–82.

[28] Allen Cato, Lynda Sutton, and Allen Cato III. *Clinical Drug Trials and Tribulations, Revised and Expanded*. Vol. 120. CRC Press, 2002.

[29] Nicole T Feric and Milica Radisic. “Maturing human pluripotent stem cell-derived cardiomyocytes in human engineered cardiac tissues”. In: *Advanced drug delivery reviews* 96 (2016), pp. 110–134.

[30] Mina T Kelleni and Mahrous Abdelbasset. *Drug induced cardiotoxicity: mechanism, prevention and management*. IntechOpen, London, UK, 2018.

[31] Keith Finlayson et al. “Acquired QT interval prolongation and HERG: implications for drug discovery and development”. In: *European journal of pharmacology* 500.1-3 (2004), pp. 129–142.

[32] Bernard Fermini and Anthony A Fossa. “The impact of drug-induced QT interval prolongation on drug discovery and development”. In: *Nature reviews Drug discovery* 2.6 (2003), pp. 439–447.

[33] Stefan Robbert Braam. “Human embryonic stem cells: advancing biology and cardiogenesis towards functional applications l”. In: (2010).

[34] Jeanne M Nerbonne and Robert S Kass. “Molecular physiology of cardiac repolarization”. In: *Physiological reviews* 85.4 (2005), pp. 1205–1253.

[35] Liliana Sintra Grilo, Pierre-Alain Carrupt, and Hugues Abriel. “Stereoselective inhibition of the hERG1 potassium channel”. In: *Frontiers in Pharmacology* 1 (2010), p. 137.

[36] CL Lawrence et al. “In vitro models of proarrhythmia”. In: *British journal of pharmacology* 154.7 (2008), pp. 1516–1522.

[37] Ahmed E Enayetallah et al. “Assessing the translatability of in vivo cardiotoxicity mechanisms to in vitro models using causal reasoning”. In: *BMC Pharmacology and Toxicology* 14.1 (2013), p. 46.

[38] Oren Caspi et al. “In vitro electrophysiological drug testing using human embryonic stem cell derived cardiomyocytes”. In: *Stem cells and development* 18.1 (2009), pp. 161–172.

[39] Ahmed E Enayetallah et al. “Assessing the translatability of in vivo cardiotoxicity mechanisms to in vitro models using causal reasoning”. In: *BMC Pharmacology and Toxicology* 14.1 (2013), p. 46.

[40] Alan Lloyd Hodgkin. “The ionic basis of electrical activity in nerve and muscle”. In: *Biological Reviews* 26.4 (1951), pp. 339–409.

[41] Alan L Hodgkin and Bernard Katz. “The effect of sodium ions on the electrical activity of the giant axon of the squid”. In: *The Journal of physiology* 108.1 (1949), p. 37.

[42] DR Curtis, JW Phillis, and JC Watkins. “Chemical excitation of spinal neurones”. In: *Nature* 183.4661 (1959), pp. 611–612.

[43] Ulrich Egert and Thomas Meyer. “Heart on a chip—extracellular multielectrode recordings from cardiac myocytes in vitro”. In: *Practical methods in cardiovascular research*. Springer, 2005, pp. 432–453.

[44] Thomas Meyer et al. “Micro-electrode arrays in cardiac safety pharmacology”. In: *Drug Safety* 27.11 (2004), pp. 763–772.

[45] Tamir Gabay et al. "Electro-chemical and biological properties of carbon nanotube based multi-electrode arrays". In: *Nanotechnology* 18.3 (2007), p. 035201.

[46] Alexandra Gramowski et al. "Substance identification by quantitative characterization of oscillatory activity in murine spinal cord networks on microelectrode arrays". In: *European Journal of Neuroscience* 19.10 (2004), pp. 2815–2825.

[47] Joseph J Pancrazio et al. "Portable cell-based biosensor system for toxin detection". In: *Sensors and Actuators B: Chemical* 53.3 (1998), pp. 179–185.

[48] Guenter W Gross et al. "Odor, drug and toxin analysis with neuronal networks in vitro: extracellular array recording of network responses". In: *Biosensors and Bioelectronics* 12.5 (1997), pp. 373–393.

[49] Ronen Segev et al. "Observations and modeling of synchronized bursting in two-dimensional neural networks". In: *Physical Review E* 64.1 (2001), p. 011920.

[50] Conrad D James et al. "Extracellular recordings from patterned neuronal networks using planar microelectrode arrays". In: *IEEE Transactions on biomedical engineering* 51.9 (2004), pp. 1640–1648.

[51] Mandy B Esch et al. "How multi-organ microdevices can help foster drug development". In: *Advanced drug delivery reviews* 69 (2014), pp. 158–169.

[52] Supramaniam Srinivasan. "Electrode/electrolyte interfaces: Structure and kinetics of charge transfer". In: *Fuel Cells*. Springer, 2006, pp. 27–92.

[53] Stuart F Cogan. "Neural stimulation and recording electrodes". In: *Annu. Rev. Biomed. Eng.* 10 (2008), pp. 275–309.

[54] Thomas Stieglitz. "Electrode materials for recording and stimulation". In: *Neuroprosthetics: theory and practice*. World Scientific, 2004, pp. 475–516.

[55] Zbigniew Stojek. "The electrical double layer and its structure". In: *Electroanalytical methods*. Springer, 2010, pp. 3–9.

[56] *Electrical Double-Layer Formation Part 1 (Nanotechnology)*. URL: http://what-when-how.com/nanoscience-and-nanotechnology/electrical-double-layer-formation-part-1-nanotechnology/ (visited on 02/20/2021).

[57] Tomi Ryynänen et al. "All titanium microelectrode array for field potential measurements from neurons and cardiomyocytes—a feasibility study". In: *Micromachines* 2.4 (2011), pp. 394–409.

[58] *Microelectrode Array (MEA) Manual*. URL: https://www.multichannelsystems.com/sites/multichannelsystems.com/files/documents/manuals/MCS_MEA_Manual.pdf (visited on 01/04/2021).

[59] *Ayanda™ MEA Biochips- Product Catalog*. URL: https://alascience.com/products/pdf/MEA_Product_Catalog.pdf (visited on 01/04/2021).

[60] James D Weiland, David J Anderson, and Mark S Humayun. "In vitro electrical properties for iridium oxide versus titanium nitride stimulating electrodes". In: *IEEE transactions on biomedical engineering* 49.12 (2002), pp. 1574–1579.

[61] Evelina Slavcheva et al. "Sputtered iridium oxide films as charge injection material for functional electrostimulation". In: *Journal of the Electrochemical Society* 151.7 (2004), E226.

[62] Hamid Charkhkar et al. "Chronic intracortical neural recordings using microelectrode arrays coated with PEDOT–TFB". In: *Acta Biomaterialia* 32 (2016), pp. 57–67.

[63] Elena Valderrama et al. "Microfabrication and characterisation of microelectrode arrays for in vivo nerve signal recording". In: *Proceedings of the International Solid-State Sensors and Actuators Conference-TRANSDUCERS'95*. Vol. 1. IEEE. 1995, pp. 63–66.

[64] H Cesiulis et al. "The study of thin films by electrochemical impedance spectroscopy". In: *Nanostructures and thin films for multifunctional applications*. Springer, 2016, pp. 3–42.

[65] J Bard Allen and R Faulkner Larry. *Electrochemical methods fundamentals and applications*. John Wiley & Sons, 2001.

[66] David C Duffy et al. "Rapid prototyping of microfluidic systems in poly (dimethylsiloxane)". In: *Analytical chemistry* 70.23 (1998), pp. 4974–4984.

[67] Skarphedinn Halldorsson et al. "Advantages and challenges of microfluidic cell culture in polydimethylsiloxane devices". In: *Biosensors and Bioelectronics* 63 (2015), pp. 218–231.

[68] Michael W Toepke and David J Beebe. “PDMS absorption of small molecules and consequences in microfluidic applications”. In: *Lab on a Chip* 6.12 (2006), pp. 1484–1486.

[69] BJ Van Meer et al. “Small molecule absorption by PDMS in the context of drug response bioassays”. In: *Biochemical and biophysical research communications* 482.2 (2017), pp. 323–328.

[70] Dennis E Discher, David J Mooney, and Peter W Zandstra. “Growth factors, matrices, and forces combine and control stem cells”. In: *Science* 324.5935 (2009), pp. 1673–1677.

[71] Anna Grosberg et al. “Ensembles of engineered cardiac tissues for physiological and pharmacological study: heart on a chip”. In: *Lab on a chip* 11.24 (2011), pp. 4165–4173.

[72] Sebastian Sosin. “Interconnect schemes for stretchable array-type microsystems”. In: (2011).

[73] Shivani Joshi et al. “Investigation of “fur-like” residues post dry etching of polyimide using aluminum hard etch mask”. In: *Materials Science in Semiconductor Processing* 75 (2018), pp. 130–135.

[74] Fabrice Axisa et al. “Stretchable engineering technologies for the development of advanced stretchable polymeric systems”. In: *PORTABLE-POLYTRONIC 2008-2nd IEEE International Interdisciplinary Conference on Portable Information Devices and the 2008 7th IEEE Conference on Polymers and Adhesives in Microelectronics and Photonics*. IEEE. 2008, pp. 1–8.

[75] Dae-Hyeong Kim et al. “Flexible and stretchable electronics for biointegrated devices”. In: *Annual review of biomedical engineering* 14 (2012), pp. 113–128.

[76] Jong-Hyun Ahn and Jung Ho Je. “Stretchable electronics: materials, architectures and integrations”. In: *Journal of Physics D: Applied Physics* 45.10 (2012), p. 103001.

[77] T Adrega and SP Lacour. “Stretchable gold conductors embedded in PDMS and patterned by photolithography: fabrication and electromechanical characterization”. In: *Journal of Micromechanics and Microengineering* 20.5 (2010), p. 055025.

[78] Samuel Rosset et al. “Metal ion implantation for the fabrication of stretchable electrodes on elastomers”. In: *Advanced Functional Materials* 19.3 (2009), pp. 470–478.

[79] P Wei et al. “Stretchable microelectrode array using room-temperature liquid alloy interconnects”. In: *Journal of Micromechanics and Microengineering* 21.5 (2011), p. 054015.

[80] Richard Gordon Budynas, J Keith Nisbett, et al. *Shigley’s mechanical engineering design*. Vol. 8. McGraw-Hill New York, 2008.

[81] Joseph E Shigley, Charles R Mischke, and Thomas Hunter Brown Jr. *Standard handbook of machine design*. McGraw-Hill Education, 2004.

[82] William C Wilson and Gary M Atkinson. “Review of polyimides used in the manufacturing of micro systems”. In: (2007).

[83] Filipa Verdasca. “Microfabrication Technologies for Neural Drug Delivery”. In: ().

[84] *Essentials For Curing Polyimide Films*. URL: http://archive.constantcontact.com/fs077/1101427030702/archive/1109948285639.html (visited on 01/04/2021).

[85] WJ Wu et al. “Polyimide-damage-free, CMOS-compatible removal of polymer residues from deep reactive ion etching passivation”. In: *Journal of Electronic Materials* 44.3 (2015), pp. 991–998.

[86] JAG Baggerman, RJ Visser, and EJH Collart. “Ion-induced etching of organic polymers in argon and oxygen radio-frequency plasmas”. In: *Journal of applied physics* 75.2 (1994), pp. 758–769.

[87] David L Pappas, Jerome J Cuomo, and Krishna G Sachdev. “Studies of adhesion of metal films to polyimide”. In: *Journal of Vacuum Science & Technology A: Vacuum, Surfaces, and Films* 9.5 (1991), pp. 2704–2708.

[88] Shuai Shi et al. “Fabricating processes of free-standing silicon nitride thin film for MEMS devices”. In: *2013 14th International Conference on Electronic Packaging Technology*. IEEE. 2013, pp. 23–26.

[89] Kunigunde Cherenack et al. “SiNx barrier layers deposited at 250°C on a clear polymer substrate”. In: *2006 MRS Spring Meeting*. 2006, pp. 7–12.

[90] Jon S Agustsson et al. “Growth, coalescence, and electrical resistivity of thin Pt films grown by dc magnetron sputtering on SiO2”. In: *Applied Surface Science* 254.22 (2008), pp. 7356–7360.

[91] Richard J Mills et al. "Functional screening in human cardiac organoids reveals a metabolic mechanism for cardiomyocyte cell cycle arrest". In: *Proceedings of the National Academy of Sciences* 114.40 (2017), E8372–E8381.

[92] *Force Sensing With Elastic Micropillars*. URL: http://biomechanicalregulation-lab.org/elastic-pillars (visited on 02/20/2021).

[93] Mario Gonzalez et al. "Design of metal interconnects for stretchable electronic circuits". In: *Microelectronics Reliability* 48.6 (2008), pp. 825–832.

[94] Emily N Sevcik et al. "Patterning on topography for generation of cell culture substrates with independent nanoscale control of chemical and topographical extracellular matrix cues". In: *Current protocols in cell biology* 75.1 (2017), pp. 10–23.

[95] Chris Yang and John Pham. "Characteristic study of silicon nitride films deposited by LPCVD and PECVD". In: *Silicon* 10.6 (2018), pp. 2561–2567.

[96] Yu-Cheng Chen et al. "Achieving high aspect ratio wrinkles by modifying material network stress". In: *Soft Matter* 13.22 (2017), pp. 4142–4147.

[97] Xi Chen and John W Hutchinson. "Herringbone buckling patterns of compressed thin films on compliant substrates". In: *J. Appl. Mech.* 71.5 (2004), pp. 597–603.

[98] Jan Genzer and Jan Groenewold. "Soft matter with hard skin: From skin wrinkles to templating and material characterization". In: *Soft Matter* 2.4 (2006), pp. 310–323.

[99] Affan Affan Kaysa Waafi. "Fabrication and Characterization of PEDOT coated Microelectrodes Array for Organ-on-Chip Application". In: (2018).

[100] Hyunsu Park, Pavel Takmakov, and Hyowon Lee. "Electrochemical evaluations of fractal microelectrodes for energy efficient neurostimulation". In: *Scientific reports* 8.1 (2018), pp. 1–11.

[101] Mike Cooke. "Scribe and dice". In: *III-Vs Review* 19.4 (2006), pp. 20–24.

[102] Nikolas Gaio et al. "Versatile and Automated 3D Polydimethylsiloxane (PDMS) Patterning for Large-Scale Fabrication of Organ-on-Chip (OOC) Components". In: *Multidisciplinary Digital Publishing Institute Proceedings*. Vol. 2. 13. 2018, p. 873.

[103] JF Creemer et al. "Microhotplates with TiN heaters". In: *Sensors and Actuators A: Physical* 148.2 (2008), pp. 416–421.

[104] Hüseyin AVCI et al. "Recent advances in organ-on-a-chip technologies and future challenges: a review." In: *Turkish Journal of Chemistry* 42.3 (2018).

[105] Dongeun Huh et al. "Reconstituting organ-level lung functions on a chip". In: *Science* 328.5986 (2010), pp. 1662–1668.

[106] Jiu Deng et al. "Engineered liver-on-a-chip platform to mimic liver functions and its biomedical applications: A review". In: *Micromachines* 10.10 (2019), p. 676.

[107] Yu-Shih Weng et al. "Scaffold-free liver-on-a-chip with multiscale organotypic cultures". In: *Advanced materials* 29.36 (2017), p. 1701545.

[108] Lonneke M Griep et al. "BBB on chip: microfluidic platform to mechanically and biochemically modulate blood-brain barrier function". In: *Biomedical microdevices* 15.1 (2013), pp. 145–150.

[109] Balabhaskar Prabhakarpandian et al. "SyM-BBB: a microfluidic blood brain barrier model". In: *Lab on a Chip* 13.6 (2013), pp. 1093–1101.

[110] E Weinberg, M Kaazempur-Mofrad, and J Borenstein. "Concept and computational design for a bioartificial nephron-on-a-chip". In: *The International journal of artificial organs* 31.6 (2008), pp. 508–514.

[111] Kyung-Jin Jang and Kahp-Yang Suh. "A multi-layer microfluidic device for efficient culture and analysis of renal tubular cells". In: *Lab on a Chip* 10.1 (2010), pp. 36–42.

[112] D Martin Knotter and TJJ Dee Denteneer. "Etching mechanism of silicon nitride in HF-based solutions". In: *Journal of The Electrochemical Society* 148.3 (2001), F43.

[113] Sami Franssila. *Introduction to microfabrication*. John Wiley & Sons, 2010.

[114] *Sheet Resistance: A Guide to Theory*. URL: https://www.ossila.com/pages/sheet-resistance-theory#sheet-resistance-derivation (visited on 02/20/2021).

[115] *Resistivity*. URL: https://www.britannica.com/science/resistivity (visited on 02/20/2021).